Understanding the progenitor formation galaxies of merging binary black holes

Rahul Srinivasan

UNIVERSITÉ CÔTE D'AZUR

ÉCOLE DOCTORALE
SCIENCES FONDAMENTALES ET APPLIQUÉES

THÈSE DE DOCTORAT

Comprendre les galaxies à l'origine de la fusion des trous noirs binaires

Rahul SRINIVASAN

Laboratoire J.-L. Lagrange - Observatoire de la Côte d'Azur
Laboratoire Artemis - Observatoire de la Côte d'Azur

Présentée en vue de l'obtention du grade de docteur en Sciences de la Planète et de l'Univers
de l'Université Côte d'Azur

Dirigée par : Astrid LAMBERTS, Chargée de recherche CNRS, Observatoire de la Côte d'Azur, Nice
Co-dirigée par : Marie-Anne BIZOUARD, Directrice de recherche CNRS, Observatoire de la Côte d'Azur, Nice
Soutenue le : 12-October-2023

Devant le jury, composé de :
Mathias SCHULTHEIS, Astronome, Observatoire de la Côte d'Azur, Nice
Tomasz BULIK, Professeur, University of Warsaw, Warsaw, Poland
Sylvain CHATY, Professeur, Université Paris Cité, Paris
Frédérique MARION, Directrice de recherche CNRS, Laboratoire d'Annecy-le-Vieux de Physique des Particules, Annecy
Irina DVORKIN, Maître de conférence, Sorbonne Université, Paris

COMPRENDRE LES GALAXIES À L'ORIGINE DE LA FUSION DES TROUS NOIRS BINAIRES

Understanding the progenitor formation galaxies of merging binary black holes

Rahul SRINIVASAN

Jury :

Président du jury

Mathias SCHULTHEIS, Astronome, Observatoire de la Côte d'Azur, Nice

Rapporteurs

Tomasz BULIK, Professeur, University of Warsaw, Warsaw, Poland
Sylvain CHATY, Professeur, Université Paris Cité, Paris

Examinatrices

Frédérique MARION, Directrice de recherche CNRS, Laboratoire d'Annecy-le-Vieux de Physique des Particules, Annecy
Irina DVORKIN, Maître de conférence, Sorbonne Université, Paris

Directrice de thèse

Astrid LAMBERTS, Chargée de recherche CNRS, Observatoire de la Côte d'Azur, Nice

Co-directrice de thèse

Marie-Anne BIZOUARD, Directrice de recherche CNRS, Observatoire de la Côte d'Azur, Nice

---

Université Côte d'Azur

Comprendre les galaxies à l'origine de la fusion des trous noirs binaires

Résumé La détection d'ondes gravitationnelles (OG) provenant de la fusion de deux trous noirs de 30 masses solaires en 2015 a surpris les astrophysiciens, car tous les trous noirs connus de la Voie Lactée ont des masses de l'ordre de 10-15 masses solaires, et le consensus général de la communauté était que la formation de trous noirs au delà de 20 masses solaires par l'effondrement d'une étoile massive était improbable. Cette découverte a immédiatement soulevé la question de l'origine des trous noirs de masse stellaire. Si la plupart des fusions de trous noirs proviennent d'étoiles massives évoluant dans des systèmes binaires, de grandes incertitudes subsistent sur leur évolution. Mon objectif est de comprendre l'environnement galactique typique dans lequel se produisent les fusions de trous noirs.

À cette fin, j'adopte une approche systématique avec plusieurs modèles de formation d'étoiles et d'évolution binaire. Je modélise les progéniteurs des fusions de trous noirs en fonction de leur époque de formation, de la masse actuelle de la galaxie hôte et de la métallicité stellaire pour 240 modèles. J'utilise des modèles semi-analytiques du taux de formation d'étoiles et des codes de synthèse de population binaire. Je fournis des lignes directrices pour déduire les propriétés des galaxies et de l'époque de formation, en soulignant l'interaction entre le taux de formation stellaire et l'efficacité de la formation de trous noirs binaires, qui dépendent tous deux fortement de la métallicité. Je trouve que si pour plus de 50% des fusions de trous noirs la métallicité du progéniteur est de quelques dixièmes de la métallicité solaire, il existe cependant de fortes disparités selon les modèles. Les trous noirs de faible masse (< 15 masses solaires) sont plutôt situés dans les galaxies plus lourdes que la Voie Lactée. En revanche, les fusions de trous noirs plus massifs proviennent surtout de galaxies naines de plus faible métallicité. Je trouve que les progéniteurs des trous noirs binaires détectables proviennent de galaxies naines à un redshift de formation plus faible (z < 1). Enfin, je construis la distribution de probabilité des propriétés de l'environnement du progéniteur pour tout signal d'OG détecté. Pour la fusion massive GW150914, je montre qu'elle provient probablement d'un environnement de très faible métallicité. Les résultats sont publiés dans la revue MNRAS [Srinivasan et al., 2023].

J'ai aussi conçu une validation de principe d'un nouvel algorithme de détection d'OG, avec un autre doctorant. Nous utilisons une méthode d'estimation parcimonieuse et apprentissage de dictionnaire pour reconstruire les signaux d'OG enfouis dans le bruit du détecteur. Se distinguant des méthodes traditionnelles basées sur le filtrage adapté, cette technique d'apprentissage automatique permet d'identifier rapidement la présence d'OG dans les données. J'ai testé les performances de l'agorithme avec des injections d'OG provenant de la population astrophysique de trous noirs générée par mes simulations.

Mots-clés – ondes gravitationnelles, galaxies, étoiles, astrophysique, modélisation, apprentissage automatique

Understanding the progenitor formation galaxies of merging binary black holes

Abstract The first gravitational wave (GW) detection, the merger of two 30 $M_\odot$ black holes, came as a surprise to the astrophysicists as all black holes we know of in the Milky Way have masses around 10-15 $M_\odot$ and the general consensus of the stellar physics community was that forming black holes with mass $\gtrsim$ 20 $M_\odot$ from the collapse of a massive star was unlikely. This discovery immediately raised the question regarding the origins of massive stellar-mass black holes. Most black hole mergers are thought to come from massive stars evolving in binary systems, but major uncertainties remain both on the formation and the evolution of massive binary stars. I focus on understanding the typical galactic environment in which binary black hole mergers arise.

To this end, I take a systematic approach in simulating multiple models of the star formation and binary evolution in the Universe. I synthesize progenitors of binary black hole mergers as a function of the redshift of progenitor formation, present-day formation galaxy mass, and progenitor stellar metallicity for 240 star formation and binary evolution models. I use semi-analytic models of the star formation rate and binary population synthesis codes to simulate probable binary evolution models. I provide guidelines to infer the formation galaxy properties and time of formation, highlighting the interplay between the star formation rate and the efficiency of forming merging binary black holes from binary stars, both of which strongly depend on metallicity. I find that across models, over 50% of BBH mergers have a progenitor metallicity of a few tenths of solar metallicity, however, inferring formation galaxy properties strongly depends on both the binary evolution model and global metallicity evolution. The numerous, low-mass black holes ($<$ 15 $M_\odot$) trace the bulk of the star formation in galaxies heavier than the Milky Way. In contrast, heavier BBH mergers typically stem from larger black holes forming in lower metallicity dwarf galaxies. I find that the progenitors of detectable binary black holes tend to arise from dwarf galaxies at a lower formation redshift ($z < 1$). I finally produce a posterior probability of the progenitor environment for any detected gravitational wave signal. For the massive GW150914 merger, I show that it likely comes from a very low-metallicity environment. The results are published in the MNRAS journal [Srinivasan et al., 2023].

In addition to the astrophysical analysis of binary black holes, in collaboration with another PhD student, I am designing a proof-of-concept of a novel GW detection pipeline. We use sparse dictionary coding to reconstruct GW signals buried in detector noise. Distinguishing itself from traditional, match filtering-based pipelines, our machine learning-based technique can rapidly identify the presence of GWs within the detector data. I test the performance of the pipeline with injections of GWs from the astrophysical population of merging black holes generated by my simulations.

Keywords: gravitational waves, galaxies, stars, astrophysics, modeling, machine learning

Acknowledgement

I was quite fortunate to have supervisors who are empathetic and understanding of the different stages in the life of a Ph.D. student while they progress through their research. Astrid and Marie-Anne, your guidance over these formative years of my career has instilled principles that allow me to function as an independent, *capable* researcher. I express my sincere gratitude to you for all the discussions, advice, and pleasant memories we shared.

I am forever indebted to my teachers through school, undergraduate, and research assistantships. I thank my first inspiration in physics during school: teachers Gyaaneshwaran and Madhusudan. You've left an everlasting impression on so many students like myself. Thank you Prof Ramakrishnan for providing the opportunity for my first internship in research. Of course, Prof Sashideep: you provided the single best course in Relativity that I shaped my career based on the inspiration. I hope we may collaborate soon, perhaps as colleagues this time. Professors Archana and Varun, thank you for the opportunity and guidance that prepared me for the Ph.D.

Over the past three years, I have been surrounded by people who inspire me, both through their capacity as a fellow researcher and as a source of fortitude. I have been pleasantly surprised by the number of people who have entered my life as indispensable friends. To you, my dearest friends, colleagues, and confidants, I am forever grateful for your love, support, and company. Thank you, MJ, Faly, Yacine for being my family away from home. Words cannot express how much your presence means to me, so you will have to excuse me if I do not attempt a description. Thank you, Hugo, for our invigorating gym sessions that pushed me to the very limits. If only you joined OCA a couple of years ago, imagine the gains. Dinil, thank you for my first, among many, tennis sessions and for showing me that a coder can flourish in physics. Tristan, for sharing my distaste towards the uncertainties in the CE, teaching me to ski and surf, and making conferences less boring. Yara, so glad you moved to Nice. Another big reason for me to come visit often. Please take care of the people of Monteb' when I'm not there. Nayeem, I'm glad you're keeping up with our liberation routine. Keep at it. And to the many many people who make me miss life in Nice so much: thank you Fabi, Amel, Kasia, Xiuheng, Meng Fei, Xuandi, Jo, Leo, Luc, Joachim, Mel, Mircea, Sab, Mohammed (Mahmoud), Priyam. Sunrise and Mathieu, I sure wish you guys joined sooner. I shall come to visit for the many memories we are yet to make.

My wonderful parents: your ***constant*** encouragement has brought me further in life than should be possible. Your unwavering support makes me approach unfamiliarity with confidence. And Raghav, it's such a pleasure to see you grow up as a smart and infinitely more handsome adult. Although I always regret missing portions of your life when I was away studying, I thoroughly enjoyed visiting and annoying you with my "veri". My grandparents: your belief in my abilities (oftentimes undeserved, but always appreciated) inspires me to eventually be worthy of it. Finally, Ridam. It's only apt that I mention you in this paragraph. You've been witness to it all. You inspire me to pursue research. It is always interesting to see how our lives progress.

Contents

Chapter 1

Introduction

Gravitational wave (GW) astronomy has become a staple topic of discussion in the context of understanding the astrophysics and origins of compact objects like back holes (BHs) and neutron stars. The number of detections of binary black holes (BBHs) has exponentially risen from successive observing runs. In addition to the existing 90 [Abbott et al., 2023] compact binary coalescence (CBC) detections declared by the LIGO-Virgo-KAGRA (LVK) collaboration, the advent of the fourth observing run (O4) is expected to bring the number of detections well into the hundreds [Abbott et al., 2018]. With this wealth of GW data, we can statistically probe the origins of black holes by combining information from the detected GW parameters with its progenitor, ie. parent, star formation and evolution models [Lamberts et al., 2016, O'Shaughnessy et al., 2017, Mapelli et al., 2017, Schneider et al., 2017, Boco et al., 2019, Neijssel et al., 2019, Artale et al., 2020, Broekgaarden et al., 2022, Santoliquido et al., 2022]. The aim of my thesis is to understand the properties of the progenitor galaxies of BBH mergers that form via the isolated binary evolution of massive stars.

The poor sky localization capabilities of GW detectors do no permit them to identify the host galaxies of CBCs [Abbott et al., 2018]. The host galaxy of the first detected binary neutron star merger, GW170817 [Abbott et al., 2017] was identified by observing its electromagnetic (EM) counterparts with telescopes with far greater angular resolution than GW detectors. Unfortunately, most BBH mergers are unlikely to have a detectable EM counterpart [Veres et al., 2019]. Therefore, to understand their progenitor environment, we cannot rely on GW or EM observations alone and must include simulations to infer the formation galaxy parameters. Current literature has highlighted the challenge in predicting the progenitors of BBH mergers primarily due to uncertainties in modeling their formation mechanisms [see Mapelli, 2021a, Mandel and Broekgaarden, 2022, for recent reviews]. Two widely accepted formation channels of merging BBHs are isolated binary evolution of stars [e.g. Bethe and Brown, 1998, Belczynski et al., 2002, Kalogera et al., 2007, Dominik et al., 2012, Belczynski et al., 2016, Eldridge and Stanway, 2016, Stevenson et al., 2017,

Kruckow et al., 2018, Giacobbo and Mapelli, 2018, Kruckow et al., 2018] and dynamical interactions of black holes in dense environments such as young star clusters, globular clusters or nuclear star clusters [e.g. Sigurdsson and Hernquist, 1993, Portegies Zwart and McMillan, 2000, Rodriguez et al., 2015, Mapelli, 2016, Rodriguez et al., 2016, Askar et al., 2017, Samsing, 2018, McKernan et al., 2018, Di Carlo et al., 2019, Zevin et al., 2019].

The astrophysical interpretation of GW events comes in different flavors. Some studies build detailed models for stellar and binary evolution which produce BBH mergers with global properties, such as masses and spins, that can be compared with observations [Spera et al., 2019, Marchant et al., 2021, Bavera et al., 2021, Zevin and Bavera, 2022, Bavera et al., 2023, Dorozsmai and Toonen, 2022]. Other models rely on sets of simplified models that can be easily used to build entire populations of compact objects, which can be directly compared with observations [Mapelli et al., 2017, Giacobbo et al., 2018, Mapelli and Giacobbo, 2018, Mapelli et al., 2019, Baibhav et al., 2019, Broekgaarden et al., 2022, van Son et al., 2022]. These populations are based on a combination of models of binary evolution and metallicity-dependent global star formation in the Universe, which can be built using cosmological simulations, semi-analytic models and/or observations.

Recent studies have highlighted the importance of the star formation model when it comes to population inference of merging black holes, as these often stem from low-metallicity progenitor stars. Modeling the whole range of progenitor metallicity across cosmic history is a key aspect towards understanding compact object mergers but it is far from being straightforward [Chruslinska and Nelemans, 2019]. One can assume a simple evolution with redshift [Giacobbo et al., 2018], including a scatter in the metallicity distribution at all redshifts [Santoliquido et al., 2021]. Models based on cosmological simulations directly provide redshift-dependent distributions of the metallicity, across different types of galaxies [Mapelli et al., 2017, Schneider et al., 2017, Artale et al., 2020]. Otherwise, one can use the combination of the mass-metallicity relation (or the fundamental metallicity relation Santoliquido et al., 2022) across different galaxy masses with a galaxy stellar mass function to build a star formation model [Boco et al., 2019, Neijssel et al., 2019, Broekgaarden et al., 2022]. These studies find that the choice of star formation model, through the distribution of metallicity, is equally important as the choice of binary evolution model, when it comes to determining BBH merger rates. I focus on studying how the uncertainties of the metallicity distribution throughout cosmic history impact our inference of the progenitor environment of BBH mergers.

Such an analysis requires both observations of BBHs, and simulations of the formation and evolution of stars that form the BBHs of the Universe. The former can be found in the wealth of GW data regarding BBH population properties [Abbott et al., 2023], whereas the latter requires an understanding of the star formation in the Universe and its binary evolution mechanisms. To this end, this chapter has been organized into sections that examine and explain the evolution of the Universe at different scales. In § 1.1, I describe the formation of the large-scale structure in the Universe, specifically, dark-matter halos and galaxies. Within

galaxies, in § 1.2 I discuss the star formation rate, its parameterization, and the associated model uncertainties. Then, looking at a given binary star system, in § 1.3 I discuss various binary evolution prescriptions used to model the evolution of binaries. Finally, in § 1.4, I discuss the formation, simulation, and simulated detection of GWs from BBH mergers by ground-based detectors.

1.1 Formation of large scale structure

In this section, I provide an overview of the formation of large-scale structure, their properties, and their rate of occurrence based on Mo et al. [2010], Planelles et al. [2015] and Cimatti et al. [2019]. The underlying framework of any model describing the large-scale structure of the Universe is the assumed cosmology. One such cosmological framework is the ΛCDM model which is used to describe the accelerated expansion of the Universe from the Big Bang, to the emergence of the cosmic microwave background radiation, and up to the present-day rate of expansion. In this manuscript, I assume a flat ΛCDM cosmology model with cosmological parameters $\Omega_{\rm M} = 0.3089$, $\Omega_\Lambda = 0.6911$, and Hubble constant $H_0 = 67.74$ km/s/Mpc [Planck Collaboration et al., 2016]. Within the ΛCDM cosmology, large-scale structure arises from quantum fluctuations in the matter density of the pre-inflationary Universe. Eventually, regions of over-density underwent gravitational collapse resulting in the formation of large-scale structure primarily comprised of dark matter in the shape of halos. In the early Universe, the process of baryogenesis [Sakharov, 1967] is hypothesized to have brought about a baryonic asymmetry, ie., matter dominated over anti-matter. Early dark-matter halos were host to this baryonic matter in the form of hot hydrogen gas. As the hot gas eventually cooled, they collapsed to form galaxies. Observation-based analytical models [Tegmark et al., 1997, Barkana and Loeb, 2001] and 3-dimensional N-body numerical simulations [Klypin and Shandarin, 1983] have shown that the earliest dark-matter halos and the galaxies within emerged at a redshift of 10 to 30, with a typical halo mass of $10^5 - 10^8$ $M_\odot$. Over cosmic time, the halos gravitationally interact with each other, sometimes merging to form larger halos. These halo mergers also led to the merger of their galaxies, facilitating the growth of galaxies.

A halo merger history describes the redshift evolution of the masses and the number of previously-formed smaller halos that merged to ultimately form a present-day halo. The former, earlier halos are known as the progenitors of the latter, present-day halos. The halo merger history has been theoretically modeled and verified by observations. The Press-Schechter formalism [Press and Schechter, 1974] is one such mathematical model that predicts the number of objects (like halos and galaxies) that are formed of a certain mass at a given time and within a given volume. It is derived by evolving smooth density perturbations of matter under the influence of gravity and constrained by observations that indicate a power law for the mass distribution of halos with an exponential cutoff above a

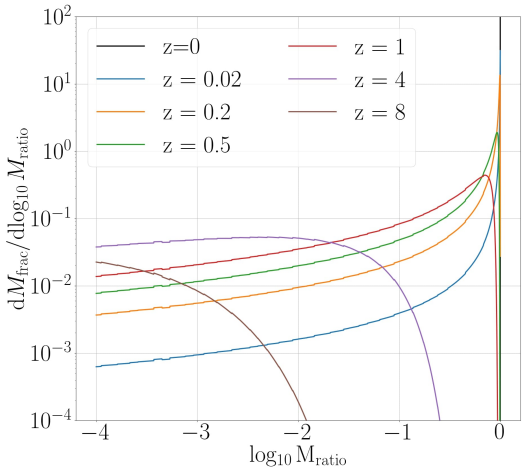

Figure 1.1: Halo merger history: redshift evolution of a present-day halo of mass 10^{13} $\mathrm{M}_\odot$ as a function of the progenitor halo's mass ratio M_{ratio}, defined as the ratio of the masses of the progenitor and the present-day halo, and the fraction of mass M_{frac} from the present-day halo that comes from the progenitor halos with the given mass ratio. The figure was made using the fit from Cole et al. [2007], based on the extended Press-Schechter formalism [Lacey and Cole, 1993]. Shown in color is the progenitor halo distribution at different redshifts.

characteristic mass that increases with time. Better adapted towards mapping present-day halos with their progenitors, the extended Press-Schechter formalism [Lacey and Cole, 1993] includes a conditional mass function to keep track of the halo merger history. In order to monitor the history of a halo, the extension accounts for the probability that a halo of a given mass $M_{1\,\mathrm{Halo}}$ at redshift z_1 will have a mass $M_{2\,\mathrm{Halo}}$ at a redshift z_2.

To elaborate on a typical merger evolution of a halo in the Universe, I show the halo merger history of a present-day halo with mass 10^{13} $\mathrm{M}_\odot$ in Figure 1.1. I depict the merger history of a present-day halo by showing the redshift evolution of the mass ratio of its progenitor halos. The figure shows that at high redshifts, the progenitor halos are numerous and have low mass. For example, for redshift 4 and above, all progenitor halos have a mass that is well below 50% of the present-day halo mass (mass ratio < 0.5). As redshift decreases, the progenitors get larger through mergers as can be seen in the shift of the halo mass ratio to higher values. Eventually, the mass fraction of progenitor halos approaches a delta function and the mass ratio approaches 1, indicating the formation of the massive present-day halo.

One can model the relation between the mass of galaxies and their corresponding host halos from cosmological simulations of galaxy formation (such as the FIRE suite Hopkins

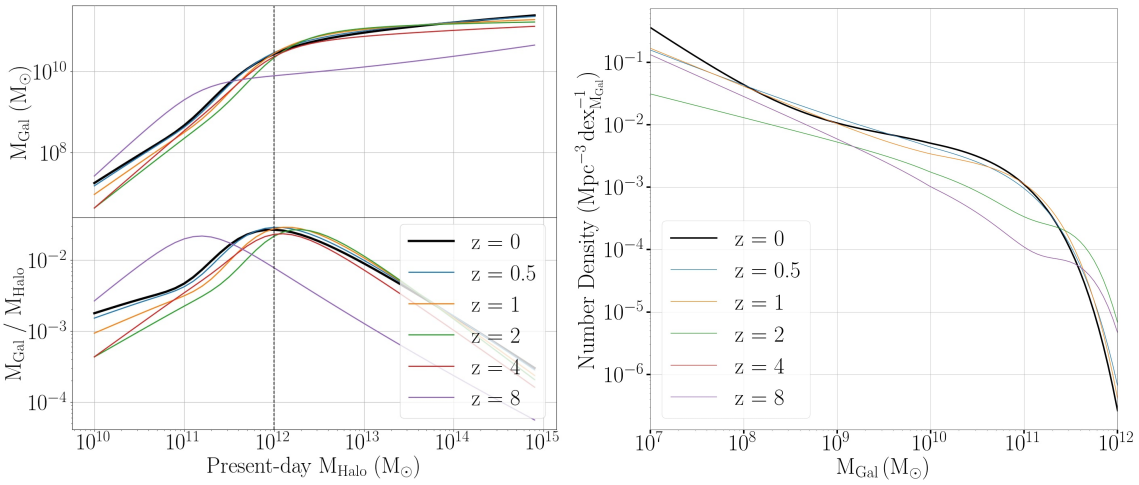

Figure 1.2: **Top left** Galaxy mass $M_{\rm Gal}$ as a function of the present-day mass of the corresponding host halo $M_{\rm Halo}$ at different redshifts z, shown in color. This figure was produced by following the abundance matching technique using the prescription from Behroozi et al. [2010]. **Bottom left** Galaxy formation efficiency, defined as the mass of galaxy formed per unit halo mass, as a function of present-day halo mass. Here, the efficiency of galaxy formation is quantified by the ratio of the galaxy mass to halo mass. The dotted black line at present-day $\rm M_{Halo} = 10^{12}\ M_\odot$ indicates the typical halo mass with maximum efficiency of forming galaxies for redshift < 8. **Right** galaxy stellar mass function: the number density ($\rm Mpc^{-3}\ dex^{-1}_{M_{Gal}}$) of galaxies as a function of galaxy mass $M_{\rm Gal}$ and z using the fit from Tomczak et al. [2014].

et al., 2014) or using fitting functions that are based on observations of galaxies and their host-halos (such as the abundance matching technique Behroozi et al., 2010), or a combination of the two. In this manuscript, I use abundance matching, a method that maps the rank-order galaxy mass with the rank-order halo mass from observations such that the heaviest halos contain the heaviest galaxies (due to their large gravitational potential well), and vice-versa. Figure 1.2, top left, illustrates this relationship. Moreover, it shows that as we go back in time (increasing redshift), a given present-day halo had progressively smaller progenitors that hosted progressively smaller galaxies, consistent with halo merger history (Figure 1.1).

The efficiency of forming galaxies within halos has been observed to depend on the mass of the halo, and on feedback processes from stellar evolution and the supermassive black hole at the center of the galaxy. To understand the galaxy formation efficiency for a given halo mass, I show the galaxy mass formed per unit halo mass in Figure 1.2, bottom left. The dotted black line at present-day $M_{Halo} = 10^{12}$ $M_\odot$ indicates the typical halo mass with maximum efficiency of forming galaxies for redshift < 8. Across redshifts, small halos ($M_{Halo} \lesssim 10^{11}$ $M_\odot$) fail to form large galaxies due to the halo's weak gravitational potential well. Due to their low escape velocity, dwarf galaxies lose the majority of star-forming gas by stellar feedback processes like winds, radiation of energetic ultraviolet photons capable of ionizing cold gas, and supernovae explosions from the first generation of stars. On the other hand, large halos ($M_{Halo} \gtrsim 10^{13}$ $M_\odot$) lose efficiency at forming proportionally large galaxies due to a feedback effect of active galactic nuclei (AGN) at the center of massive galaxies [Garrison-Kimmel et al., 2013] which heats and disturbs the gas, hampering star formation.

Ultimately, the relative abundance of galaxies in the Universe is determined by the merger history of halos and their efficiency of forming galaxies. This can be modeled by a number density of galaxies as a function of their mass and redshift, known as the galaxy stellar mass function. In Figure 1.2, right, I show an observation-based fit of the galaxy stellar mass function from Tomczak et al. [2014]. Generally, across redshift, smaller galaxies are more numerous. Moreover, with time, the number density of galaxies generally tends to increase as can be inferred from the increasing area under the galaxy stellar mass function with decreasing redshift.

1.2 Star formation rate

The star formation rate (SFR) within a galaxy directly depends on the amount of star-forming gas available within it which can be modeled by the host galaxy's mass and redshift (or equivalently, time) of formation. Figure 1.3 shows the observed redshift evolution of the SFR density (SFRD), commonly referred to as the "cosmic star formation history". The star formation in the early Universe rose, peaking between redshift 1.5 and 2, and subsequently

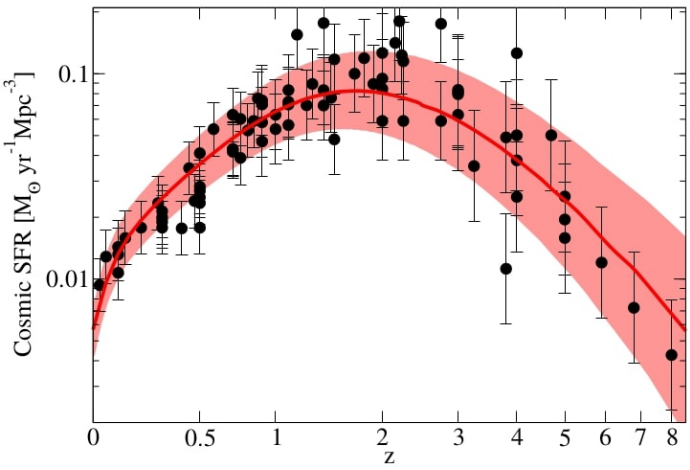

Figure 1.3: The star formation rate density (SFRD) of the Universe as a function of redshift (from Figure 3 of Behroozi et al. [2013]) based on the data from Madau and Dickinson [2014]. Shown in black dots with error bars are observations from the ultraviolet and infrared spectrums (listed in Table 1 of Madau and Dickinson, 2014). The red line and shaded region correspond to the best fit and the 1 sigma confidence region of the SFRD.

gradually fell. The co-moving SFRD at redshift 7 is approximately equal to that of today. The observations of the cosmic star formation history come from emission of stars in the ultraviolet, visible and infrared spectrums from the present-day to redshift 8 [Madau and Dickinson, 2014]. Due to faint luminosities, observations at high redshifts are sparse and have large error bars which is also seen in the increasing width of the 90% confidence region.

The chemical composition of the star-forming gas has a large influence on the evolution of stars and their binary interactions (§ 1.3.3) which can drastically affect the merger rate and the mass of black holes. To quantify the stellar chemistry, the metallicity Z is defined as the mass fraction of elements heavier than helium, $Z := M_{\rm m}/M_{\rm baryons}$, where $M_{\rm m}$ refers to the mass of elements heavier than helium. Commonly, the metallicity of the gas is represented relative to that of the Sun, where the value of solar metallicity $Z_\odot$ is derived from observations (for e.g., Asplund et al., 2009 find that $Z_\odot = 0.014$). Based on observations, the relative fraction of stars of a certain metallicity can be characterized by the galaxy mass and redshift of formation. The metallicity can therefore also be used to parameterize the SFR.

At high redshift ($z \gtrsim 2$), the star-forming gas in all galaxies is hydrogen, ie., of low metallicity. To understand the evolution of metallicity in the Universe, it is important to understand its evolution within a stellar lifetime. From its birth, until its death, the metallicity of a star increases due to the fusion of lighter elements into heavier elements.

This implies that at the end of a star's life cycle, the metallicity of the ejected gas from its supernova explosion is higher than the initial metallicity of the star. Therefore, with time, as large galaxies (of mass $M_{\rm Gal} \gtrsim 10^9\,{\rm M}_\odot$) host successive generations of stars, higher metallicity in the star-forming gas is accumulated. In contrast, galaxies with low mass ($M_{\rm Gal}$ $<10^9\,{\rm M}_\odot$), generally referred to as dwarf galaxies, do not have many generations of stars and hence maintain a low-metallicity environment.

1.2.1 Metallicity modeling uncertainties

Deriving the metallicity, and hence the abundance of elements heavier than helium, of star-forming gas in galaxies is not a trivial process. Observationally, it is often easier to measure the abundance of certain elements such as oxygen, $Z_{\rm O/H} = 12 + \log_{10}({\rm O/H})$, where (O/H) represents the abundance ratio of oxygen to hydrogen. The abundance ratio of other elements is usually assumed to scale linearly with that of oxygen, maintaining the abundance ratio with respect to that of the Sun, ie., $\log_{10}({\rm Z/Z}_\odot) = \log_{10}({\rm O/H}) - \log_{10}({\rm O/H})_\odot$ where ${\rm Z/Z}_\odot$ represents the relative metallicity with respect to the Sun. However, this assumption is not necessarily true. For example, oxygen and iron are released into the interstellar medium of galaxies by different sources and evolve with drastically different timescales (10 Myr and 1 Gyr respectively) [Tinsley, 1979, Nomoto et al., 2013]. As a result, metallicity measurement from (O/H) abundance deviates from direct measurements of metallicity by redshift 2. Comparison of the measurements of the two abundances in high redshift ($z \gtrsim$ 2) galaxies [Steidel et al., 2016, Cullen et al., 2021, Strom et al., 2022] shows that the metallicity derived from (O/H) is significantly overestimated.

To model the metallicity of star-forming gas in galaxies based on observations, the mass-metallicity relation (MZR) describes the mean metallicity of the gas as a function of galaxy mass and redshift. Modeling the MZR strongly depends on the method used to approximate the oxygen abundance (O/H). Different calibrations can be used to estimate (O/H) and different fits are used to extrapolate the MZR to high redshifts. The metallicity inferred from the spectra of massive stars is from measurements in the nearby Universe.

The direct method of estimating (O/H) involves measuring auroral lines from the HII-regions. However, these emission lines are typically weak (although observable at high z ($\simeq$ 3) with JWST, Rieke et al., 2019). Instead of direct measurements of (O/H), several calibrations have been used to estimate the oxygen abundance from stronger emission lines. Popular calibrations include Pettini and Pagel [2004], which use measurements of the gas electron temperature, Kobulnicky and Kewley [2004] and Tremonti et al. [2004], which are based on the photo-ionization mechanism, and large redshift measurements from deep near-IR spectroscopy as done in Maiolino et al. [2008], later refined by Mannucci et al. [2009]. Beyond the local universe, the metallicity can be measured at $z \simeq 3$ where the ultraviolet light from the galaxy spectrum is affected by the stellar emission (Damped Lyman α (DLA) measurements Rafelski et al., 2012) and is redshifted into the sensitivity band of optical

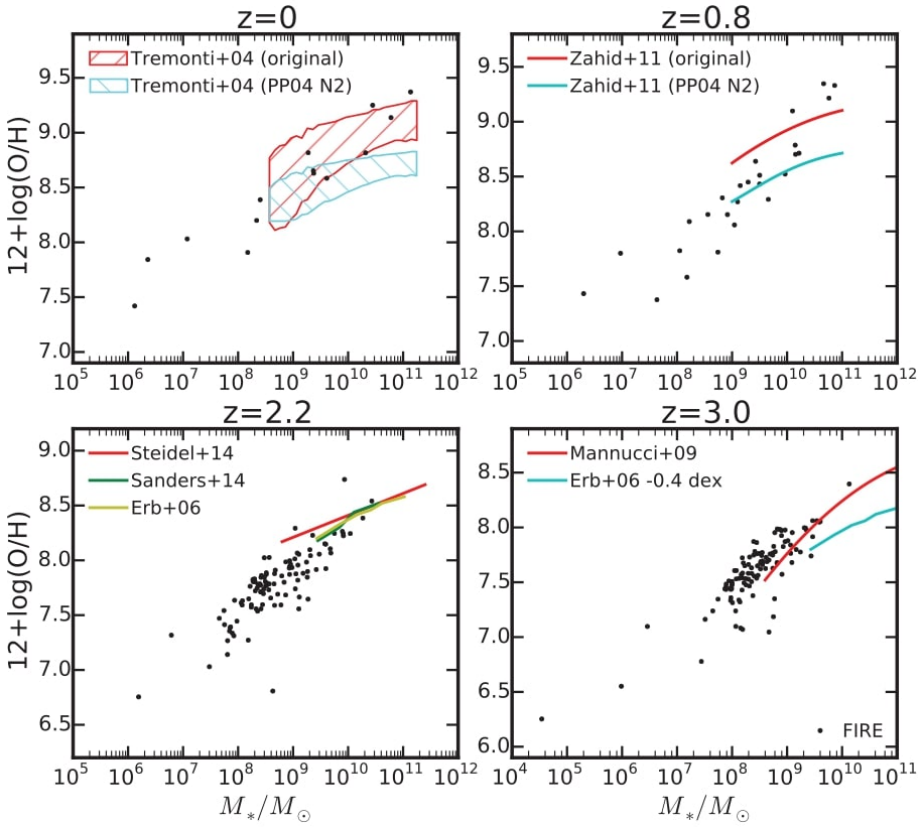

Figure 1.4: The stellar mass-gas phase oxygen abundance relation at redshifts = 0, 0.8, 2.2, 3 from different observations with different calibrations (colored lines and shaded regions), and cosmological zoom-in simulations (black dots) from Figure 6 of Ma et al. [2016]. The upper panels highlight the change in the relation using different calibrations for the two observations.

telescopes. At higher redshifts ($z \gtrsim 3$), measurements can be sparse, and a combination of different observational techniques and simulations must be used. Therefore, connecting low and high redshift measurements of the MZRs can be challenging.

Observations and simulations of different galaxy masses and their corresponding gas phase oxygen abundance, ie., $Z_{\mathrm{O/H}}$ are shown in Figure 1.4. Generally, the galaxy mass - oxygen abundance relation shifts to lower metallicities with increasing redshift. This is consistent with the narrative that the Universe was initially full of low-metallicity gas, which over time were polluted with heavier "metals" from successive generations of stars.

Modeling the metallicity as a function of galaxy mass and redshift ignores the range in metallicity seen across galaxies of a given mass. Observations of the metallicity in the Milky Way [Bergemann et al., 2014] highlight the variance of the metallicity about the mean metallicity of the MZR. This scatter in the metallicity about the MZR can result from differences in the galaxy type [Tremonti et al., 2004], from differences at a given galactocentric radius [Berg et al., 2013], from radial variations within a galaxy [Henry et al., 2010], and from the low-metallicity concentration seen in the outskirts of galaxies [Chakrabarti et al., 2017]. The importance and effect of metallicity on stellar and binary evolution will be made clear in § 1.3.3 and § 2.2.3

1.2.2 Initial condition of binary stars

Star formation occurs when pockets of over-density of star-forming gas begin to collapse inwards due to their self-gravity [Stahler and Palla, 2004]. The density and temperature of the gas increase in a runaway process that ultimately forms high-density hot cores which eventually form the stars of the galaxy. In the context of forming binary stars, it is important to include the fraction of binaries in stellar systems. The binary fraction of massive stars seems to be independent of metallicity [Moe and Di Stefano, 2017]. Observations of massive stars indicate that this is likely to be 0.7 [Sana et al., 2012]. Before modeling the evolution of binary systems, one must consider the initial conditions of the binary. The initial mass function (IMF) of stars is an observation-based model of the mass of stars at the time of formation. Initial studies used a power-law distribution of the IMF, originally adopted by Salpeter [1955] based on the observed luminosity function of stars. More modern forms of the IMF like the one by Kroupa [2001] use a series of power-laws to describe the IMF for all masses. There exist large uncertainties across different models of IMF for low-mass stars $M \lesssim 0.2\ \mathrm{M}_{\odot}$ [Thies and Kroupa, 2007, Thies and Kroupa, 2008, Kroupa et al., 2013]. This arises due to a number of observational biases and systematic uncertainties in the observation of the luminosity function and converting it to an IMF [Jeffries, 2012, Luhman, 2012]. However, stars with higher masses have an IMF that is better agreed upon by different models. Figure 1.5 shows the IMF of different models from Offner et al. [2014]. Note the discrepancy in the models at low mass and the general agreement at higher stellar-mass $M \gtrsim \mathrm{M}_{\odot}$. In this manuscript, for the purpose of creating binary black holes, I focus on

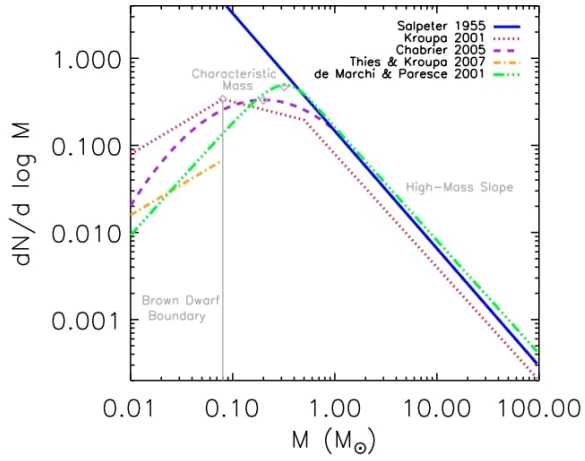

Figure 1.5: Comparison of the initial mass function (IMF) of different models from Figure 1 of Offner et al. [2014]. For stars more massive than the Sun, the IMF is consistent across models.

stars that are more massive than the Sun ($\sim 20\ M_\odot$). However, the uncertainties in the low mass spectrum result in the uncertainty in the overall normalization of the IMF. In a binary system, the mass of the primary star follows the IMF. Mazeh et al. [1992] have shown that the mass ratio of the binary, based on observations of 23 nearby systems, approximately follows a uniform distribution, slightly favoring higher mass ratios. The mass of the secondary is determined by the sampled value of the primary mass and mass ratio.

Finally, uncertainties from the initial conditions of binary systems can arise from the orbital parameters. From more than 20 massive star surveys, Moe and Di Stefano [2017] found correlations between the stellar masses, periods, and eccentricities, which I have ignored here, instead, using the data from Sana et al. [2012]. Incorporating the correlated initial binary parameters of Moe and Di Stefano [2017] in their BPS simulations, Klencki et al. [2018] find that the global merger rates of binary black holes decrease by about a factor 2. Tang et al. [2020] perform a similar analysis with their binary model and show an increase in the merger rate by a factor of two. These different findings indicate that one should be careful when introducing new uncertainties and that generalization should be done with caution.

1.3 Binary evolution of stars into black holes

1.3.1 Typical massive single star evolution

Massive stars (with a mass of a few tens to hundreds of $M_\odot$) are formed from the collapse of star-forming gas called molecular clouds or nebulae. At the time of formation, the star begins its evolution in the main-sequence (MS) phase. MS stars have a characteristic temperature and brightness that fall within a continuous band of values seen in most stars of the Universe. The star stays in the MS as long as it continues to fuse hydrogen nuclei at its core. Throughout the stellar evolution, stars continuously lose mass due to stellar winds which are expulsions of stellar material, primarily due to radiation pressure (further discussion in § 1.3.4). The mass loss due to winds increases with increasing metallicity due to enhanced opacity in the stellar atmosphere.

As the stellar core exhausts its hydrogen supply, fusion stops. The resulting absence of radiation pressure to counteract the gravitational attraction causes the core to contract. After the completion of hydrogen buring, the star briefly enters the Hertzsprung gap (HG) stage. As seen on a Hertzsprung-Russel diagram, very few stars populate the HG region due to the transient nature of this stage, hence the "gap". Soon after transitioning into an HG, the contracting core heats to a temperature when helium begins to undergo fusion and the star begins its supergiant evolution, characterized by its large stellar radius. The core progressively fuses heavier elements such as carbon, oxygen, neon, etc, until eventually forming an iron core and the fusion ends. At the culmination of the fusion process, the core of the massive star collapses. Depending on properties of the star and its core, some of the massive stars can undergo a direct collapse to form a black hole [Mapelli, 2021c], while others can undergo a supernova explosion that results in a compact object. The supernova explosion results in the expulsion of ejecta material, although, a likely stage in the process is the fallback of some ejecta back into the core. In the case of a supernova explosion, stars with a pre-supernova mass $\gtrsim 8\ M_\odot$ result in the formation of a black hole or neutron star. The black hole is given a "kick" from the supernova explosion, characterized by the kick velocity. The mechanism of the supernova and its associated kicks are further discussed in § 1.3.4.

1.3.2 Typical binary evolution of massive stars

Binary black holes (BBHs) can be formed from the binary evolution of massive stars. The evolution depends on many parameters that describe both the evolution of single stars and their binary interactions. The process begins with the massive stars formed in the MS denoted as the zero-age main sequence (ZAMS) stage. Like in the case of single-star evolution, these stars continuously lose stellar material through winds.

A mass transfer can initiate when the stellar radius of one star (donor) exceeds its Roche lobe, resulting in a stable mass transfer from the donor to the accretor star. Stable mass transfers result in a change in the binary separation through the conservation of orbital angular momentum. The mass transfer ends when the donor star no longer overflows its Roche lobe. However, if the donor keeps expanding as a result of the mass loss or if the separation keeps decreasing, the mass transfer can occur on a dynamical timescale and undergo a run-away process of unstable mass transfer which results in mass from the donor star lost to a common envelope (CE) surrounding the binary [Ivanova et al., 2013]. This process leads to a significant loss in the mass and orbital momentum of the system [Webbink, 1984b, Mapelli, 2020]. The CE provides a drag on the system, significantly shortening the system's orbit. If the orbital energy is large enough to eject the common envelope, the unstable mass transfer phase ends. However, failure to eject the common envelope will result in the stellar merger of the binary.

The BBH is formed when both stars eventually undergo supernovae explosions. During these explosions, a significant fraction of mass can be ejected, and the remaining mass collapses to form a black hole remnant. However, depending on the mass of the pre-supernova star, the amount of mass that is ejected can vary, sometimes even leaving behind no remnant. This is the case with the Pair-Instability supernova (PISN) [Rakavy and Shaviv, 1967, Fryer et al., 2001]. The PISN occurs in massive stars (typically 130 - 250 $M_\odot$) where the electron-positron pair production drains away the radiation energy from the star. This results in a partial collapse and a subsequent runaway thermonuclear explosion that leaves no remnant. Stars below the PISN mass range, specifically between 100 and 130 $M_\odot$, can undergo a pulsational pair-instability supernova (PPISN). Much like the PISN, the PPISN is driven by spontaneous electron-positron pair production. However, due to the relatively lower mass of the star in comparison to the PISN case, the star is not blown away. Instead, mass is lost through successive smaller explosions until eventually, the core collapses, leaving behind a black hole.

Associated with a supernova explosion is the kick imparted to the black hole. Supernova kicks can impact the final fate of the BBH by modifying its orbit and potentially unbinding the binary. These natal kicks are imparted by the conservation of momentum of the binary due to the mass lost as ejecta [Blaauw, 1961] and possibly because of asymmetric stellar collapse [Janka and Mueller, 1994, Burrows and Hayes, 1996]. Once the black holes are formed, through the emission of GWs, the binaries gradually lose orbital angular momentum and spiral inward until eventually merging. The relation of the delay time $t_{\rm delay}$ between the time of the formation of the BBH and its merger [Peters and Mathews, 1963] is as follows,

$$t_{\rm delay} = \frac{5a^4c^5}{256\,G^3\,\mu\,M_{\rm Tot\,BBH}^2}, \tag{1.1}$$

where $M_{\rm Tot\,BBH}$ represents the total mass of the black holes, μ represents the reduced mass

of the BBH given by $(M_{1\,\mathrm{BBH}} * M_{2\,\mathrm{BBH}})/(M_{1\,\mathrm{BBH}} + M_{2\,\mathrm{BBH}})$, and a represents the separation at the time of formation of the BBH. As t_{delay} is proportional to a^4, the delay time can have a wide range of values, from tens of million years to the order of a Hubble time or more. Therefore, for the purpose of forming merging BBHs, it is vital that at the time of formation of the BBHs, the orbital separation should be small (a few tens of stellar radii); highlighting the importance of processes like mass transfer and kicks that influence the separation.

Figure 1.6 depicts an example of the binary evolution of stars that ultimately form a BBH with masses comparable to the first GW detected system. The binary stars are initially in the ZAMS stage. After about 3.9 Myr, one of the stars completes its hydrogen burning in the core, and enters the transient HG phase. Soon afterwards, the star becomes a giant, overfills its Roche lobe, and begins a phase of stable mass transfer between the donor (itself) and the accretor (the secondary MS) star. During this period of mass transfer, the orbital separation changes due to angular momentum conservation. After the mass transfer, the donor star becomes a small, stripped, naked helium MS star, and the secondary MS star has grown significantly in mass from the accretion. At this stage, each star evolves through their life cycles. Eventually, at about 4.2 Myr, the primary star undergoes a supernova explosion and forms black hole. The resulting supernova kick increases the orbital separation slightly and imparts a small eccentricity to the orbit. After 1.6 Myr, the secondary burns through the hydrogen in its core, evolves into a HG star, and soon after expands into the giant phase. This time, the secondary rapidly overflows its Roche lobe and a mass transfer is initiated between the secondary donor and the primary black hole. However, the mass transfer occurs on a dynamical timescale and a runaway process leads to the formation of a CE surrounding the binary. The CE significantly shortens the orbit until eventually being ejected, leaving behind a black hole-naked helium star binary 39 $R_\odot$ apart. Soon after, the star undergoes a supernova explosion, and collapses into a black hole. Thus forming a BBH with component masses 25.6 $M_\odot$ and 30 $M_\odot$. The orbital energy is slowly lost through the emission of GWs until, after nearly 13.4 Gyr, the BBH merges to form a single black hole of mass 55 $M_\odot$. In this simulation, 0.6 $M_\odot$ of the total BBH mass is emitted as GW radiation.

1.3.3 Influence of metallicity in stellar evolution

To effectively model the binary stellar evolution of stars until eventually merging as binary black holes, it is important to understand the effect of metallicity in stellar evolution and binary interactions. For massive stars, the effect of metallicity is most prominent in wind-driven mass loss [Pauldrach et al., 1986, Kudritzki et al., 1987, Vink et al., 2001, Mokiem et al., 2007, Gräfener and Hamann, 2008, Puls et al., 2008, Vink and Sander, 2021]. Depending on the atmospheric opacity of the star, radiation pressure can interact with the atmosphere and drive stellar winds. Stars with higher metallicity have a higher atmospheric opacity, resulting in a larger mass loss due to winds. In addition to mass, winds also carry angular momentum from the star [Maeder and Meynet, 2000]. In comparison to high Z

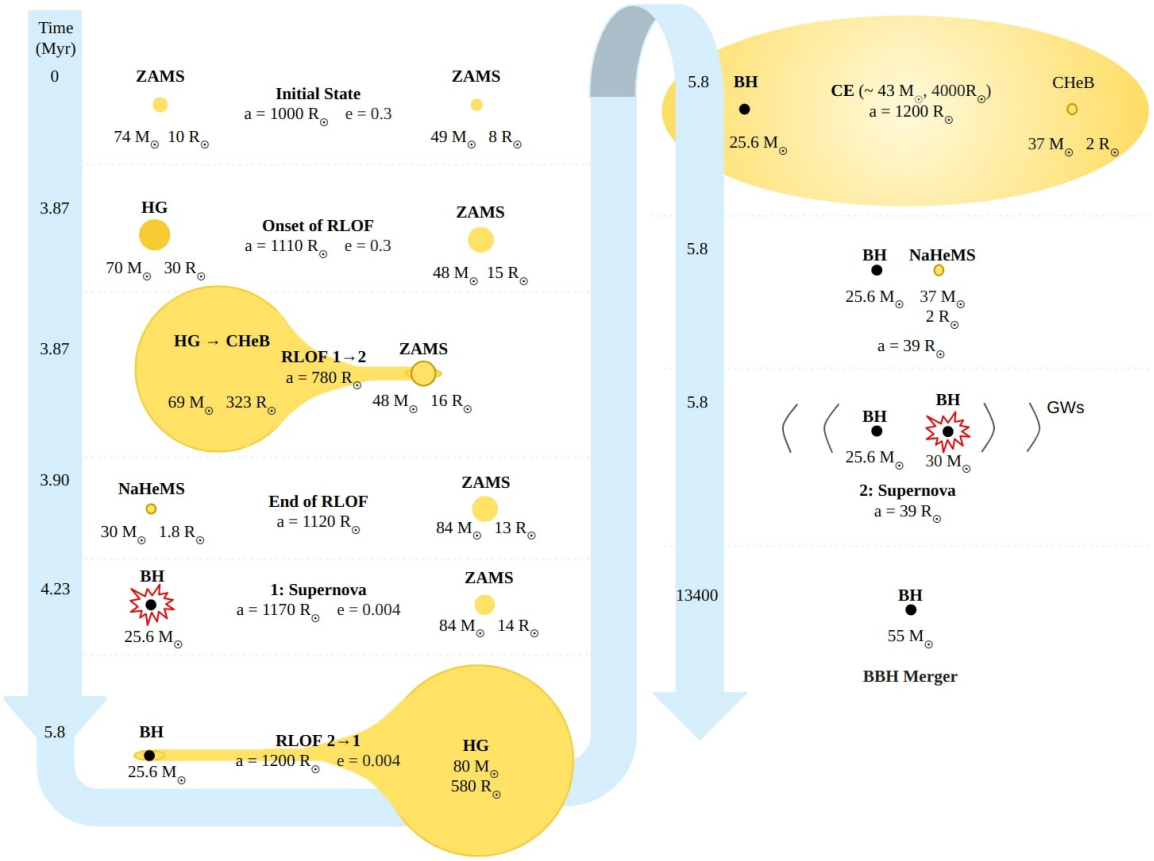

Figure 1.6: Example of a binary evolution of stars that eventually form binary black holes with masses similar to that of the first GW detection (GW150914). I made this illustration based on the output of a simulation produced using a binary population synthesis (BPS) code, COSMIC [Breivik et al., 2020]. The stage of the evolution is shown in the center of each column and the time of the evolution is shown on the left. Also shown in relevant locations are the mass, distance of separation, and the eccentricity of the orbit. The size and distance between the circles are indicative of the masses and separation of the binary (although not to scale). Acronyms: RLOF - Roche lobe overflow, CE - common envelope, ZAMS - zero-age main sequence star, HG - Hertzsprung gap, CHeB - core He burning, NaHeMS - naked helium main sequence, and BH - black hole, GWs - gravitational waves.

stars, this implies that massive low Z stars have a lower wind-driven mass loss and are more likely to retain their angular momentum, thus likely to form high-spinning massive black holes.

In binary star systems, the mass and angular momentum loss from winds can result in changes to the orbital separation [Schrøder et al., 2021] such that pronounced mass loss in higher metallicity systems results in wider binaries. Brunish and Truran [1982] and Baraffe and El Eid [1991] show that the radius of a star and, hence, its Roche lobe, depends on its metallicity. As a result, metallicity also plays a role in determining mass transfers between the star overflowing its Roche lobe and its companion. This has far-reaching implications as mass transfers play a pivotal role in determining the separation of the system, governing whether they merge within the age of the Universe. Mass transfers can also result in stripped stars that lack an envelope. Stripped stars tend to eject less mass than typical stars when undergoing a supernova explosion. Thus, these systems have low supernova kicks, increasing the likelihood of forming bound compact binaries.

1.3.4 Binary models and their uncertainties

Numerical simulation codes like the MESA code [Paxton et al., 2011] provide accurate simulations of stars but at the cost of being computationally intensive and time-consuming. The MESA code is a numerical, 1-dimensional single-star evolution code that is especially good at predicting the internal structure and evolution of the star. However, the simulation ends at the pre-supernova stage. The MESA code has also been adopted for binary star systems using semi-analytical models of binary interactions. The binary interactions and supernova mechanisms are determined by analytical models similar to those used in population synthesis codes. Moreover, most population studies require the evolution of millions of binaries. Therefore, numerical simulations are not a feasible option. As an alternative, I resort to codes that use semi-analytical prescriptions of different stages of binary and single-star evolution. Such binary population synthesis (BPS) codes provide a fast, albeit approximate, evolution of a population of binary stars. The first widely used BPS code was developed by Hurley et al. [2002], which forms the basis of many modern BPS codes. In Hurley et al. [2002], prescriptions of the different evolution stages are denoted by flags and their values. The formation of merging BBHs is mostly affected by the choice of the flags (or models) of stellar winds, mass transfers, and supernova mechanisms. In the following paragraphs, I elaborate on popular prescriptions for these phenomena.

Higher metallicity stars tend to have larger winds. Therefore, most wind prescriptions [Vink et al., 2001, Vink and de Koter, 2005] have a metallicity dependence. Relevant to black hole formation, wind parameters like the wind velocity factor and the mass loss near the Eddington limit can play an important role in determining the mass of the final black hole. The wind velocity factor is a proportionality constant equating the wind velocity to the surface escape velocity of the star (Eq. (9) of Hurley et al. [2002]). As described

in Belczynski et al. [2008], the velocity factor for massive stars can take different values depending on the metallicity and evolutionary stage of the donor star. For example, it can have high values ($\simeq 7.0$) for high-metallicity stars, while low-metallicity giant stars have low values ($\simeq 0.125$). The prescription for the mass loss near the Eddington limit can be metallicity independent or can be modeled based on the metallicity [Giacobbo et al., 2018].

Modeling the CE requires 3D hydro-dynamical simulations that are not feasible in rapid population synthesis. Instead, BPS codes typically use a simplified model of Eq. (71) in Hurley et al. [2002], adapted from the principles of Paczynski [1976], Webbink [1984a],

$$E_{\rm bind\,CE} = \alpha_{\rm CE}(E_{\rm orb\,f} - E_{\rm orb\,i}), \tag{1.2}$$

where $\alpha_{\rm CE}$ is the CE efficiency defining the efficiency of transferring orbital energy to the envelope. $E_{\rm bind\,CE}$ is the total binding energy of the envelope, $E_{\rm orb\,i}$ and $E_{\rm orb\,f}$ show the orbital energy of the binary at the onset and ejection of the CE. Eq. (1.2) assumes that the envelope is ejected, ie., the final binding energy of the CE is zero. Large uncertainties are associated to the CE efficiency. As a result, $\alpha_{\rm CE}$ can usually have a wide range of values; from 0.1 to 10. The total binding energy of the envelope, $E_{\rm bind\,CE}$, is related to the sum of the binding energy of the envelope with the component masses by a binding energy factor. Popular prescriptions of the binding energy factor include a fixed value like 0.5 (Eq. (69) of Hurley et al., 2002) or a variable prescription, as given in the Appendix of Claeys et al. [2014]. The variable prescription, based on the results of the STARS code [Eggleton, 1971, Pols et al., 1995], assigns different values of the binding energy factor based on whether the star is hydrogen-rich or helium-rich. For example, in hydrogen-rich stars, the binding energy factor is a function of the mass of the convective envelope to distinguish between stars with radiative and deep convective envelopes. The prescription also depends on the type of star (e.g. Main sequence, HG, AGB). Uncertainties also exist in the calculation of the initial orbital energy ($E_{\rm orb\,i}$). For example, one method is to calculate the orbital energy with just the binary's core masses as per Eq. (70) of Hurley et al. [2002],

$$E_{\rm orb,i} = \frac{{\rm G}M_2(M_{\rm e} + M_{\rm c1})}{2a_{\rm i}}, \tag{1.3}$$

or with core + envelope mass from the de Kool [1990] prescription,

$$E_{\rm orb,i} = \frac{{\rm G}M_{\rm c2}M_{\rm c1}}{2a_{\rm i}}, \tag{1.4}$$

where $a_{\rm i}$ is the initial separation and $M_{\rm e}$, $M_{\rm c1}$, M_2, $M_{\rm c2}$ are the masses of the envelope, core of the primary star, secondary star, and the core of the secondary star respectively. Finally, the onset of CE is determined by the critical mass ratio of the donor and accretor stars which depends on the state of the donor star (MS, HG, Asymptotic Giant Branch, etc). Uncertainties and different assumptions have led to multiple competing critical mass ratio

models [Hjellming and Webbink, 1987, Hurley et al., 2002, Belczynski et al., 2008, Claeys et al., 2014, Neijssel et al., 2019].

An accurate supernova kick model is essential to evaluate the final separation of black holes or even the disruptions of binaries. Unlike neutron stars, we do not have observational data for black hole kicks and must instead base models on neutron star data. Observations of pulsar kicks show a Maxwellian distribution with the dispersion parameter set to 265 km/s. Black hole kick models are modifications to the distribution of pulsar kicks. Popular models prescribe the supernova kick of black holes by re-scaling the observed distribution of neutron star kicks using the conservation of momentum involving different functions of the ejecta mass, remnant mass, and initial masses [Bray and Eldridge, 2016, Giacobbo and Mapelli, 2020].

The prescription of the supernova can influence the mass of the remnant drastically. Some models account for a fallback of ejecta material back into the core of the proto-neutron star at the center of the supernova. This can occur when the material that is initially shocked away from the core interacts with in-falling matter and slows below the escape velocity. Depending on the delay between the supernova explosion and the fallback of matter, one can have a rapid or delayed fallback of matter [Fryer et al., 2012] which can determine the presence or absence of a mass gap between neutron stars and black holes. The PISN and PPISN mechanisms are modeled by simulations of single star evolution of massive stars [Marchant et al., 2019, Woosley, 2019] and can also include the effect of close binaries on the supernova mechanism [Spera and Mapelli, 2017].

1.3.5 Example of a binary population evolution

To illustrate the results of a BPS simulation, I show, in Figure 1.7, the relation between the total ZAMS mass and the mass of the post-merger remnant black hole for different metallicities using the default models of the BPS code, COSMIC [Breivik et al., 2020]. High metallicity binaries tend to have light pre-supernova stars which can hamper BH formation or result in small BHs. This is due to high winds causing large mass loss during the evolution of the binary. The low-mass BHs are subject to large BH kicks, potentially disrupting the binary. Irrespective of metallicity, there appear to be two channels of binary evolution based on whether the binary was formed with equal mass or not. Systems with nearly equal masses have similar stellar evolution timescales. During their evolution, the binaries enter giant phases together, where both stars undergo a common envelope phase where their respective stellar envelopes are stripped, leaving behind a naked helium core. The double CE event results in significant mass loss. Hence, equal mass ZAMS tend to form smaller remnants. In contrast, unequal mass ZAMS stars do not necessarily both undergo CE, thus resulting in lower mass loss and larger remnants. The drop in final remnant mass for total ZAMS mass $\gtrsim 170\ M_\odot$ is due to the present default PISN prescription in COSMIC. As shown in Table 1 of Marchant et al. [2019], as the pre-supernova mass of the progenitor

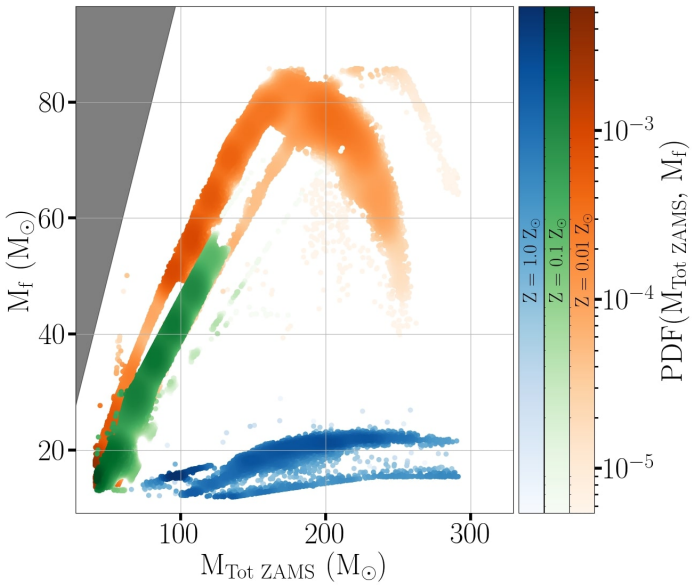

Figure 1.7: Remnant black hole mass M_f versus total initial stellar mass $M_{Tot\ ZAMS}$ from my default binary population synthesis simulation for metallicities 0.01 $Z_\odot$ (red), 0.1 $Z_\odot$ (green) and 1.0 $Z_\odot$ (blue). The color map represents the probability density function for each metallicity.

stars increases beyond $\gtrsim 50\ M_\odot$, there is significant mass loss due to the PPISN mechanism resulting in a black hole with progressively smaller mass.

1.4 Gravitational waves from binary black holes

GWs are solutions to Einstein's equations and they manifest as space-time deformations that travel at the speed of light. GWs are generated when an accelerating mass causes the quadrupole moment tensor to vary with time [Maggiore, 2007]. So far, the only GW sources that are detectable by ground-based detectors are coalescences of compact binary objects (black holes or neutron stars). In the following sections, I describe the properties and detection of GWs from these compact binary coalescences.

1.4.1 Gravitational wave properties

The GW emission from a compact binary has three basic stages, namely, the inspiral, merger, and ringdown. The evolution of the waveform during the inspiral can be approximated by post-Newtonian expansions. The merger, due to the highly non-linear regime of gravity, is obtained using numerical relativity simulations. And, the ringdown waveform follows

an exponentially damped sinusoid. For accurate GW simulation, we are required to model these three phases. General relativity dictates that these waves have two polarizations. Using the far-field approximation to simplify the equations for GWs from distant merging compact binaries, the GW strains for the two polarizations are

$$h_+(t) = \frac{4}{c^4 D_{\rm L}}(G\mathcal{M})^{5/3}(\pi f_{\rm GW})^{2/3}\left(\frac{1+cos^2\iota}{2}\right)cos(2\pi f_{\rm GW}t+\phi_0), \tag{1.5}$$

$$h_\times(t) = \frac{4}{c^4 D_{\rm L}}(G\mathcal{M})^{5/3}(\pi f_{\rm GW})^{2/3}cos\,\iota\, sin(2\pi f_{\rm GW}t+\phi_0), \tag{1.6}$$

where h_+ and $h_\times$ are the "plus" and "cross" polarizations. $D_{\rm L}$ is the luminosity distance to the source, t is the time, and ι is the inclination defined as the angle between the line of sight of the source and the axis of rotation of the binary. During the inspiral of the binary, the frequency $f_{\rm GW}$ of the GW (which is twice the orbital frequency for circular binaries) is given by:

$$f_{\rm GW}(t) = \frac{1}{\pi}\left(\frac{5}{256}\frac{1}{(t_{\rm c}-t)}\right)^{3/8}\left(\frac{G\mathcal{M}}{c^3}\right)^{-5/8}, \tag{1.7}$$

where, $t_{\rm c}$ is the time of coalescence (such that t $<$ $t_{\rm c}$) and $\mathcal{M}$ is the chirp mass of the binary, defined as,

$$\mathcal{M} = \frac{(m_1 m_2)^{(3/5)}}{(m_1+m_2)^{(1/5)}}, \tag{1.8}$$

where m_1 and m_2 are the component masses in the detector frame of reference, ie., the redshifted masses. The detector frame and source frame masses are related as $M_{\rm Detector} = M_{\rm Source}(1+z)$, where z is the cosmological redshift. Eq. (1.7) shows that the frequency increases with time indicating that the orbital frequency also increases. Conservation of angular momentum dictates that the orbit must therefore shrink until eventually merging. Like the inspiral, the frequency of the merger is also determined by the masses and is approximately equal to $15\,kHz/(m_1+m_2)$ Centrella et al. [2010].

As briefly mentioned in § 1.3.2 and shown in Figure 1.6, the delay time between the formation of the BBH and its eventual merger can be very large and is almost always the stage of binary evolution with the longest time duration. This is due to the relatively low amount of orbital energy that is lost in the form of GWs, at least during the inspiral. Current GW detectors are only able to detect the high frequency parts of the signal, ie., the pre-merger and merger phases of BBHs. As a result, we can only detect the GWs of BBHs that merge. Hence, the delay time is an important factor that determines GW sources that are detectable.

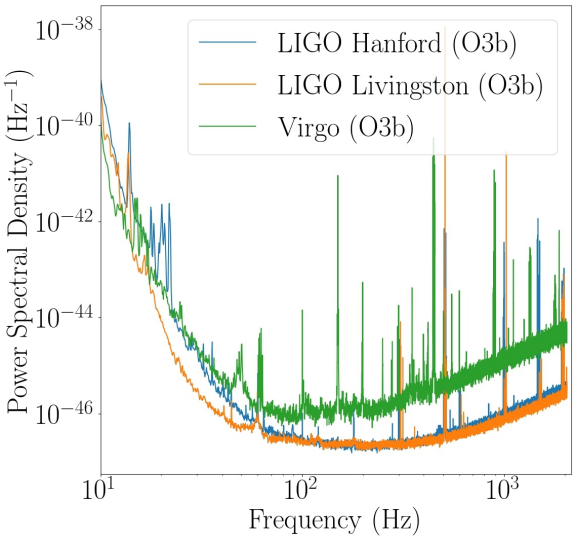

Figure 1.8: Power spectral density of the three GW detector network during the second half of the third observing run (O3b) of the LIGO-Virgo-Kagra collaboration [Abbott et al., 2023].

1.4.2 Gravitational wave detector network

Ground-based GW detectors are based on the Michelson's interferometer and are capable of detecting strain amplitude of the order 10^{-21}. At the time of writing the thesis, the GW detectors that are observing sources formed a 3-detector network of LIGO Hanford, LIGO Livingston, and Virgo, with a fourth detector, KAGRA, that has just become operational. LIGO Hanford and LIGO Livingston are located in the USA, Virgo is in Italy, and KAGRA is located in Japan. The 'L' shaped detectors have perpendicular arms, each of length 4 km for the two LIGO detectors and 3 km for the Virgo and KAGRA detectors. A larger number of detectors helps improve the sky sensitivity of the network of detectors and helps increase confidence in the detection of a particular GW. The GW detectors have an antenna response function, F_+ and $F_\times$, that describes the response of the detector to each polarization and which depends on the sky position of the source. The measured strain, h(t), is the projection of the two GW polarizations onto the antenna response function of the detector

$$h(t) = F_+(\theta, \phi) \times h_+(t) + F_\times(\theta, \phi) \times h_\times(t), \tag{1.9}$$

where θ and ϕ are the source sky coordinates.

The noise and the frequency response of a detector are fully characterized by the one-sided power spectral density $S_n(f)$ which is given by the Fourier transform of the auto-correlation of the noise in the detector

$$S_n(f) = 2\int_{-\infty}^{\infty} \langle n(t+\tau)n(t)\rangle e^{-i2\pi f\tau} d\tau, \tag{1.10}$$

where the angle brackets $\langle\ \rangle$ denote an ensemble average over many noise realisations. Figure 1.8 shows the one-side PSD, $S_n(f)$, of the three GW detectors during the third GW observing run (in early 2020). As louder signals are more likely to be detected, there is an observational bias towards GWs with greater amplitude, ie., massive black holes and nearby mergers. However, as shown in Figure 1.8, ground-based detectors are typically sensitive to GWs with frequencies greater than 10 Hz which places a lower limit on the merger frequency. As a consequence, current ground-based detectors can detect GWs from black hole mergers up to a total mass of a few hundred $M_\odot$. To quantify the strength of the signal, one uses the optimal signal-to-noise ratio (SNR), $\rho_{\rm opt}$ described below

$$\rho^2_{\rm opt} = 4\int_0^{+\infty} \frac{|\tilde{h}(f)|^2}{S_{\rm n}(f)} {\rm d}f, \tag{1.11}$$

where $\tilde{h}(f)$ is the Fourier transform of the GW signal, and $S_{\rm n}(f)$ is the one-sided PSD. The optimal SNR is essentially the autocorrelation of the whitened signal.

When simulating the GW signal, one can compute the GW waveforms using often time-consuming, but very accurate, numerical relativity codes [Boyle et al., 2019] or using fast, and arguably slightly inaccurate, waveform approximations. For the purpose of this study, I use the IMRPhenomD [Hannam et al., 2014] waveform approximation that models the phenomenology of the three phases.

1.5 Unanswered questions

GW detectors have been collecting data since September 2015 with the seminal detection of GW150914. Inter-spaced between periods of observations are periods when detectors are upgraded in order to improve their sensitivity to observe further into the Universe. By the end of the third observing run of the LIGO-Virgo detectors, there have been over 80 confident detections of BBH mergers whose properties are listed in Abbott et al. [2023]. This catalog of mergers provides observational data about the rates of mergers, the mass spectrum, and spin distribution of black holes which can be used to carry out a population analysis. The fourth observing run, O4, began on 24 May 2023. At the time of writing the thesis, after just 8 weeks of observations, we already have over 20 confident GW alerts. By the end of O4, we expect to more than double the number of GW detections. With this wealth of data, the stellar physics community have begun to analyze the astrophysical origins of binary black holes. Figure 1.9 shows a mass comparison of the black holes detected via GWs and through electromagnetic (EM) observations. There is an apparent mass disparity between the two detection channels. Moreover, the spin distribution of EM-detected and GW-detected black

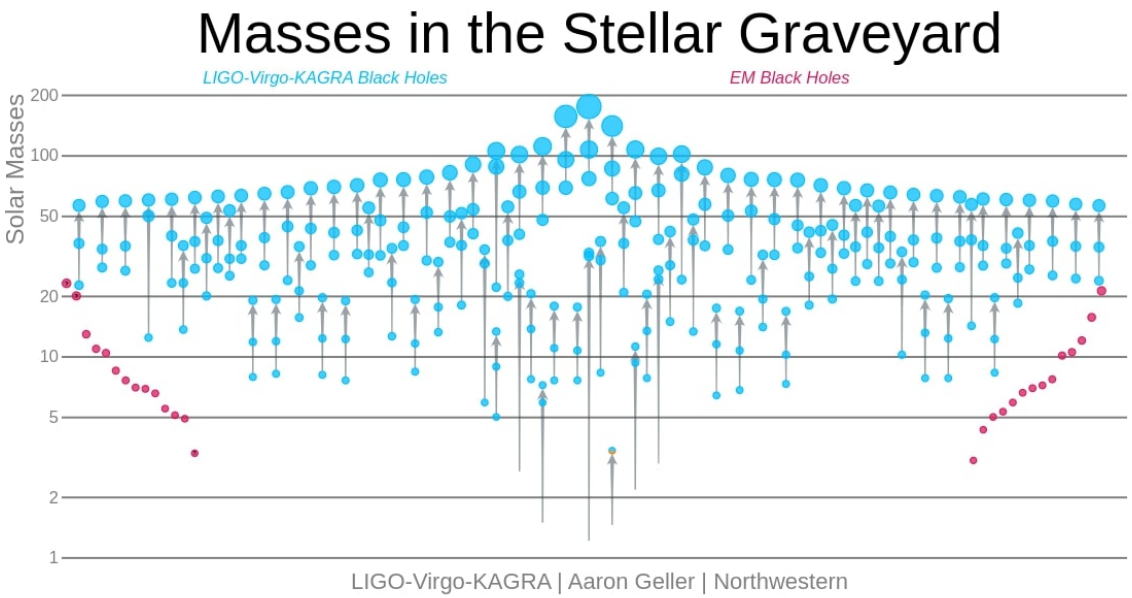

Figure 1.9: Black holes in the stellar graveyard: illustration of the black holes detected from GW (blue) and EM (red) observations by LIGO-Virgo / Aaron Geller / Northwestern University. The size of the circles are indicative (but not to scale) of the black hole mass.

holes show significant tension, at the 99.9% level [Fishbach and Kalogera, 2022]. The discrepancy between the populations of black holes (a) can potentially arise due to different observational biases between GW and EM detectors [Liotine et al., 2023], or, (b) can perhaps indicate an underlying difference in the astrophysical origins of black holes observed by the two detection channels. In this thesis, I would like to probe the latter, by understanding the environment in which these black holes form.

Typical sources of EM-detected stellar-mass black holes come from black hole X-ray binaries [Corral-Santana et al., 2016, Fortin et al., 2023]. These systems are comprised of a stellar-mass black hole in a binary with a companion star that has overflown its Roche lobe. During the stable mass transfer of gas from the star into the black hole, an accretion disk can sometimes emerge, resulting in the emission of soft or hard X-ray emission or, in some cases, soft gamma-rays. These black hole-star systems are classified into categories (low, intermediate, and high mass X-ray binaries) based on the mass of the component star. There have been around 70 candidates of black hole X-ray binaries (listed in the online BlackCAT catalog Corral-Santana et al., 2016). Most are in the Milky Way and only a few are extragalactic. We have an indication of the host galaxy and the environment within. Some information can be gathered on the metallicity based on observations of the companion star. However, in contrast to EM telescopes, current GW detectors lack the sky

and distance sensitivity to precisely locate the galaxy of black hole mergers. Therefore, the galactic environment of GW-detected binary black holes is unlikely to be observed directly.

Hence, I resort to model-based simulations that produce a representative population of the BBH mergers in the Universe to extract information about the progenitor environment. I use LVK observations of the merger rate and black hole mass spectrum [Abbott et al., 2023] to validate the veracity of a model of the Universe. I use a collection of probable models of the Universe to map merging black hole properties (like masses, distance of mergers, and merger rate) to their progenitor properties (metallicity, galaxy mass, redshift of star formation) to better understand the relation between the black holes we observe and their astrophysical environment.

Chapter 2

Merging binary black hole population simulation

To understand the progenitor environment of merging binary black holes (mBBHs), I create a set of models that combine star formation rate (SFR) models and binary stellar evolution models. I parametrize the star formation environment by the present-day formation galaxy mass $M_{\rm Gal}$, the metallicity of star-forming gas in the galaxy Z, and the redshift of star formation $z_{\rm f}$ (§ 2.1). Using a binary population synthesis code, I produce a representative population of mBBHs from binary systems with different metallicities (§ 2.2). In § 2.3, I convolve the star formation rate with the binary models to get the astrophysical merger rate of mBBHs and the formation rate of their progenitors. Finally, I generate the GW signals emitted by these systems and simulate their detection by the LIGO-Virgo three-detector network considering their sensitivity during the third observing run. I describe the construction of my simulation in the flowchart shown in Figure 2.1.

2.1 Star formation rate

The SFR describes the mass accretion rate of the formation of stars in the Universe. Typically, the SFR is represented as a function of the redshift of formation $z_{\rm f}$. However, as I am interested in eventually modeling and understanding the progenitor formation galaxy environment of merging black holes, I must also incorporate the formation galaxy properties into the SFR. The mass of the formation galaxy, $M_{\rm Gal}$, influences the amount of star-forming gas available to form binary systems. In addition, the metallicity of the star-forming gas, Z, is correlated with $M_{\rm Gal}$ and also strongly influences the evolution of the binary star systems. Thus, for the purpose of producing merger rates of binary black holes, I am interested in building a 3-dimensional model of the SFR as a function of Z, $M_{\rm Gal}$, and $z_{\rm f}$. To this end, I follow a modified version of the model proposed in Lamberts et al. [2016].

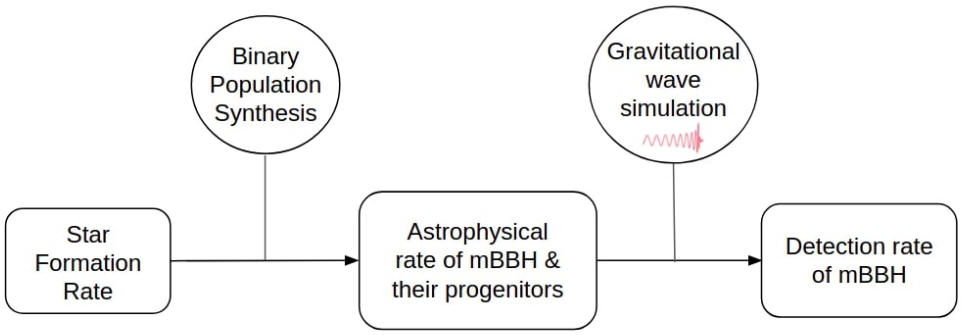

Figure 2.1: Workflow of my pipeline to simulate the merging BBH population. First, I model the star formation rate as a function of metallicity, galaxy mass, and redshift of formation. Then, the astrophysical formation rate is obtained by integrating the star formation rates with the binary population synthesis of binary stars that form merging binary black holes. The detection rate of black holes mergers is calculated by simulating the detection process of gravitational waves emitted by the astrophysical population.

2.1.1 Galaxy mass and redshift dependence of the SFR

To develop the 3-dimensional SFR, I first use the star formation history (SFH) from Behroozi et al. [2013] which provides an observation-based fit of the average SFR in a given dark-matter halo at a given redshift. I use the SFH from Behroozi et al. [2013] as it is a self-consistent relation that accounts for observational uncertainties and biases, and also implicitly incorporates the halo merger history (for more information, see discussion in § 1.1) using dark matter simulations.

Figure 2.2 shows the SFH where the average observed SFR (in units $\mathrm{M}_\odot\ \mathrm{yr}^{-1}$) is shown as a function of redshift z_f and dark-matter halo with a present-day halo mass M_Halo. Generally, massive halos have large SFRs that peak at $z_\mathrm{f} \simeq 2$. However, unlike the SFR, the efficiency of star formation in halos increases up to $M_\mathrm{Halo} = 10^{12}\ \mathrm{M}_\odot$ and falls thereafter (see discussion of Figure 1.2, left). Using the abundance matching relation between present-day halo mass and the corresponding present-day galaxy mass M_Gal, I can express the SFH as a function of M_Gal and z_f. The SFH(M_Gal, z_f) only describes the star formation for a given galaxy mass. To account for the number density of galaxies as a function of M_Gal, I use the galaxy stellar mass function $\frac{\mathrm{d}^2 N_\mathrm{Gal}(M_\mathrm{Gal})}{\mathrm{dlog}\, M_\mathrm{Gal}\, \mathrm{d}V_\mathrm{c}}$ derived from observations. For my analysis, I use the galaxy stellar mass function fitted by Tomczak et al. [2014] (Figure 1.2, right). However, it is important to note that observational errors in the galaxy stellar mass relation, especially at higher redshift, result in model uncertainties [Neijssel et al., 2019]. Multiplying the SFH(M_Gal, z_f) by the galaxy stellar mass function at $z_\mathrm{f} = 0$, I produce the SFR density (SFRD) as a function of present-day galaxy mass and redshift.

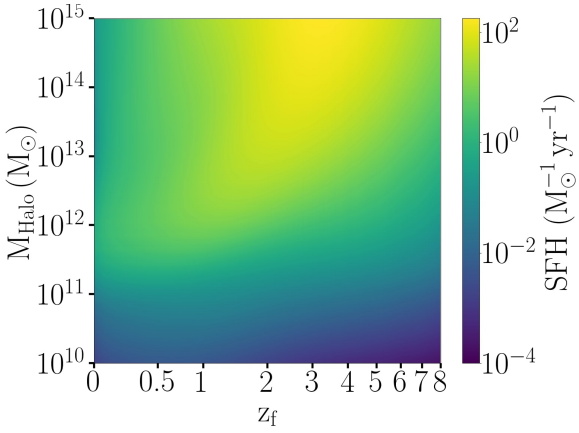

Figure 2.2: Star formation history from Behroozi et al. [2013] shown in the color map, as a function of present-day dark-matter halo mass $M_{\rm Halo}$ and formation redshift $z_{\rm f}$.

2.1.2 Metallicity dependence of the SFR

In this analysis, I assume that the solar metallicity $Z_\odot = 0.014$ [Asplund et al., 2009]. To model the metallicity of star-forming gas in galaxies, I use the mass-metallicity relation (MZR). As described in § 1.2.1, large uncertainties in the MZR arises from different calibrations. In order to probe the effect of different metallicity models in the progenitor environment of mBBHs, I incorporate the following MZR calibrations that were explored in the comprehensive study of Chruślińska [2022]: Kobulnicky and Kewley [2004], Pettini and Pagel [2004], Tremonti et al. [2004], and Mannucci et al. [2009]. I chose these calibrations also due to their large differences in the MZR. In addition, I also probe different models of extrapolating the MZR to higher redshifts ($z_{\rm f} \gtrsim 3$). I use two fits of the MZR with significantly different models at high redshifts. The first fit is prescribed in Eq. (3) and Eq. (4) and Table 2 of Chruslinska and Nelemans [2019] for the aforementioned metallicity calibrations (whose MZRs will be henceforth denoted as PP04, KK04, T04, and M09 respectively). My second fit is provided by Ma et al. [2016] for the Pettini and Pagel [2004] and Kobulnicky and Kewley [2004] calibrations (MZRs denoted as PP04_Ma16 and KK04_Ma16 respectively) which are based on high-resolution cosmological zoom-in simulations of galaxy formation using the FIRE suite [Hopkins et al., 2014] and consistent with observations at low redshift. Due to the large uncertainties in the calibrations and extrapolation to higher redshift, I explore all six MZRs in my analysis. By default, I use the MZR of KK04_Ma16 as it shows reasonable consistency with observations at low redshift.

Figure 2.3 shows the MZRs for different calibrations and redshift extrapolation considered in my analysis. The solid lines represent the fits of Chruslinska and Nelemans [2019] (Ch19) and the dashed lines are that of Ma et al. [2016] (Ma16). The Ch19 fits assumes a broken power-law in the MZR with a turnover point at $M_{\rm Gal} \simeq 10^{9.7}\,{\rm M}_\odot$. In contrast, Ma16

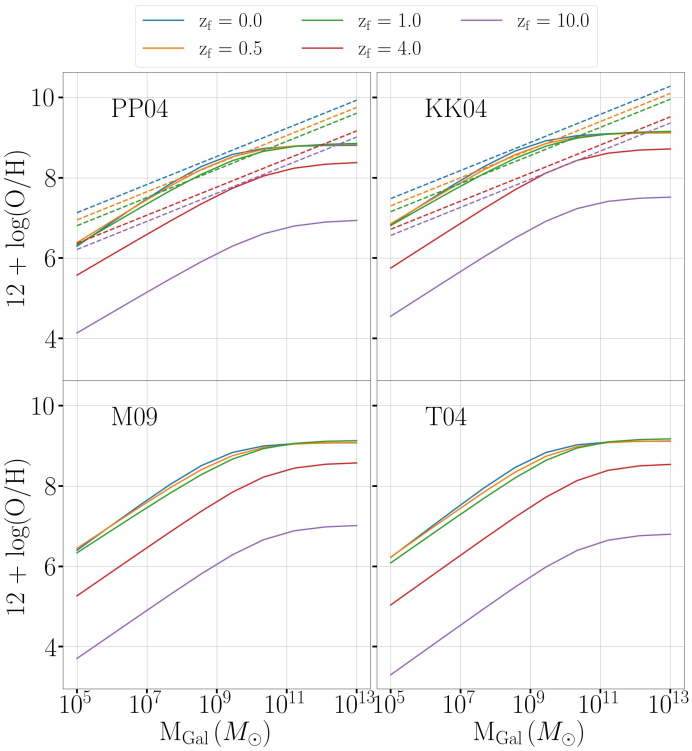

Figure 2.3: Mass metallicity relation (MZR) for different calibrations and redshift fits. The MZR is represented as a function of the oxygen abundance, 12 + log(O/H) and the galaxy mass $M_{\rm Gal}$. The colors represent the MZR at different redshifts. The calibrations with the redshift extrapolation fit are respectively (clockwise from top-left): Pettini and Pagel [2004] calibration with Ch19 [Chruslinska and Nelemans, 2019] fit (solid) and Ma16 [Ma et al., 2016] fit (dashed), Kobulnicky and Kewley [2004] calibration with Ch19 fit (solid) and Ma16 (dashed) fit, Tremonti et al. [2004] calibration with Ch19 fit, and Mannucci et al. [2009] calibration with Ch19 fit.

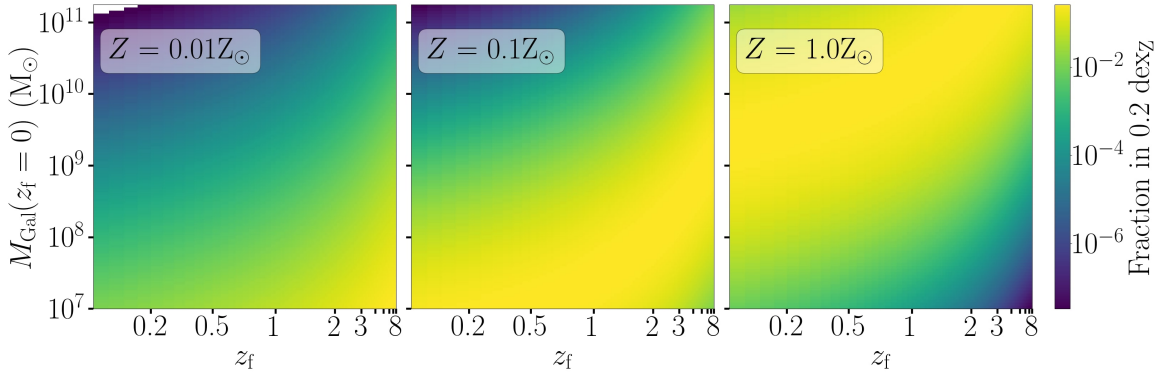

Figure 2.4: Fraction of stars in a given metallicity bin as a function of galaxy mass and redshift. The color bar represents the fraction of stars within a metallicity bin of size 0.2 dex, centered at 0.01 $Z_\odot$ (left), 0.1 $Z_\odot$ (center), and $Z_\odot$ (right) respectively. The white regions contribute to near-zero star fraction.

assumes a power-law description of the MZR. Moreover, comparing the MZR extrapolation at high redshift ($z_{\rm f} \gtrsim 2.5$), Ma16 shows very little variation, whereas Ch19 extrapolates the low redshift trend of the MZR to high redshifts as well. Hence, Ch19 shows a constant shift of the MZR towards lower metallicities with increasing redshifts, without changes to its dependence on galaxy mass.

Accounting for variance around the mean metallicity, I approximate the metallicity distribution in a galaxy as a Normal distribution $\mathcal{N}$ with a mean metallicity from the MZR and a scatter σ of three origins: $\simeq 0.1$ dex due to differences between galaxies [Tremonti et al., 2004], $\simeq 0.2$ dex due to radial variations within a galaxy [Henry et al., 2010] and $\simeq 0.2$ dex for differences at a given galactocentric radius [Berg et al., 2013]. Adding the contributions in quadrature, I get $\sigma = 0.3$ dex. Thus, the fraction $\Psi(Z,M_{\rm Gal},z_{\rm f})$ of stars forming within a metallicity bin of size $\Delta\log Z$ is the integral of $\mathcal{N}(\mu{=}\ 12 + \log_{10}(O/H),\ \sigma{=}\ 0.3)$ over the metallicity bins of Z.

Taking an example MZR of KK04_Ma16, Figure 2.4 shows the fraction of stars for different metallicities as a function of $M_{\rm Gal}(z_{\rm f}{=}0)$ and $z_{\rm f}$. I show that different metallicities dominate in different redshift and galaxy mass ranges. Low-metallicity stars tend to form in low-mass galaxies ($M_{\rm Gal} \lesssim 10^9$ $M_\odot$) at high redshifts ($z_{\rm f} \gtrsim 3$). Conversely, high metallicity stars tend to arise in larger galaxies ($M_{\rm Gal} \lesssim 10^{10}$ $M_\odot$) at all redshifts. Stars with intermediate metallicities ($Z \simeq 0.1$ $Z_\odot$) can form in low-mass galaxies at low redshift and high-mass galaxies at high redshift.

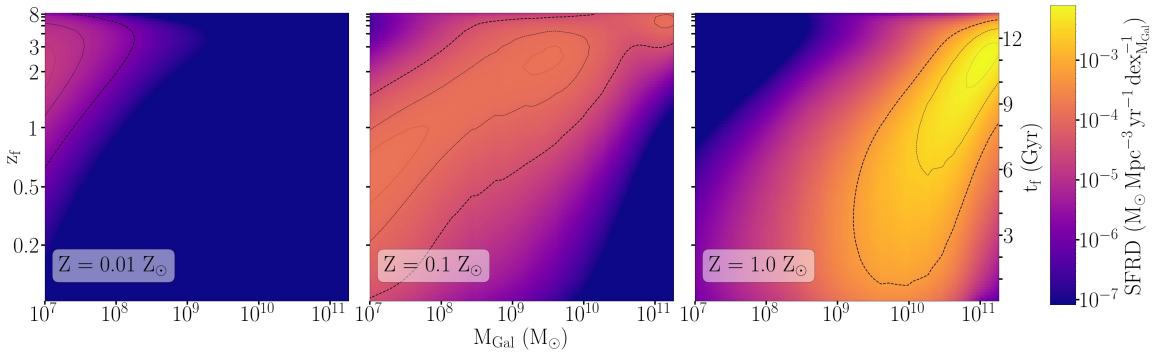

Figure 2.5: Star formation history for different metallicities in my default model. Star formation rate density (SFRD), shown in the color map, as a function of present-day galaxy mass $M_{\rm Gal}$ and formation redshift $z_{\rm f}$ or look-back time $t_{\rm f}$ for metallicities $0.01\,{\rm Z}_\odot$ (left), $0.1\,{\rm Z}_\odot$ (center) and $1.0\,{\rm Z}_\odot$ (right). The contour lines, in decreasing order of line width, contain the $90^{\rm th}$, $50^{\rm th}$ and $10^{\rm th}$ percentile of the SFRD. This particular SFRD is generated using the mass-metallicity relation from the Ma et al. [2016] fit for the Kobulnicky and Kewley [2004] calibration (KK04_Ma16).

2.1.3 Constructing the SFR

I construct the SFRD $\frac{{\rm d}^4 M_*}{{\rm d}V_{\rm c}\,{\rm d}t_{\rm f}\,{\rm dlog}M_{\rm Gal}\,{\rm dlog}Z}$ as a function of $M_{\rm Gal}$, Z, $z_{\rm f}$ by incorporating the star formation history of halos, the galaxy mass to dark-matter halo mass abundance matching, the galaxy stellar mass function, and the metallicity dependence of star formation

$$\begin{aligned}\frac{{\rm d}^4 M_*(Z, M_{\rm Gal}, z_{\rm f})}{{\rm d}V_{\rm c}\,{\rm d}t_{\rm f}\,{\rm dlog}M_{\rm Gal}\,{\rm dlog}Z} &= \frac{{\rm d}M_*(M_{\rm Gal}, z_{\rm f})}{{\rm d}t_{\rm f}} \times \frac{{\rm d}^2 N_{\rm Gal}(M_{\rm Gal}, z_{\rm f})}{{\rm dlog}M_{\rm Gal}\,{\rm d}V_{\rm c}} \\ &\times \frac{{\rm d}\Psi(Z, M_{\rm Gal}, z_{\rm f})}{{\rm dlog}Z},\end{aligned} \tag{2.1}$$

where $\frac{{\rm d}M_*(M_{\rm Gal}, z_{\rm f})}{{\rm d}t_{\rm f}}$ is the star formation history as a function of $M_{\rm Gal}$ and $z_{\rm f}$. Following the limits on $M_{\rm Gal}$ and $z_{\rm f}$ from Behroozi et al. [2013], I span the ranges $10^7 - 10^{11.25}\,{\rm M}_\odot$ and $0 - 8$ respectively. The range of metallicity covered by the COSMIC BPS code is from 10^{-4} to 1.78×10^{-2}. I use these ranges for my global model of merging black holes. Upon checking for robustness to different bin-sizes (further elaborated in § 2.1.4), the galaxy mass is logarithmically spaced with 200 samples, the redshift of formation is distributed uniformly in look-back time in intervals of 100 Myr. The number of metallicity bins is limited by the computational cost of running BPS simulations and will be defined in § 2.2.

I show the SFRD as a function of $M_{\rm Gal}$, and $z_{\rm f}$ in Figure 2.5 for the KK04_Ma16 model. Globally, the peak of star formation occurs at $z_{\rm f} \simeq 2.5$, in galaxies larger than the Milky-Way ($M_{\rm Gal} \simeq 10^{11}\,{\rm M}_\odot$) at nearly solar metallicity. Very low metallicity stars ($Z \simeq 0.01\,{\rm Z}_\odot$) are

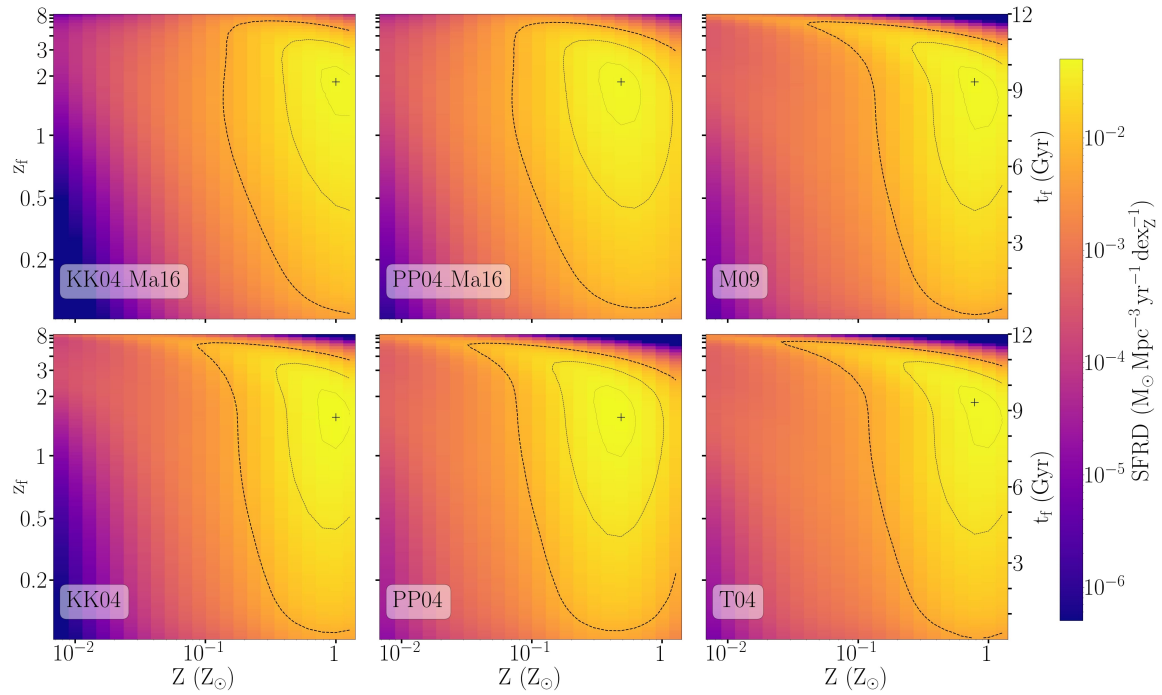

Figure 2.6: Star formation history as a function of metallicity for the different mass-metallicity models that I study. Clock-wise from the top-left, I show the star formation rate density based on different mass-metallicity relations: Ma et al. [2016] fit for Kobulnicky and Kewley [2004] (KK04_Ma16), Ma et al. [2016] fit for Pettini and Pagel [2004] (PP04_Ma16), Chruslinska and Nelemans [2019] fit based on Mannucci et al. [2009] refinement of Maiolino et al. [2008] (M09), Chruslinska and Nelemans [2019] fit for Tremonti et al. [2004] (T04), Chruslinska and Nelemans [2019] fit for Pettini and Pagel [2004] (PP04) and Chruslinska and Nelemans [2019] fit for Kobulnicky and Kewley [2004] (KK04). The contour lines in decreasing order of line width, contain the 90$^{\text{th}}$, 50$^{\text{th}}$ and 10$^{\text{th}}$ percentile of the SFRD, with the peak shown by '+'.

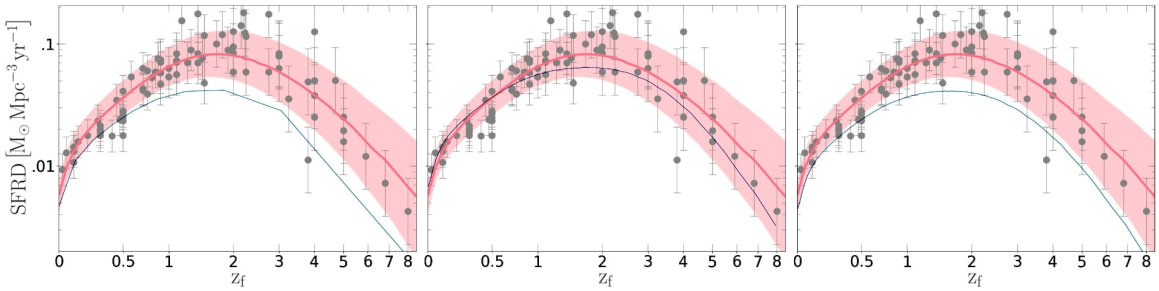

Figure 2.7: Comparing the star formation rate density of the Universe as function of redshift (from Figure 3 of Behroozi et al. [2013]) based on the data from Madau and Dickinson [2014] with my model for different bin sizes: coarse binning in $z_{\rm f}$ (left), coarse binning in $M_{\rm Gal}$ (center), converged distribution (right). The blue line represents the SFRD from my model. The black dots with error bars are observations and the red line and shaded region correspond to the best fit and the 1 sigma confidence region of the SFRD.

few in number and tend to form in dwarf galaxies ($M_{\rm Gal} \lesssim 10^9\,{\rm M}_\odot$) at high redshifts ($2 < z_{\rm f} < 4$). In contrast, high metallicity ($Z \simeq {\rm Z}_\odot$) stars are more numerous and are predominantly formed in large galaxies ($M_{\rm Gal} \gtrsim 10^{10}\,{\rm M}_\odot$) over a wide range of redshifts. Stars with metallicity $Z \simeq 0.1\,{\rm Z}_\odot$ can form in all types of galaxies. They are formed in dwarf galaxies at low redshift ($z_{\rm f} < 1$), average sized galaxies (10^9 to 10^{10} ${\rm M}_\odot$) at high redshifts ($2 < z_{\rm f} < 4$), and large galaxies at very high redshifts ($z_{\rm f} > 4$).

Figure 2.6 shows the SFRD as a function of Z, and $z_{\rm f}$ for the six different SFR/MZR models. The distributions show different peak values in terms of metallicity. The KK04 calibration has the highest mode of metallicity ($Z \simeq {\rm Z}_\odot$), followed by the mode of the M09 and T04 calibrations. The PP04 calibration shows the lowest mode of metallicity ($Z \simeq 0.5$). Comparing the 90% contours of the SFRD in different extrapolated fits of the MZR at high redshift ($z_{\rm f} \gtrsim 3$), the Ma_16 fits (corresponding to SFR/MZR of KK04_Ma16 and PP04_Ma16) show that most stars are formed with $Z \gtrsim 0.1\,{\rm Z}_\odot$. In contrast, fits which consider a smooth drop in the MZR with redshift (corresponding to SFR/MZR of KK04, PP04, T04 and M09) predict that, for $z_f > 3$, most stars are formed with $Z \lesssim 0.1$ ${\rm Z}_\odot$.

As I am interested in binary systems and their rate of formation, I include the fraction of binaries among stellar systems, ie., the binary fraction, into the SFRD. Based on observations of massive stars [Sana et al., 2012], it is set to a constant value of 0.7.

2.1.4 Testing the SFR

I compare my SFRD with observational data, specifically, the observed SFR as function of redshift [Madau and Dickinson, 2014]. I integrate the SFRD along the $M_{\rm Gal}$ and Z axes to produce the SFRD shown in Figure 2.7. In comparison to the finely binned case, coarse

binning of the time of formation (or equivalently z_f) brings the SFRD to lower values and coarse binning of the M_{Gal} artificially brings the rates to higher values. Although only 2 scenarios of large bin sizes is shown here, progressively coarse binning further amplifies this effect. The size of the bins for the converged SFR relation corresponds to 0.02 dex in galaxy mass, 1 Myr in the time of formation. As the SFRD is integrated over the metallicity, all bin sizes of metallicity and different SFR/MZR models produce the same relation. The bin size in metallicity is therefore determined by the computational demand of the binary evolution codes (§ 2.2). The SFRD from my model is relatively consistent with observations at low redshifts. At higher redshifts ($z_f \gtrsim 0.5$), deviation can arise due to improper modeling of the metallicity dependence of the SFR as elaborated in studies like Neijssel et al. [2019], Langer and Norman [2006].

2.1.5 Programming optimizations

A key improvement I introduce into my adaptation of the program used to produce the SFR in Lamberts et al. [2016] is a vastly more time efficient algorithm by 5 to 6 orders of magnitude. The current version of my code can produce the SFRD within a second. The same, run using the original Lamberts et al. [2016] code would take well over the duration of my PhD to compute. This was possible using an algorithm that uses existing optimized functions in built-in python libraries (numpy, scipy), hashing complicated and time-consuming integration (eg. cosmology-based conversion between time and redshift) into simpler fits, and using a few basic dynamic programming and pre-computation techniques that employ the use of stored data. The improvement in the computational complexity allows me to probe 2 orders of magnitude of finer binning along the three axes of the SFR for a fraction of the running time. As discussed in Figure 2.7, fine bin sizes along both the z_f and M_{Gal} axes is essential to produce a converging rate distribution.

2.2 Binary population synthesis

In order to understand the galactic environments that produce mBBHs, I simulate different models of the SFR (§ 2.1) and binary evolution to produce an astrophysical population of mBBHs which can then be used to map back to its progenitor properties. To produce a catalog of mBBHs for a given model of binary evolution, I use COSMIC [Breivik et al., 2020] to semi-analytically evolve binary star systems. From the catalog of mergers produced for different metallicities, I identify a representative sub-population of binary star systems with varying metallicities Z and binary parameters θ_{BPS} that ultimately form merging binary black holes (mBBHs), denoted by $Pop_{BPS}(Z, \theta_{BPS})$. I space the metallicities given in § 2.1 in 22 log-spaced bins, optimized for computational efficiency and checking for convergence in the Pop_{BPS} population to different binning.

For every metallicity, Z, I use COSMIC to iteratively sample and evolve binary zero-age main sequence (ZAMS) stars, selecting those that form mBBHs until recovering a converging distribution of BBH stellar-masses and orbital parameters at the time of formation with a tolerance mismatch of at most 10^{-4}. The primary star mass is sampled from the initial mass function in Kroupa [2001] between 15 and 100 $M_\odot$and the secondary mass is sampled from a uniform mass distribution from 15 $M_\odot$ to primary mass. The binary fraction is already incorporated into the SFR and is not used in the COSMIC simulations. The orbital parameters are sampled from Sana et al. [2012]. For each BPS model, across all metallicities, I evolve 1.2×10^{11} $M_\odot$ binary ZAMS star masses, forming a converging population of 2.2×10^6 progenitors of mBBHs. Due to the large number of binary simulations required for this analysis, I cannot use numerical simulations such as the MESA code. For example, García et al. [2021] uses MESA to perform a targeted simulation of $\sim$ 66,000 stellar binaries. In comparison, my simulations span a wider range of initial conditions for 40 binary evolution models, requiring 10^9 binary simulations.

The synthetic catalogs of binary stars allow me to compute the efficiency of forming mBBHs from binary stars, defined as the number of mBBH progenitors per unit mass of initial binary stars.

$$\eta_{\rm mBBH}(Z) = \frac{n_{\rm BPS}(Z)}{M_{\rm BPS}(Z)}, \tag{2.2}$$

where $M_{\rm BPS}$ is the total initial stellar-mass sampled to produce $Pop_{\rm BPS}$ and $n_{\rm BPS}$ is the number of mergers.

2.2.1 Establishing parameters explored

In this study, the default values of the binary evolution models (or COSMIC flags) have been set to values prescribed by the COSMIC documentation, v3.4.0 [1]. In the following paragraphs, I describe relevant flags and the values I explore. When exploring different values of a given parameter, all other parameters are set to their default values, thus varying only one parameter at a time. Note that I am not interested in commenting on the validity of the parameter values. Instead, I include variations in the BPS modeling to infer and compare the progenitor environments they predict. I emphasize that the motivation behind this agnostic approach is to focus on understanding how the inference of host galaxies depends on uncertainties in modeling binary evolution. In total, I simulate 40 different binary evolution models. Of these models, one is the default prescription and the remaining 39 have a different value of one of the flags. I summarize the values and corresponding BPS model of the parameters I explore in the following paragraphs and explicitly show in Table A.1 of the Appendix (§ A).

[1] https://github.com/COSMIC-PopSynth/COSMIC/tree/v3.4.0

The wind parameters I explore include the wind velocity factor ($\beta_{\rm w}$) and the mass loss near the Eddington limit ($\dot{M}L_{\rm edd}$). $\beta_{\rm w}$ is set to the Belczynski et al. [2008] prescription by default and I explore high (7) and low (0.125) values for Eq. (9) of Hurley et al. [2002]. The $\dot{M}L_{\rm edd}$ flag is set to be independent of the metallicity by default and I explore the metallicity dependence from Giacobbo et al. [2018].

I set the CE efficiency α by default to 1, and explore the values 0.1, 0.2, 0.3, 0.5, 2, 3, 5, 10. Efficiency greater than 1 violates the conservation of energy such that it is not possible for the envelope to be ejected due to the change in orbital energy alone. However, setting $\alpha > 1$ accounts for other potential energy sources (like ionization energy, and jets) to help eject the envelope. Sources of external energy include nuclear energy from burning at the center of the envelope or from burning at the accretor surface. The longer the CE phase lasts, the greater the likelihood that there is a deviation from the energy equation described in Eq. 1.2 [Ivanova et al., 2013]. Focusing on an agnostic approach toward model selection, and in order to understand the effect of the efficiency parameter at relatively unexplored values, I explore high values of α (> 3) that fall beyond the range that is typically considered possible. My default value for the binding energy factor of the envelope λ is set to the prescription from the appendix of Claeys et al. [2014], without the extra ionization energy. I also explore a case with the extra ionization energy as well as a constant λ set to $1/\alpha$ (see § 2.7.1 of Hurley et al. [2002]). I also check a CE prescription that prevents the direct stellar merger of systems lacking a core-envelope boundary of the donor ($CE_{\rm Merger}(0)$). Regarding the initial orbital energy calculation ($E_{\rm orb,i}$), I use, by default, the core masses as per Eq. (70) of Hurley et al. [2002] (here, Eq. (1.4)) and I explore the calculation with core + envelope mass from the de Kool [1990] prescription (here, Eq. (1.3)). The critical mass ratio model ($q_{\rm crit}$) determining the onset of CE is given by Table 2 of Claeys et al. [2014] and I explore alternate models from Hurley et al. [2002], Belczynski et al. [2008], and Hjellming and Webbink [1987] for GB/AGB stars.

In my default model, I use the natal kick prescription $v_{\rm Kick}$ of Hurley et al. [2002] where kicks are drawn from a Maxwellian distribution with dispersion parameter, σ, set to 265 km/s. I also simulate large (530 km/s) and small (90 km/s) values of σ. I explore other kick models described by two equations from Giacobbo and Mapelli [2020], and a relation for neutron star kick velocity from Bray and Eldridge [2016]. Eq 1 of Giacobbo and Mapelli [2020] scales the sampled kick velocity by the relative ratio of the ejecta mass by the remnant mass with respect to that of the typical neutron star and ejecta masses. Eq 2 scales the velocity by the ratio of the ejected mass with the typical ejecta mass for neutron star formation. Bray and Eldridge [2016] describes the kick as a linear function of the ratio of the ejected mass to remnant mass. Upon sampling the natal kick using $v_{\rm Kick}$ and σ, it is modulated for BHs by the $v_{\rm BH}$ flag. By default, the Fryer et al. [2012] prescription accounts for ejecta fallback. I also explore a model that re-weights the natal kick by the ratio of the remnant black hole mass to that of- a typical neutron star (1.44 $M_\odot$), and a model that does not alter the sampled natal kick.

The prescription of the supernova can influence the mass of the remnant drastically, denoted by the $M_{\rm NS-BH}$ flag. I set my default supernova mechanism to the rapid prescription of Fryer et al. [2012] with the proto-core mass from Giacobbo and Mapelli [2020] which results in a mass-gap between neutron stars and black holes. I also explore Belczynski et al. [2008], and the delayed prescription from Fryer et al. [2012], both of which fill the mass-gap. The pair-instability supernova (PISN) and the pulsational pair-instability supernova (PPISN) mechanisms are modeled by the $PISN$ flags. The default flag uses the Marchant et al. [2019] prescription which sets an upper limit on the component black hole mass of 45 $M_\odot$ and I explore the models of Spera and Mapelli [2017] and Woosley [2019]. In addition, I also switch off the PISN and PPISN mechanisms. Finally, I also explore the effect of different tide modeling, $Tide_{\rm ST}$, using Belczynski et al. [2008] for the default and exploring Hurley et al. [2002].

2.2.2 Coding binary population simulations

The SFRD from § 2.1 can be produced with an extremely fine grid in metallicity within a second of runtime due to analytic model described. The BPS simulations, however, require a semi-analytical approach to produce a converging population of mBBH from progenitors of a given metallicity that requires a long runtime ($\simeq$ 10-100 hrs using 20 CPU cores, depending on the metallicity and evolution model). Hence, I limit the number of metallicity bins to 22 to efficiently explore the 40 BPS models.

Figure 2.8 shows a flowchart describing the structure of my program. I use batch scripts to execute commands on the Slurm Workload Manager to parallelize my workflow. I used the computational resources of my university cluster, Licallo, which provided over 250 nodes with 40 cores in each node for parallel computation. The "controller" batch script initializes 40 "agents" scripts that parallelly and independently simulates 40 BPS models. Each agent simultaneously executes 22 COSMIC runs for every metallicity bin. Instructions to COSMIC regarding the metallicity of the progenitors and the flags of the BPS model is specified within 22 configuration files generated by the agents. The agents supervise the COSMIC runs, logging down any outputs or errors which I can use to monitor the progress and to potentially troubleshoot problems. Once COSMIC successfully produces a converging population of mBBHs for each of the metallicities, the agents assimilates the population into a large database $Pop_{\rm BPS}$ that is unique to every BPS model. The agents then terminate and the control is passed back to the controller. The controller catalogues the progress and errors of the agents in its log file.

In the interest of efficiency and due to the limited allocation of resources per user of the cluster, the large number of BPS models were simulated in a joint effort by a fellow PhD student, and good friend, Tristan Bruel and myself. We parallelly ran simulations of 20 models each. In order to optimize the performance of the program, I maximize the use of the allocated memory, and RAM (nodes and cores) of the cluster. The controller

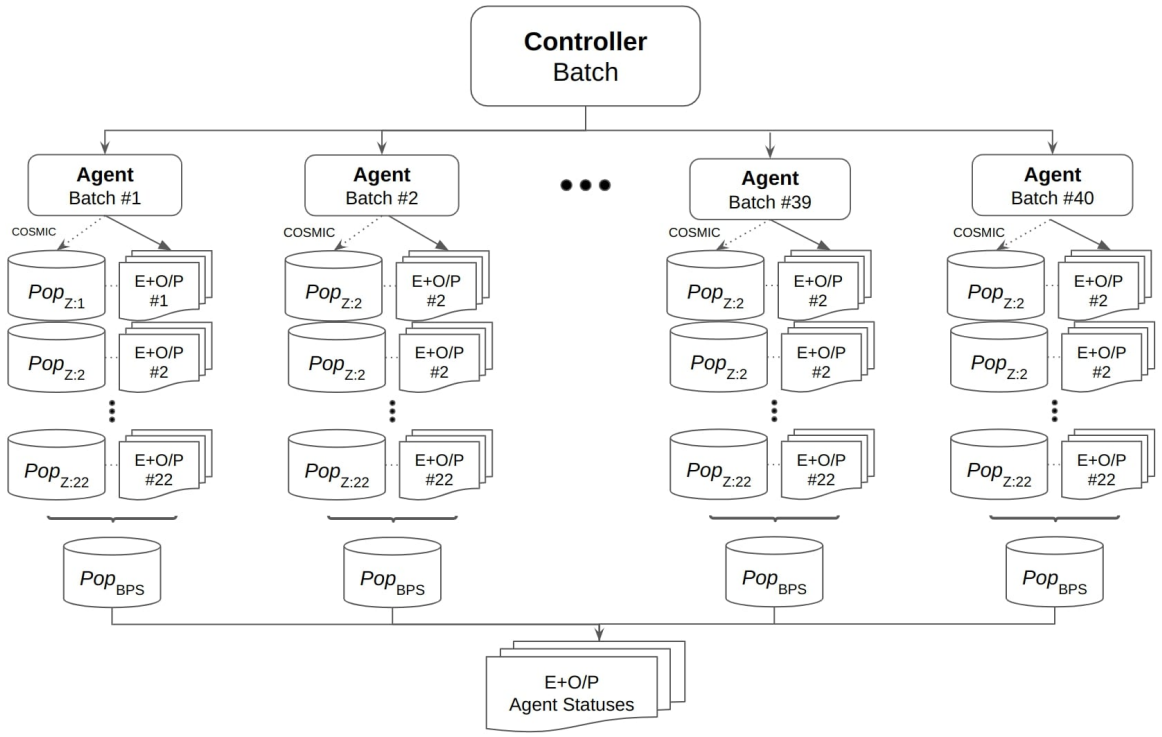

Figure 2.8: Flowchart describing the architecture of my code to run a host of BPS simulations to produce 40 different populations of mBBHs ($Pop_{\rm BPS}$), one for each BPS model. This program was executed using batch scripts (1 "controller" and 40 "agents") that utilize the Slurm Workload Manager on a local cluster with a Linux-like kernel. For a given BPS model, $Pop_{\rm BPS}$ is produced by combining the separately produced populations of 22 BPS simulations $Pop_{\rm Z:i}$, one for each metallicity Z, indexed by i. The executions of COSMIC codes are represented by the dotted arrows. E+O/P refers to the error and outputs log files.

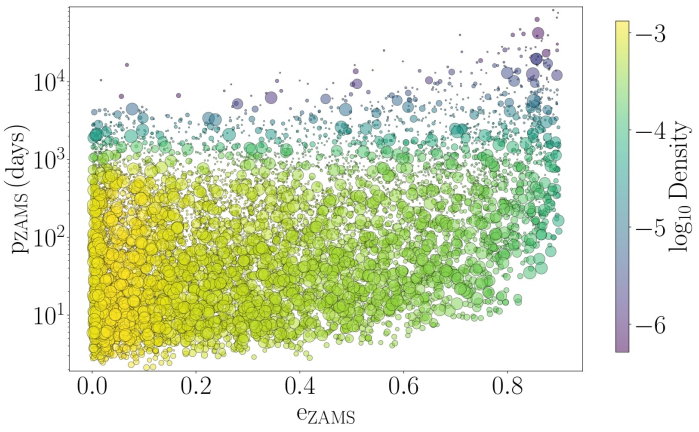

Figure 2.9: Initial orbital period p_{ZAMS} and initial eccentricity e_{ZAMS} of binary systems that form mBBHs using the default binary evolution model. The relative size of the circle is indicative of the total mass of the mBBH, and the colorbar represents the relative formation rate.

distributes a node to every agent and the agents allocate 10-20 cores of the node for each of the 22 COSMIC runs. COSMIC efficiently uses the CPUs of the cores to parallelly evolve the multitude of binary systems. Typically, for every BPS model, the population for low metallicities progenitors take 1-2 days to compute, while the higher metallicities can take 1-2 weeks. This is due to the low efficiency of forming mBBHs in high metallicity systems. In the ideal scenario of 100% available computational resources in the local cluster, the entire simulation of 40 BPS models would simultaneously complete within 2 weeks. However, due to the variable percentage of resources shared between users of the clusters, the complete simulation took nearly 2 months to execute. Keeping in mind the layers of parallelization used to rapidly produce the results (40 BPS $\times$ 22 metallicities), the use of the cluster and the Slurm scheduling algorithm was a vital step in ensuring the timely completion of the simulations.

2.2.3 Understanding binary evolution

To understand the correlations of binary parameters and their influence on the mBBH population, I illustrate the properties of a Pop_{BPS} produced using the default model of COSMIC (unless specified otherwise).

Effect of initial orbital parameters

Figure 2.9 shows the orbital period p_{ZAMS} versus the eccentricity e_{ZAMS} of the initial ZAMS stars. Systems with low orbital period ($p_{\mathrm{ZAMS}} \in 10-200$ days) and low eccentricity

($e_{\rm ZAMS} \in 0-0.1$) tend to form mBBHs. The low $p_{\rm ZAMS}$ corresponds to low initial separation between the stars which encourages mass-transfer due to the small Roche lobe of the stars. Depending on the relative mass of the donor and accretor, this process can crucially bring the bodies closer together. Moreover, in the case of an unstable mass transfer and the formation of a CE, the orbital energy lost towards ejecting the envelope can drastically shorten the orbit and hence increase the chances of merging within the present-day. Note that Figure 2.9 only represents systems which merge as black holes, and ignore those that undergo stellar mergers. The dearth in the formation of mBBH from systems with low $p_{\rm ZAMS}$ and high $e_{\rm ZAMS}$ is due to the increased probability of stellar mergers as a result of the close proximity of the stars. Moreover, maximally eccentric systems can undergo disruptions that break the binary. Systems with high $p_{\rm ZAMS}$ and low $e_{\rm ZAMS}$ also do not form mBBH due to the large separation between the stars, thereby increasing the delay time, and preventing the system from merging by the present-day. In comparison, systems with high $p_{\rm ZAMS}$ and high $e_{\rm ZAMS}$ are likely to form mBBHs due to the close proximity of interaction in highly eccentric systems. The black hole masses generally appear to be uniformly distributed across the parameters, with minor trends. For example, very low $p_{\rm ZAMS}$ systems tend to form small mBBHs. This is expected due to the increased probability of unstable mass-transfers which can lead to mass loss.

Effect of initial binary masses

Figure 2.10 shows the correlation between the initial mass ratio $q_{\rm ZAMS}$, initial total mass $M_{\rm Tot\,ZAMS}$ and the number of CE events. First, it is apparent that the vast majority of binaries that form mBBHs undergo one CE event. Moreover, as shown by the relative sizes of the circles, binaries which do not undergo CE generally form larger black holes than those which do as a result of the mass lost by the donor star in the latter case. Systems which do not undergo CE have stars that have unequal masses ($q_{\rm ZAMS} \gtrsim 1.5$) due to the critical mass ratio $q_{\rm crit}$ parameter that determines the onset of CE. Moreover, most systems do not undergo multiple CEs due to the increased chance of stellar mergers and large mass loss preventing black hole formation. Finally, the large density of systems with low initial total mass is due to the inverse power law of the initial mass function.

Influence of metallicity in mass loss

Figure 2.11 shows the effect of metallicity on the total black hole mass for a range of initial total mass. In high metallicity stars ($Z \gtrsim 0.5\,{\rm Z}_\odot$), large mass loss primarily due to enhanced winds leads to the formation of small final black holes as indicated by the small circles. Thus, high metallicity stars that form black holes tend to be massive. However, due to the power law nature of the initial mass function [Kroupa et al., 2013], these systems are few in number. Low-metallicity environment ($Z \lesssim 0.05\,{\rm Z}_\odot$) does not greatly influence the final

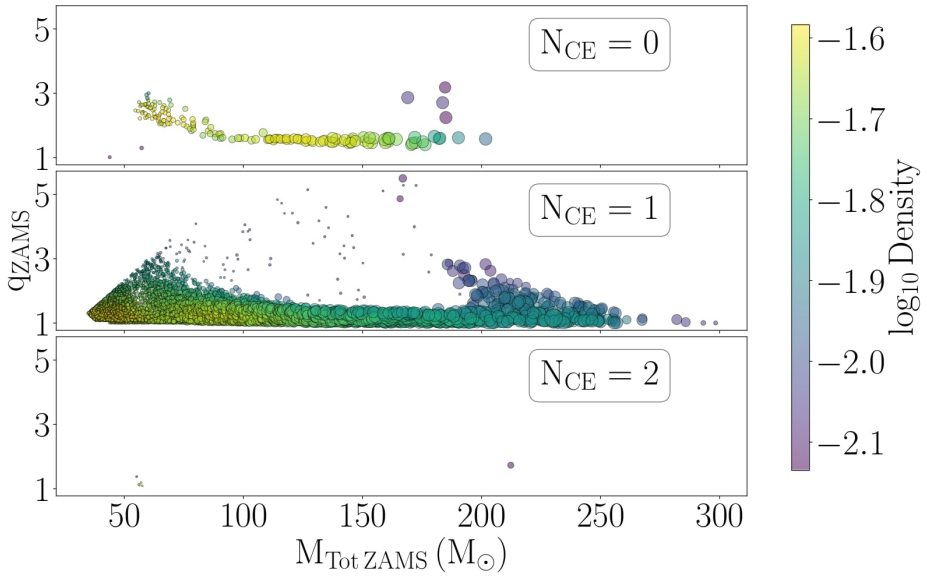

Figure 2.10: Initial mass ratio q_{ZAMS} versus total initial mass $M_{tot\,ZAMS}$ of binary systems that form mBBHs for different number of CE events N_{CE} using the default binary evolution model for all metallicities. The relative size of the circle is indicative of the total mass of the mBBH, and the colorbar represents the relative formation rate.

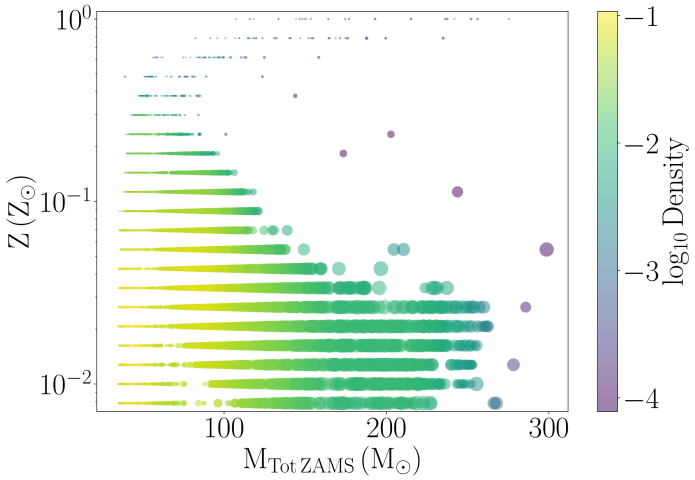

Figure 2.11: Metallicity Z versus total initial mass $M_{tot\,ZAMS}$ of binary systems that form mBBHs using the default binary evolution model. The relative size of the circle is indicative of the total mass of the mBBH, and the colorbar represents the relative formation rate.

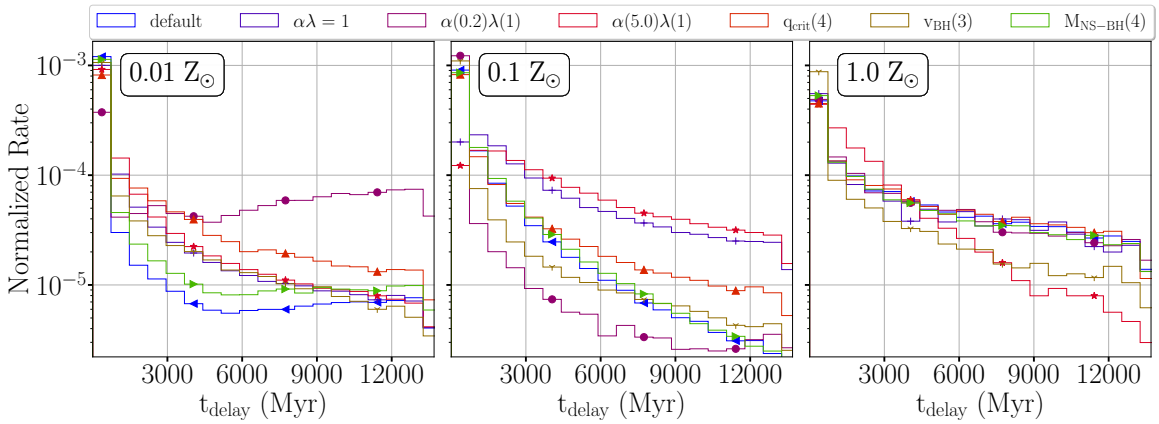

Figure 2.12: Normalized histogram of the delay time ($t_{\rm delay}$) of the mBBHs from the $Pop_{\rm BPS}$ of the binary population synthesis simulation for different BPS models (colors and symbols), across 3 metallicity bins: 0.01 $Z_\odot$ (left), 0.1 $Z_\odot$ (center), 1 $Z_\odot$ (right).

black hole mass. Instead, the final mass mostly depends on the initial total mass.

Delay time distribution

Figure 2.12 shows the delay time distribution of mBBHs for 3 metallicities for systems which merge within a Hubble time. The different colored lines represent different BPS simulations, shown for the comparison of trends. The vast majority of delay times in the BPS simulation are short, implying that the systems typically merge soon after the formation of the binary, ie., the redshift of merger $z_{\rm mBBH} \simeq z_{\rm f}$. Figure 2.12 also shows that large delay times are common for higher metallicity progenitors. As such, I expect high redshift progenitors of nearby systems to have $Z > 0.1\ Z_\odot$. Although typical delay time distributions follow a power-law relation of the form $t_{\rm delay}^{-\alpha}$, some binary models at low metallicity ($Z = 0.01\ Z_\odot$) flatten at high delay times (>6 Gyr). This is due to the abundance of massive black hole binaries in low metallicity environments. The massive black holes are likely to merge by the present day due to the greater loss in orbital energy to GW emission. Moreover, this effect is pronounced for the low CE efficiency model ($\alpha(0.2)\lambda(1)$) as the low metallicity, massive stars have larger orbital angular energy which can be used to eject the envelope.

2.3 Astrophysical and detectable mBBH population

A quick estimation of the astrophysical progenitor formation rate can be obtained by computing the product of the efficiency of forming mBBHs $\eta_{\rm mBBH}$ as a function of metallicity

Z, the fraction of systems from $Pop_{\rm BPS}$ which can merge by the present day when formed at a given redshift of formation $z_{\rm f}$, and the SFRD as a function of the galaxy properties ($M_{\rm Gal}$, Z, $z_{\rm f}$). However, in order to map a given set of mBBH properties (such as the masses, and luminosity distance to the merger) to the progenitor galaxy properties, it is useful to create an astrophysically representative population of mBBH systems $Pop_{\rm Astro}$ as a function of the three-dimensional galaxy properties.

2.3.1 Producing the astrophysical population

For every element in the 3D progenitor parameter space with a given metallicity Z, I randomly sample $N_{\rm s}$ systems with the same metallicity from the population of binary black holes produced by the simulation of binary evolution ($Pop_{\rm BPS}$) to produce an astrophysical population of merging binary black hole progenitors, $Pop_{\rm Astro}$. I discard systems that merge after the present day. Every sampled system is assigned an astrophysical progenitor formation rate $R_{\rm i}$ that is proportional to the SFRD and the efficiency of mBBH formation $\eta_{\rm mBBH}$

$$\begin{aligned} R_{\rm i}(Z, M_{\rm Gal}, z_{\rm f}) &= \frac{{\rm d}^2 N_{\rm i}(Z, M_{\rm Gal}, z_{\rm f})}{{\rm d}V_{\rm c}\,{\rm d}t} \\ &= \frac{{\rm d}^2 M_{*\,{\rm i}}(Z, M_{\rm Gal}, z_{\rm f})}{{\rm d}V_c\,{\rm d}t} \times \eta_{\rm mBBH}(Z) \times \frac{1}{N_{\rm s}}, \end{aligned} \tag{2.3}$$

where i denotes the $i^{\rm th}$ mBBH progenitor system in $Pop_{\rm Astro}$, ${\rm d}^2 N_{\rm i}$ is the number of such systems within the differential co-moving time-volume element ${\rm d}V_{\rm c}\,{\rm d}t$, and $\frac{{\rm d}^2 M_{*\,{\rm i}}}{{\rm d}V_{\rm c}{\rm d}t}$ is the SFRD from Eq 2.1 integrated over the width of the galaxy mass and metallicity bin. $R_{\rm i}$ is expressed in units of ${\rm Mpc}^{-3}{\rm yr}^{-1}$. I compute the 3D astrophysical rate of mBBH progenitor formation, R, by summing over all mBBH progenitor systems. In § 2.3.4, I elaborate on two methods of choosing $N_{\rm s}$: variable, and constant value. I also discuss the benefits and shortcomings of the resulting $Pop_{\rm Astro}$ distributions.

Astrophysical merger rate

The merger rate of systems that coalesce within a look-back time bin centered at $t_{\rm mBBH}$ can be directly mapped back to the corresponding progenitor formation rate within an identically sized time bin centered at $t_{\rm f}$ [Dominik et al., 2013], with $\Delta t = 100\,{\rm Myr}$. I obtain the merger rate evolution, $R_{\rm mBBH}(z_{\rm mBBH})$, by summing over the progenitor parameter space the product of the progenitor formation rate and the corresponding fraction of progenitors that merge within the time bin $t_{\rm mBBH}$.

2.3.2 Detectable mBBH population

To understand the detector selection effect on the progenitor population of mBBHs, I simulate GWs from the merger of every mBBH system in $Pop_{\rm Astro}$. I use the phenomenological inspiral-merger-ringdown waveform approximant IMRPhenomD [Khan et al., 2016], implemented in lalsuite [LIGO Scientific Collaboration, 2020], called from the python library PyCBC [Usman et al., 2016]. The masses and $z_{\rm mBBH}$ of the merging black holes are extracted from my astrophysical population $Pop_{\rm Astro}$. The luminosity distance is calculated from $z_{\rm mBBH}$ using a flat ΛCDM cosmology model described in § 1.1. I assume the black holes are non-spinning. I distribute the sky positions isotropically and I sample the cosine of the inclination angle from a uniform distribution.

I consider a GW detector network of LIGO Hanford (H), LIGO Livingston (L) and Virgo (V) with their sensitivity during the second half of the O3 observation run [Abbott et al., 2023]. Their power spectral density are shown in Figure 1.8. I designate an mBBH as detectable if the optimal signal-to-noise ratio (Eq 1.11) in each detector is larger than 6 and the network signal-to-noise ratio is larger than 12.

Simulating GWs and their detection, I calculate the detection rate density, R_{Det}, in units of $\rm yr^{-1} z^{-1}_{mBBH}$ using the relation

$$\begin{aligned} R_{Det}(z_{\rm mBBH}) &= \frac{{\rm d}N_{\rm Det}(z_{\rm mBBH})}{{\rm d}t_{Det}\,{\rm d}z_{\rm mBBH}} \\ &= R_{\rm mBBH}(z_{\rm mBBH}) \times \frac{{\rm d}t}{{\rm d}t_{\rm Det}} \times \frac{{\rm d}V_c}{{\rm d}z_{mBBH}} \times f_{\rm Det}(z_{\rm mBBH}) \times \eta_{\rm GW}, \end{aligned} \quad (2.4)$$

where $f_{\rm Det}(z_{\rm mBBH})$ is defined as the fraction of binaries in $Pop_{\rm Astro}$ merging at $z_{\rm mBBH}$ that are detectable by the three detectors. ${\rm d}t/{\rm d}t_{\rm Det} = (1+z_{\rm mBBH})^{-1}$ accounts for the redshift in the rate of time in the source-frame with respect to that in the detector-frame. $\eta_{\rm GW}$ is the duty cycle of the detector network and $\frac{{\rm dV_c}}{{\rm dz_{mbbh}}}$ is the co-moving volume per unit redshift as described by the cosmology. Finally, we calculate the detection rate of mBBH per year by integrating $R_{\rm Det}$ across all $z_{\rm mBBH}$.

$$\frac{{\rm d}N_{\rm Det}}{{\rm d}t_{\rm Det}} = \sum_{\forall\, z_{\rm mBBH}} R_{\rm Det} \times {\rm d}z_{\rm mBBH} \quad (2.5)$$

2.3.3 Progenitor galaxy posterior of a GW event

As a follow-up of my simulations, I infer the properties of the progenitor formation galaxy of detected mBBHs from real observational data of the LIGO-Virgo detectors. For this purpose, I download the posterior samples of confident detections from the catalog of the

Gravitational Wave Open Science Center website [2]. To produce the posterior probability distribution of $M_{\rm Gal}$, Z, and $z_{\rm f}$ for any detected GW event, I compute the probability of the progenitor formation rate $p_{\rm sim}$ as a function of the component black hole masses $M_{1,\rm BBH}$, $M_{2,\rm BBH}$ and luminosity distance $D_{\rm Lum}$, weighted by the corresponding detected posterior distribution of the GW event as shown below

$$p(M_{\rm Gal}, Z, z_{\rm f}|x_{\rm GW}) = \int p(M_{1,\rm BBH}, M_{2,\rm BBH}, D_{\rm Lum}|x_{\rm GW}) \times p_{\rm sim}(M_{\rm Gal}, Z, z_{\rm f}|M_{1,\rm BBH}, M_{2,\rm BBH}, D_{\rm Lum}) \times {\rm d}M_{1,\rm BBH}\,{\rm d}M_{2,\rm BBH}\,{\rm d}D_{\rm Lum}, \tag{2.6}$$

where $x_{\rm GW}$ represents the GW event, $M_{1\,\rm BBH}$ is the primary black hole mass, $M_{2\,\rm BBH}$ is the secondary mass, and $D_{\rm Lum}$ is the luminosity distance of the merger. This simple statistical method involves re-weighting the typical $M_{\rm Gal}$, Z, $z_{\rm f}$ values from the simulation by the most credible $M_{1\,\rm BBH}$, $M_{2\,\rm BBH}$, $D_{\rm Lum}$ values of detected GW events. In the hypothesis that a given detected GW is formed by the processes described by the simulation, $p(M_{\rm Gal}, Z, z_{\rm f}|x_{\rm GW})$ provides the most credible values for $M_{\rm Gal}$, Z, $z_{\rm f}$.

2.3.4 Generating $Pop_{\rm Astro}$

When implementing the discussed method of generating the astrophysical population of systems that form mBBHs, it is important to adequately represent the different kinds of systems, each identified by the multitude of properties (such as the metallicity, black hole masses, distance of merger, initial star properties, sequence of binary evolution, etc). This "resolution" of the astrophysical population, $Pop_{\rm Astro}$, is set by the choice of $N_{\rm s}$, the number of systems sampled for a given progenitor environment. In this section, I detail the generation of $Pop_{\rm Astro}$ using a variable and constant value of $N_{\rm s}$.

Variable sampling

In the variable sampling method I designed, for a given set of progenitor parameters (Z,$M_{\rm Gal}$,$z_{\rm f}$), $N_{\rm s}$ is proportional to the progenitor formation rate in order to ensure convergence of $Pop_{\rm Astro}$ towards the astrophysical population. $N_{\rm s}$ is described by

$$N_{\rm s} = \lfloor \frac{{\rm d}^2 M_{*\,\rm i}(Z, M_{\rm Gal}, z_{\rm f})}{{\rm d}V_c\,{\rm d}t} \times \eta_{\rm mBBH}(Z) \times \frac{1}{R_{\rm Thresh}} \rfloor, \tag{2.7}$$

where the function $\lfloor x \rfloor$ returns the greatest integer less than or equal to x. $R_{\rm Thresh}$ is a threshold rate that sets the lowest value of the progenitor formation rate $R_{\rm i}$. Elaborating

[2] https://gwosc.org/eventapi/html/GWTC/

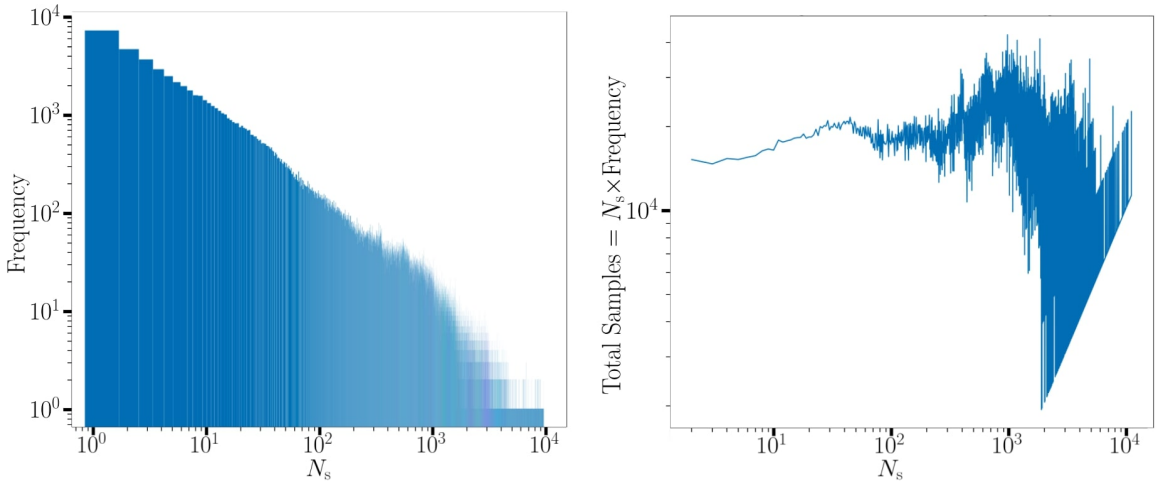

Figure 2.13: **Left** Histogram of the number of samples N_s extracted from Pop_{BPS} to generate Pop_{Astro} for every element of the 3-dimensional set of parameters Z, M_{Gal}, z_f. The number of samples for a given set of parameters in the cube is proportional to the progenitor formation rate corresponding to that element. **Right** Total number of systems for a given number of samples. Note that around 90% of progenitor systems have $N_s = 0$ and are not shown in this figure.

further, any progenitor for which the product of the SFR and the efficiency of forming mBBH is less than the threshold rate will not be represented in Pop_{Astro}, i.e., $N_s = 0$. However, as the threshold rate R_{Thresh} approaches the minimum value of the product of the SFR and efficiency, $N_s \gtrsim 1$ for an increasing fraction of progenitor parameters. This results in a large size of Pop_{Astro}.

Figure 2.13 summarizes the frequency and number of systems with a given N_s in Pop_{Astro}. The histogram on the left shows that most progenitor systems have low N_s ($\lesssim 10$), and very few have high values ($N_s \gtrsim 1000$). As a result, Figure 2.13, right, shows that the total number of systems sampled with a given N_s is approximately constant $\simeq 20,000$.

This technique of sampling emphasizes a greater representation of systems with larger formation rates, i.e., they are sampled more. However, it suffers from two flaws.

- **Large space complexity** The size of the file containing Pop_{Astro} rapidly increases as R_{Thresh} is set to lower values. As the formation rate of progenitors spans 6 to 8 orders of magnitude, and the number of samples N_s increases with the rate, I have to set R_{Thresh} to relatively high values (3-4 orders of magnitude below the maximum formation rate) to limit the file size of $Pop_{Astro} \lesssim 20$ GBs.

- **Under-representation of detectable mBBHs** As most progenitor parameters (Z,

$M_{\rm Gal}$, $z_{\rm f}$) have a low progenitor formation rate that falls below $R_{\rm Thresh}$, $Pop_{\rm Astro}$ misses out on their representation. Over 90% of the total progenitor formation rate across cosmic time is not sampled as a result. This is especially concerning as low metallicity, small galaxies ($Z \lesssim 0.05\ {\rm Z}_\odot$, $M_{\rm Gal} \lesssim\ 10^9\ {\rm M}_\odot$) have low formation rates. However, these galaxies contribute to the majority of detectable mBBHs (discussed in detail in Chapter 3).

As a result of these flaws, I discarded the variable sampling and developed the fixed sampling method instead.

Fixed sampling

To address the issue of large file sizes and under-sampling associated with the variable $N_{\rm s}$, I designed a fixed sampling method. This technique is superior due to its reduced space usage and better representation of systems with low formation rates. Setting $N_{\rm s}$ to a fixed value, every 3D progenitor element is sampled the same number of times from $Pop_{\rm BPS}$ to produce $Pop_{\rm Astro}$ (upon filtering out systems that do not merge by the present-day). Thus, irrespective of the formation rate, each system gets equal representation in the astrophysical population. Moreover, the size of the $Pop_{\rm Astro}$ file is proportional to $N_{\rm s}$ and thus remain constrained. The typical size of the $Pop_{\rm Astro}$ file is $\simeq 20$ GB for $N_{\rm s} = 100$.

Figure 2.14 illustrates the convergence of population properties with increasing $N_{\rm s}$. For $N_{\rm s} = 1$, there are visible under-sampling effects in the coarse histogram of the mass spectrum (top) and the black pixels of the progenitor formation rate (bottom) corresponding to progenitor parameters whose sampled systems did not merge by the present day. As the number of samples per progenitor element increases, the mass spectrum becomes smooth and converges to a final shape. Moreover, the formation rate also becomes smooth, with fewer black pixels indicating better sampling. In contrast, the present-day merger rate does not show a large variation with the number of samples (R_0, in ${\rm Gpc}^{-3}\ {\rm yr}^{-1}$, of 385 for $N_{\rm s} = 1$, 385 for $N_{\rm s} = 10$, and 391 for $N_{\rm s} = 100$).

As a good compromise between population robustness, computational efficiency, and memory management I set $N_{\rm s} = 100$ for analysis that requires population properties such as the BH mass spectrum and trends in the progenitor formation rate. However, to save time and space, I set $N_{\rm s} = 1$ when I'm only interested in calculating the present-day merger rate. This creates the $Pop_{\rm Astro}$ 100 times faster, and 50 times smaller in size than that of $N_{\rm s} = 100$.

2.3.5 Constructing a pipeline to visualize data

Iterating over the discussed 6 models of the SFR/MZR and 40 models of the BPS evolution, I generate 240 realizations of $Pop_{\rm Astro}$. To understand the progenitor formation rates for the

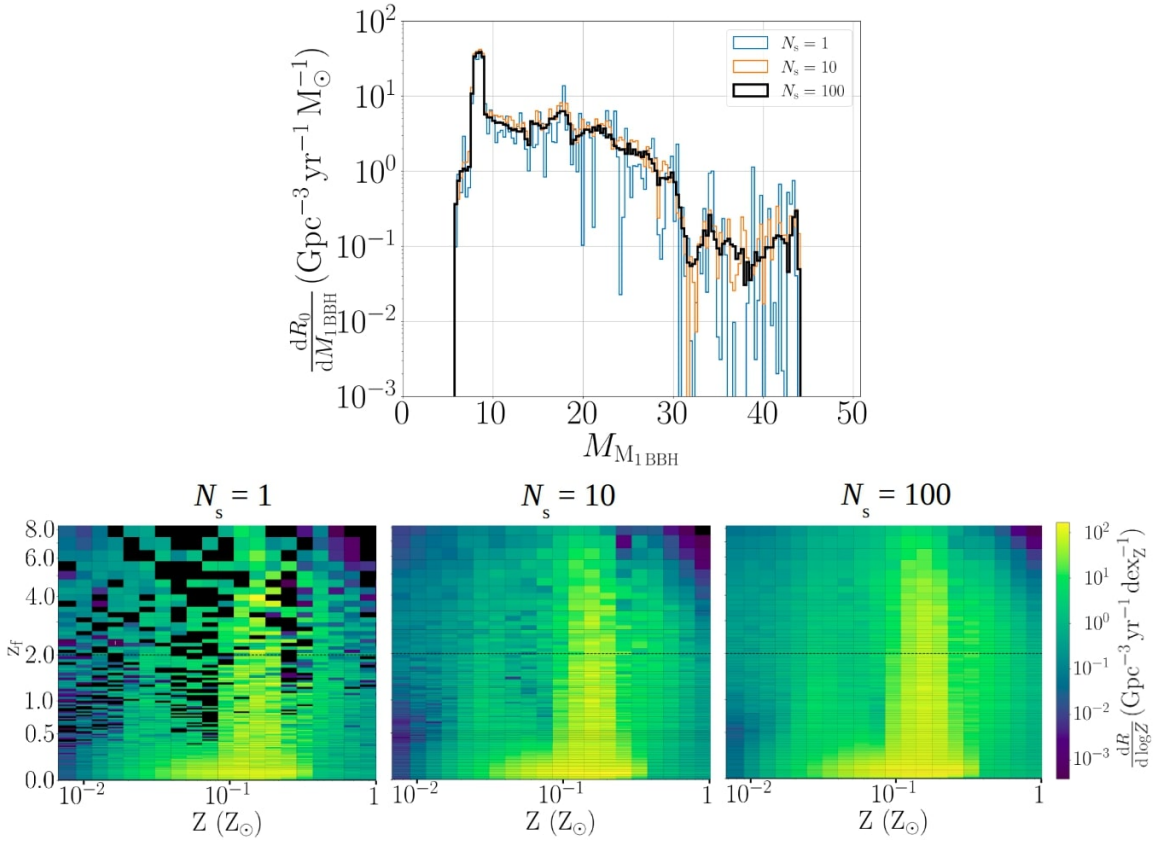

Figure 2.14: **Top** Mass spectrum of the primary black hole and **bottom** progenitor formation rate as a function of Z and z_f for different values of N_s. The black pixels in the bottom plots represent regions that do not have sampled systems that merge.

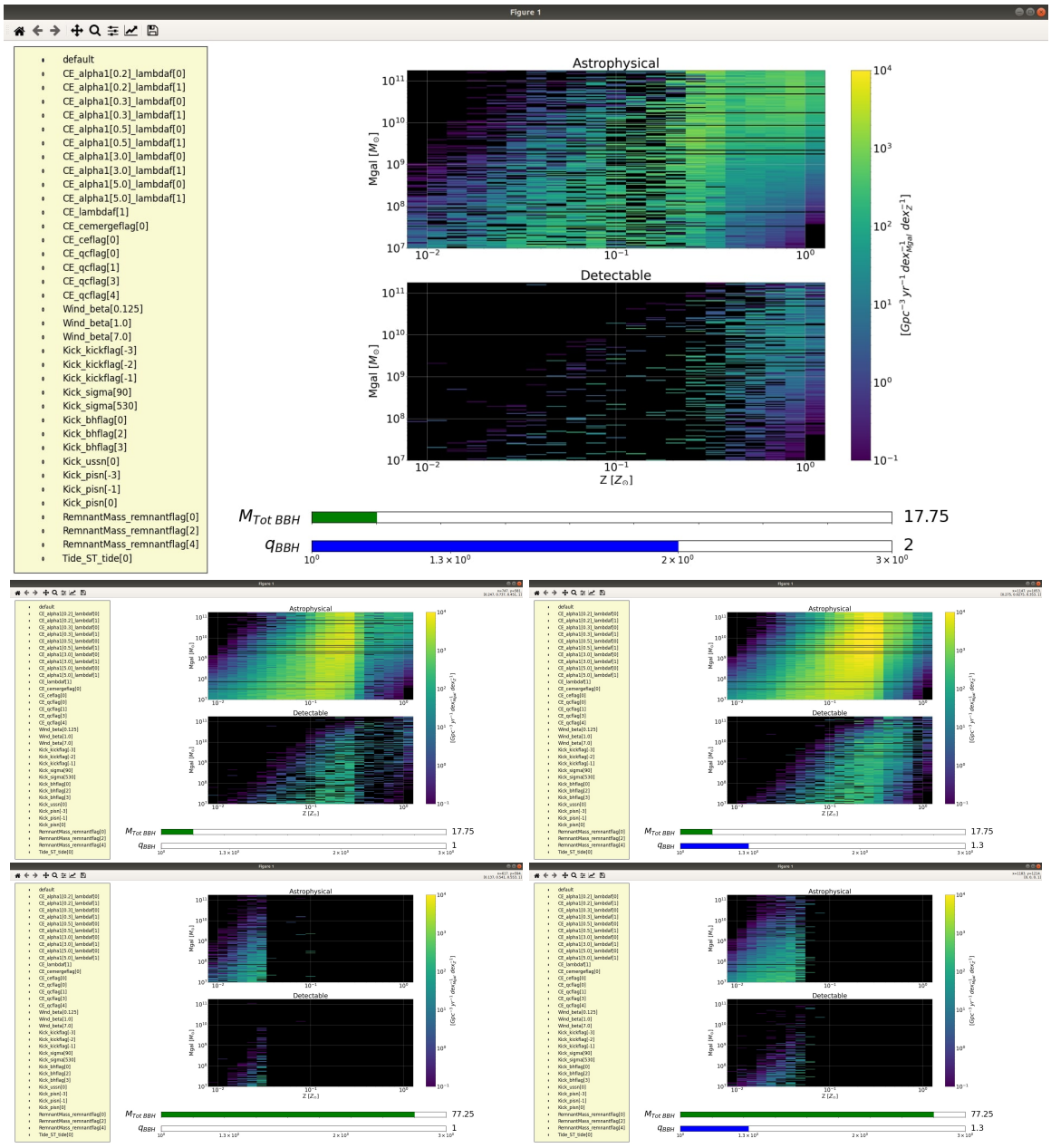

Figure 2.15: Screenshots illustrating the graphical user interface I designed to display the progenitor formation rates of mBBH with user-specified values of the BPS model, total black hole mass $M_{\mathrm{Tot\,BBH}}$, and mass ratio q_{BBH}. The BPS model is selected using radio buttons on the left column in yellow, while the mBBH properties are selected using a slider. Regions of black in the formation rate indicate an absence of systems in the Pop_{Astro} of the BPS model which merge by the present-day and which satisfy the selected mBBH properties. The SFR/MZR model and the axes of the formation rate were specified by the user-input keystrokes when starting the program.

host of models, I require an efficient and convenient tool to visualize patterns and overlapping trends. In addition to the 240 models, I am interested in seeing changes in the progenitor formation rate for different mBBH properties like the primary mass and mass ratio of the black holes, and the luminosity distance of the merger. In order to visualize a 3 dimensional (Z, $M_{\rm Gal}$, $z_{\rm f}$) progenitor formation rate with 3-4 degrees of freedom (SFR/MZR+BPS model, and 2-3 mBBH properties like $M_{\rm 1\,BBH}$, $q_{\rm BBH}$, etc), I design a graphical user interface (GUI) program that provides interactive options for the user to probe the vast data.

Using the matplotlib python library along with its derivatives, I construct the GUI to display the progenitor formation rates of the astrophysical and detectable mBBHs along the user-specified axes of progenitor properties. The controls include radio buttons for the different SFR/MZR and BPS models along with slider bars to select the mBBH total mass $M_{\rm Tot\,BBH}$ and mass ratio $q_{\rm BBH}$. Figure 2.15 shows snapshots of the GUI. Shown here is an example for the user-specified KK04_Ma16 SFR/MZR model and along the Z, $M_{\rm Gal}$ axes. Black regions in the plot indicate failure to identify systems in the selected BPS model that merge by the present day and which satisfy the selected bins of $M_{\rm Tot\,BBH}$ and $q_{\rm BBH}$.

Showcasing the ease of extracting information using this GUI, I show the trends in the progenitor properties for increasing $M_{\rm Tot\,BBH}$ and $q_{\rm BBH}$ in the sub figures of Figure 2.15. As as example, I show that black holes with large $M_{\rm Tot\,BBH}$ can arise from small galaxies with low metallicity. I also show that equal mass mBBHs ($q_{\rm BBH} \simeq 1$) have lower rates than slightly unequal mBBHs ($q_{\rm BBH} \simeq 1.3$).

2.3.6 Quantifying the overlap

One cannot exclusively rely on visual tools to analyze data, especially when there are many degrees of freedom with large correlations between parameters. It can be overwhelming to keep track of the changes seen by eye. Therefore, in order to quantify common trends between different SFR/MZR and BPS models, I designed an overlap metric. Simplifying the visual process, the overlap quantifies the degree of overlapping trends in the progenitor formation rate for different models. To do so, I first define an "area" about which I can calculate the overlap. This "area" is a surface in a projected 2D parameter space, say Z versus $M_{\rm Gal}$, which contains the top 50 percentile of the progenitor formation rate. Essentially, it is the area enclosed by a 50-percentile contour of the progenitor formation rate as a function of Z, $M_{\rm Gal}$. The overlap, O, for a given set of models is defined as

$$O = \frac{A \cap B \cap C \cap D...}{A \cup B \cup C \cup D...}, \tag{2.8}$$

where A, B, C, D, etc are 50 percentile areas of the progenitor formation rate along Z, $M_{\rm Gal}$ for different SFR/MZR + BPS models. $\cap$ is the intersection and $\cup$ is the union of sets. The same exercise can be applied to calculating the overlap for a 3D surface containing the top 50 percentile of the progenitor formation rate. This 3D overlap $O_{\rm 3D}$ is

defined just as in Eq. (2.8), however, now A, B, C, D, etc represent the volumes of the 50 percentile progenitors. Figure 2.16 represents the overlap (dark shaded region) of the 50 percentile of the progenitors of astrophysical and detectable mBBHs calculated about 4 BPS models (default, $\alpha(0.2)\lambda(1)$, $\alpha(0.3)\lambda(1)$, $\alpha(0.5)\lambda(1)$), shown for different SFR/MZR models. The union of all the areas is shown by the white shading. The 3D overlap fractions O_{3D} (mentioned in the figure caption) themselves are indicative of the relative agreement of the different models. Illustrating the power of the overlap technique, Figure 2.16 shows that the PP04_Ma16 SFR/MZR model shows the most consistency across the selected BPS models, and the KK04_Ma16 shows the largest variation between the BPS models by a factor of $\simeq 130$. Moreover, I show that the progenitor galaxies in T04 and M09 are in agreement across BPS models. Finally, the overlap calculations depict a stark difference between the astrophysical and detected population, with the latter showing large variation between models (note the log scale of the axes).

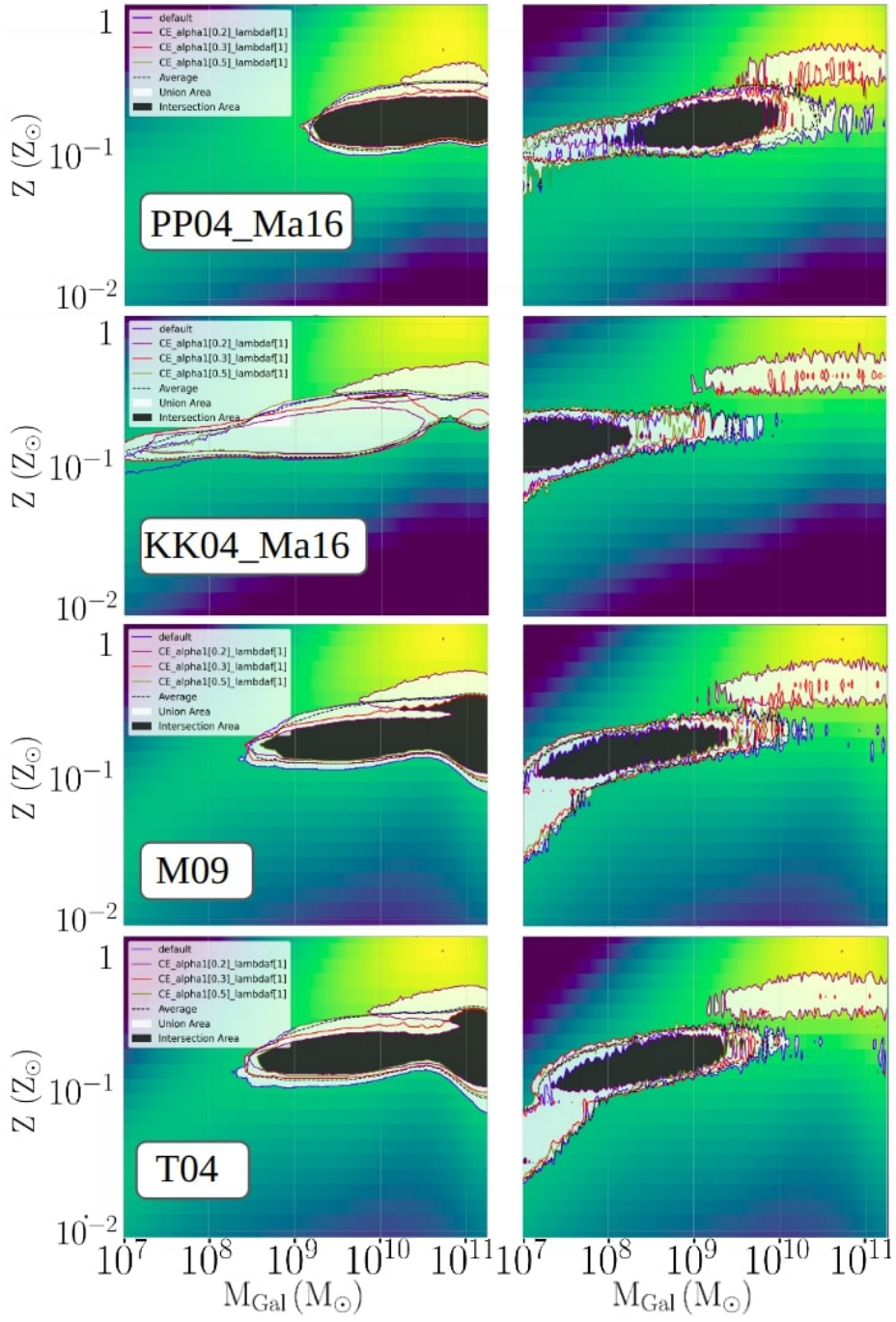

Figure 2.16: The overlap, shaded in black and shown on the left (right), of the 50% contours of the astrophysical (detected) progenitor formation rate for different BPS models. Different SFR/MZR models are shown from top to bottom. The representative BPS models are listed in the legend. The 3-dimensional overlap of the BPS contours for the SFR/MZR models of PP04_Ma16, KK04_Ma16, M09, and T04 is 44% (2%), 0.36% (0.033%), 50% (0.35%), 47% (0.48%) respectively. The color map depicts $\log_{10}$(SFRD) as a reference to illustrate the effect of the SFR on the overlapping region in the progenitor parameter space.

Chapter 3

Progenitor environments of merging binary black holes

To understand the effect of different models in predicting the progenitors of merging binary black holes (mBBHs), I generate 240 models from a combination of the 40 binary population synthesis (BPS) models and the star formation rates (SFRs) based on the 6 mass-metallicity relations. First, I discuss the present-day astrophysical merger rate for the different models and how it connects with the efficiency of forming mBBHs as a function of metallicity and the global stellar metallicity distribution in the Universe (§ 3.1). Then, in § 3.2, I show the progenitor environment predicted by the different combinations of models and highlight their main differences and common points. In § 3.3, I look at the selection bias introduced by gravitational wave (GW) detectors on the detected mBBH population and their inferred progenitor environment. Finally, in § 3.4, I describe the application of my method to produce posteriors of the formation galaxy properties with real observational data from a given GW detection, taking GW150914 as an example. The results presented in this chapter have been published in the Monthly Notices of the Royal Astronomical Society [Srinivasan et al., 2023].

3.1 Astrophysical merger rate

Figure 3.1, top, depicts the values of the present-day astrophysical merger rate (from § 2.3.1 and Eq. (2.4)), $R_0 \equiv R_{\rm mBBH}(z_{\rm mBBH} = 0)$, for my 240 models. For comparison, I show the 90% confidence range of R_0 inferred by the LVK collaboration (16 to 61 mergers $\mathrm{Gpc^{-3}yr^{-1}}$ from Table II of Abbott et al., 2023) after the O3 observing run. The merger rates from my models span about 2 orders of magnitude. For a given BPS model, the rates typically span a factor of 4 across SFR/MZR models. Globally, BPS models do not show much variation in the merger rates, with a few outliers with large deviations. For illustrative purposes in the

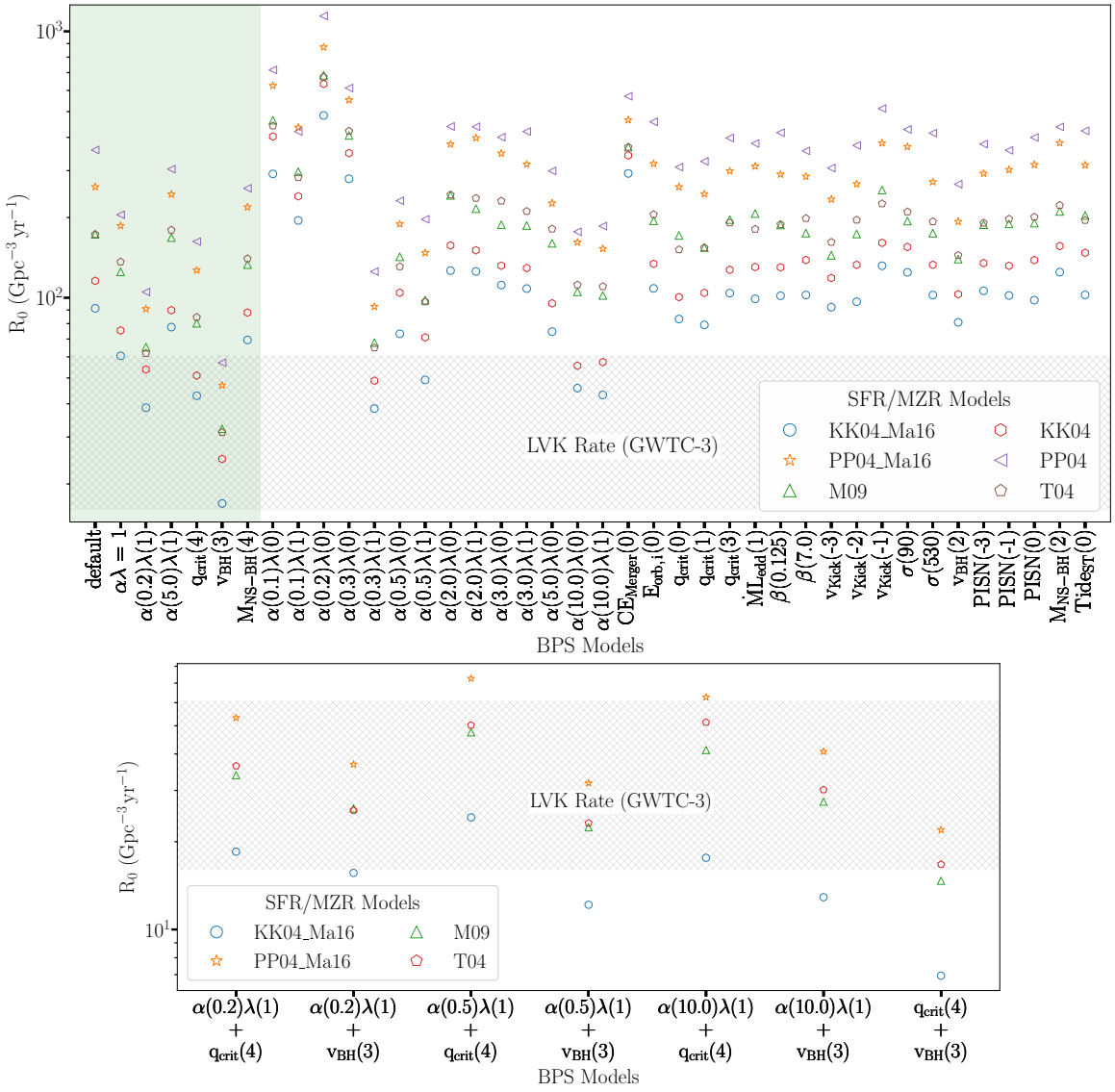

Figure 3.1: **Top**: Present-day astrophysical merger rate density of the different models. I show the merger rate in my binary population models along the x-axis and the different mass-metallicity models of the star formation rate are shown with different colors and symbols (legend). The hatched region designates LVK's 90% confidence interval of the inferred merger rate (Table II of Abbott et al., 2023) after O3. The BPS models shaded in green will be further explored in later sections. **Bottom**: Present-day merger rate of BPS models that vary from the default by two flags as indicated on the x-axis. In comparison to the top, the bottom figure illustrates that lower merger rates are attainable as one deviates further from the default model.

following analysis, I chose a subset of BPS models, highlighted in green, as representative of the 40 BPS models. These models were chosen to illustrate typical variations around the default model.

Almost all the models shown in Figure 3.1, top, predict effectively too high merger rates in comparison with LVK observations. Moreover, the range of R_0 spans almost 2 orders of magnitude. I emphasize the aim of my thesis is to understand the agreement and disagreement across models on the progenitor galaxy environment. The comparison with observations is a secondary consideration. Moreover, the galaxy stellar mass function that I incorporate (from Tomczak et al., 2014) contains a larger fraction of low-mass galaxies than other models which also favors the formation of merging BBHs. It is important to note that these BPS models correspond to 1-dimensional variations around the default choices (see Table A.1 of Appendix § A). Therefore, one can conclude that the consistently large rates irrespective of the SFR/MZR model show evidence that the underlying default BPS model proposed by COSMIC is too optimistic in forming mBBHs and are not the ones governing BBH formation in the Universe. As this study focuses on progenitor environments, I choose not to tune the BPS models in order to match the observed rate. However, as shown in Figure 3.1 bottom, certain combinations of parameters can potentially lead to rates that are compatible with the observations. Taking an example, using the KK04_Ma16 SFR/MZR and the default BPS model with two variations: $\alpha(0.5)\lambda(1)$ and $q_{\rm crit}(4)$ results in a merger rate $R_0 = 25\ \mathrm{Gpc^{-3}\ yr^{-1}}$, within the boundaries of the observed rate.

The wide range of rates suggests that caution should be used when interpreting the simulations. Still, global trends arise from my analysis. The uncertainties of the mass-metallicity relations (MZR) result in rate differences of roughly a factor 4, which is higher than the uncertainties of the bulk of the binary models I have explored here. This is consistent with other works, such as Neijssel et al. [2019], Tang et al. [2020], Briel et al. [2022], which find that differences in the star formation model, which includes the global star formation rate, mass metallicity relation and its spread, and galaxy stellar mass function, dominate the differences between the binary evolution models they explore, both for models based on simulations and observations. Broekgaarden et al. [2022] and Santoliquido et al. [2021] confirm these findings in a systematic exploration of models.

This suggests that the choice of MZR, and particularly its high redshift extension is a key parameter in modeling BBH mergers. Based on the models I have explored, MZRs with more low-metallicity star-forming gas such as the one from Pettini and Pagel [2004] are difficult to reconcile with observed BBH rates, especially when the low metallicity evolution is extrapolated beyond $z_{\rm f} \simeq 3.5$ [as in Chruslinska and Nelemans, 2019]. Fitting these MZR models with the measured LVK rates would require a typical decrease in the efficiency of forming merging BBH of more than an order of magnitude. The majority of my BPS models would require a reduction of a factor 2.

To understand the influence of the SFR/MZR models and mBBH formation efficiency on the merger rate R_0, I show the interplay between the mBBH formation efficiency and the

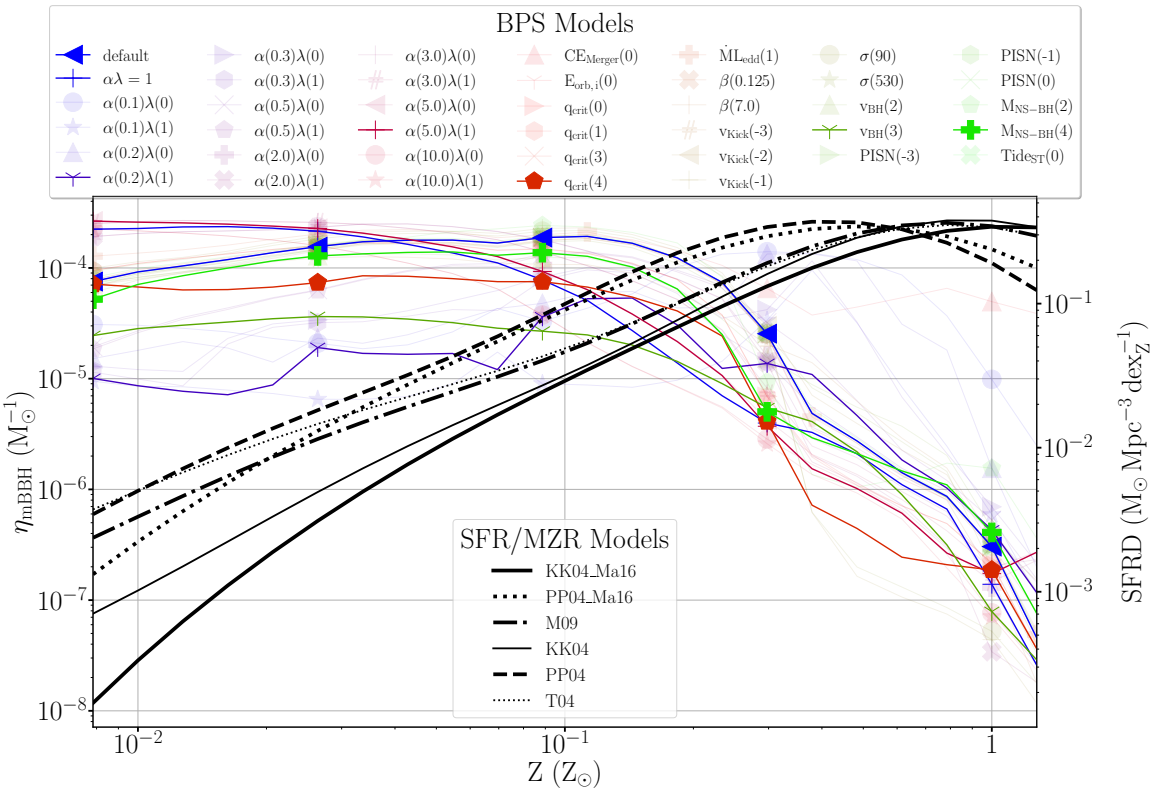

Figure 3.2: Efficiency of mBBH formation, $\eta_{\rm mBBH}$, as a function of metallicity Z. I show all the binary population models (upper legend) and highlight the models which are chosen for further analysis with brighter colors. I show in black, the star formation density for my different mass-metallicity models (lower legend).

star formation as a function of metallicity in Figure 3.2. Across BPS models, the mBBH formation efficiency sharply drops beyond low metallicities ($\gtrsim 0.1$ $Z_\odot$). This is due to increased mass loss from stellar winds resulting in a lower mass BH and a comparatively larger impact of supernova kick. In contrast, in all SFR/MZR models, the star formation drops in the low-metallicity region. As described in § 2.3.1, the progenitor formation rate depends on the product of the SFR and $\eta_{\rm mBBH}$ (Eq. (2.4)). As such, the region of $Z \simeq 0.1 - 0.3$ $Z_\odot$ dominates the production rate of merging black holes. whilst regions of very low metallicity ($Z \lesssim 0.01$ $Z_\odot$) do not contribute significantly because of the low star formation rate and the regions of very high metallicity ($Z \gtrsim Z_\odot$) do not contribute because of their low $\eta_{\rm mBBH}$. This comforts the choice of the metallicity range from 0.0078 $Z_\odot$ to 1.27 $Z_\odot$ that I use in my simulations (see § 2.2).

Figure 3.2 shows that one can expect the largest influence on the progenitor formation rate in intermediate metallicities, around 0.1 to 0.3 $Z_\odot$. Models with large efficiency in intermediate metallicities will tend to have higher progenitor formation rate and as a result have higher merger rates. As an example, the $\alpha(0.2)\lambda(1)$ model has consistently lower efficiency than the $v_{\rm BH}(3)$ model for all metallicities except between the crucial 0.1 to 0.3 $Z_\odot$. As a result, the merger rate of $\alpha(0.2)\lambda(1)$ is higher than that of $v_{\rm BH}(3)$.

For most BPS models, Figure 3.1 shows a consistent trend in the rates across SFR/MZR models: KK04_Ma16 and KK04 produce the lowest rates while PP04 and PP04_Ma16 produce the highest rates. T04 and M09 fall in between and with nearly equal rates. Again, this trend can be attributed to the metallicity dependence of the SFR/MZR models and $\eta_{\rm mBBH}$, as shown in Figure 3.2. As the efficiency of mBBH formation sharply drops off for $Z \gtrsim 0.2\,Z_\odot$, SFR/MZRs that favor lower Z (like PP04 and PP04_Ma16) will produce higher merger rates while SFR/MZRs that favour high Z (KK04_Ma16 and KK04) will result in low merger rates. The similar SFR/MZRs of T04 and M09 result in similar, intermediate merger rates. The high-redshift extrapolation from Chruslinska and Nelemans [2019] results in higher merger rates than the Ma et al. [2016] extension due to a faster decrease of the global metallicity at high redshifts. The consistently large rates of PP04 and PP04_Ma16 in comparison with that of GW observations indicate that either the default BPS model is overly optimistic and overproduces mBBH by more than an order of magnitude or that the calibration associated with the MZRs of PP04 and PP04_Ma16 [Pettini and Pagel, 2004] is in tension with the observations.

3.1.1 Mass spectrum

The global merger rate R_0 is a useful tool to evaluate a model's efficiency to produce mBBH. However, to understand the astrophysical population of each model, it is useful to look at the merger rate as a function of black hole mass. Figure 3.3 shows the mass spectrum of astrophysical black holes for the default model. For black holes with primary mass $30 - 40$ $M_\odot$, the default model is broadly consistent with LVK observations. Moreover, much like

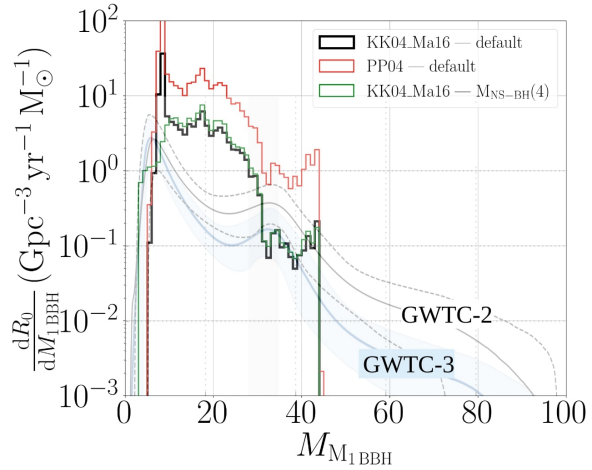

Figure 3.3: Astrophysical primary black hole mass distribution of mBBHs from my simulations (see legend) in comparison with that of the observation-based estimates from GWTC-3 [Abbott et al., 2023] and GWTC-2 [Abbott et al., 2021]. The 90% confidence interval of posterior population distribution from GWTC-3 is shown in blue shade and that of GWTC-2 is shown by the dotted black lines.

the trend in observations, there is a higher abundance of small black holes (< 30 M$_\odot$) in comparison to large black holes (> 30 M$_\odot$). This is primarily due to the decreasing power-law shape of the initial mass function of the progenitor stars (Figure 1.5), and also due to the large abundance of high metallicity stars in the Universe (2.5). However, the effect of the overly optimistic merger rates of my models is evident in the low mass region which shows significant deviation from observations. This same effect is not quite seen in high-mass black holes due to the effect of the PPISN mechanism. Furthermore, the PISN prescription prevents black holes of mass > 45 M$_\odot$from forming altogether. Moreover, I do not model the dynamical mergers of black holes in dense stellar clusters that can give rise to higher black hole masses.

In Figure 3.3, I also show examples from models that influence the black hole mass due to different metallicity and supernova models. The higher mass spectrum of the PP04 model in comparison with the default KK04_Ma16 is primarily due to the increased merger rate of the former. PP04's relatively large abundance of lower metallicity progenitors (Figure 2.6) further increases the merger rate of high-mass black holes. I also show $M_{\rm NS-BH}(4)$ which lacks a neutron star - black hole mass gap due to the delayed supernova fallback prescription. The lowest black hole mass of $M_{\rm NS-BH}(4)$ is $\simeq 3$ M$_\odot$, in lieu of the default $\simeq 5$ M$_\odot$. As a result, the peak in the default mass rate at $\simeq 7$ M$_\odot$ is absent $M_{\rm NS-BH}(4)$.

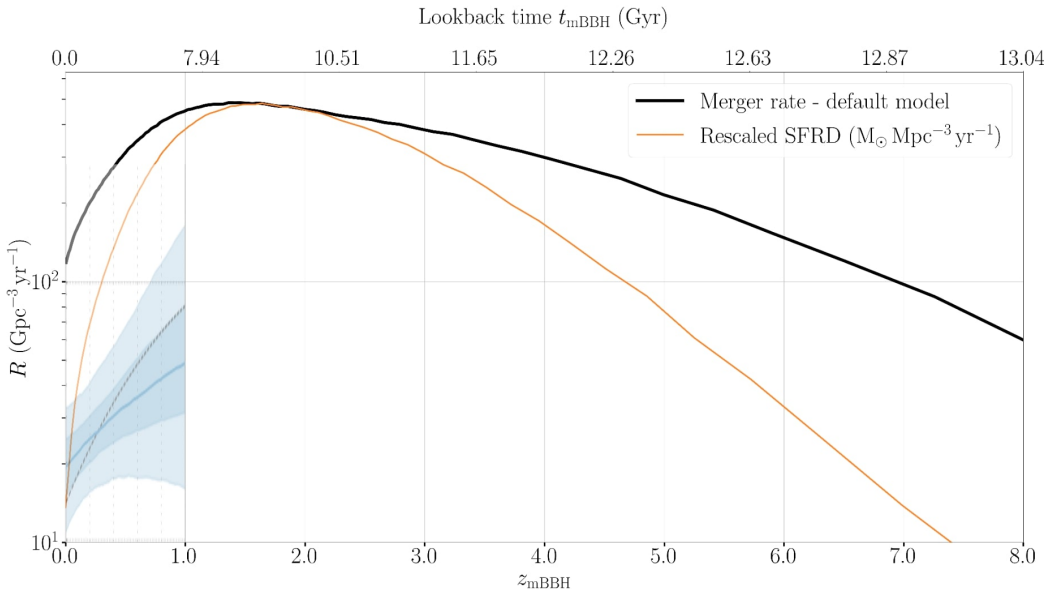

Figure 3.4: Merger rate of my default simulation model, in black, as a function of the redshift of merger $z_{\rm mBBH}$. The LVK estimation of the merger rate evolution from Abbott et al. [2023] is shown in blue: the light and dark shades corresponds to the 90% and 50% confidence intervals respectively. For comparison, the SFR of the default model (KK04_Ma16) is re-scaled and shown in orange.

3.1.2 Merger rate evolution

Using the relation derived in § 2.3.1, in Figure 3.4 I show the merger rate evolution, $R(z_{\rm mBBH})$, of my default model (black line) in comparison with LVK observations (blue shade). Although the initial merger rate R_0 is over-estimated in my model, both observations and the default model show a monotonous increase in the merger rate. Unlike LVK observations which have rate measurements up to redshift 1 due to limitations of the detector sensitivity, my simulation extends up to a merger redshift of $\simeq$ 7-8. The figure also shows that the peak black hole merger rate occurs at around redshift 1.19 (8.6 Gyr ago). This follows after the peak in star formation which occurs at redshift $\simeq$ 1.53 (9.6 Gyr ago). The delay between the peak in SFR and merger rate is primarily due to large number of systems with similar delay times ($\lesssim$ 1000 Myr) as shown in the delay time histogram of Figure 2.12.

3.2 Astrophysical progenitor formation rates

3.2.1 Global trends

Figure 3.5 depicts the progenitor galaxy mass and redshift (or equivalently look-back time) of the formation of mBBHs. The color map shows the global star formation rate density of each model. In the 1-dimensional distributions, all my models present a tri-modal distribution of the typical formation galaxy, with variations owing to the specific MZR or BPS model. One can observe three peaks in progenitor formation rates at $M_{\rm Gal} = 10^7$ M$_\odot$, $M_{\rm Gal} \simeq 3 \times 10^9$ M$_\odot$ and $M_{\rm Gal} \simeq 10^{11}$ M$_\odot$. In comparison, the global SFRD is strongly dominated by massive galaxies ($M_{\rm Gal} \gtrsim 2 \times 10^{10}$ M$_\odot$). This strong SFRD at high $M_{\rm Gal}$ and high $z_{\rm f}$ ($\gtrsim 2$) causes the corresponding high mBBH formation rate. As such, the peak of SFRD (cross in the two dimensional plots) always lies within the contour of mBBH progenitor formation rate. At high galaxy masses, the mBBH progenitor formation can be well mapped to the global star formation, with a small shift towards higher redshifts.

Away from the peak SFRD, at low redshifts ($z_{\rm f} \lesssim 1$), the progenitor contours significantly deviate from the SFRD and favor dwarf galaxies ($M_{\rm Gal} < 10^9$ M$_\odot$) across most BPS models, irrespective of the SFR/MZR model. This is primarily due to the abundance of low-metallicity star-forming gas in dwarf galaxies (see § 2.1) which have the highest efficiencies of mBBH formation (Figure 3.2). This effect causes the upturn for dwarf galaxies that is present in most of the models, except for the ones which have comparatively small efficiencies at low metallicity ($Z \lesssim 0.1$ Z$_\odot$), for e.g., the $\alpha(0.2)\lambda(1)$ model. In models with the highest efficiency at low metallicity ($\alpha\lambda$=1 and $\alpha(5)\lambda(1)$ models) formation in dwarf galaxies can be equal to (for the KK04 and M09 MZRs) or larger than (for the KK04_Ma16 MZR) the contribution from the most massive galaxies.

Figure 3.6 shows the progenitor Z and $z_{\rm f}$ for the same models. In all my BPS models, the metallicity region of 0.1-0.3 Z$_\odot$ strongly contributes or even dominates the formation of mBBH progenitors, irrespective of formation time. As an example, looking at the 1-dimensional plots (top row) for the default, $\alpha(0.2)\lambda(1)$, $q_{\rm crit}(4)$, and $M_{\rm NS-BH}(4)$ BPS models, the fraction of systems with $Z \in$ 0.1 - 0.3 Z$_\odot$ is at least 50%. As described in § 3.1, this is due to the interplay between the SFR which favors high metallicities and $\eta_{\rm mBBH}$ (Figure 3.2) which favors low metallicities. Outside the 0.1-0.3 Z$_\odot$ metallicity range, the overlap across different BPS models can be very limited due to the large dependence on metallicity in BPS modeling.

Looking at the 2-dimensional $z_{\rm f}$-Z plane of Figure 3.6, throughout cosmic history, the progenitor metallicity shows a wide distribution centered at 0.1-0.3 Z$_\odot$. For all models, the metallicity distribution of the progenitors narrows with decreasing redshift, and again, this can be attributed to the combination of the SFR and the efficiency of mBBH formation, $\eta_{\rm mBBH}$. The plots of M09 and KK04 calibrations show a correlation at high redshift ($z_{\rm f} \gtrsim 3$) between the contour of the progenitor formation rate and the global SFR. This is

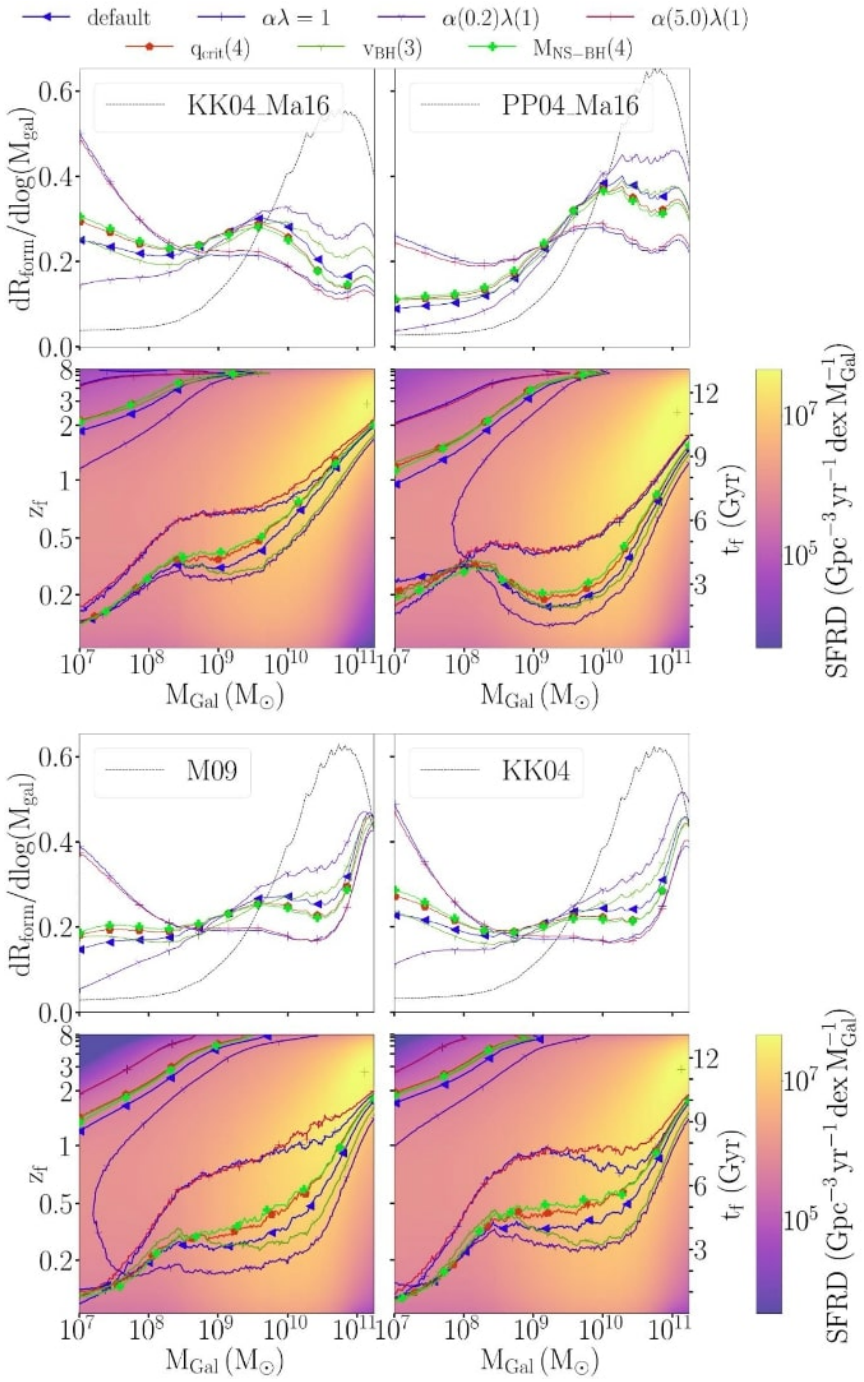

Figure 3.5: Typical formation galaxy mass and formation time redshift (or equivalently lookback time t_f) of merging black holes. In the second and fourth row, I show the contours containing 90% of the progenitor formation rate in terms of present-day galaxy mass and time of formation, for different binary population synthesis models (colored lines with symbols) and different mass-metallicity models in each 2 × 1 panel (mentioned in the label). The logarithmic color map depicts the global star formation rate in each model for comparison. In the first and third rows, I show the same distributions, summed over formation time, with the corresponding star formation model shown with the black dotted line.

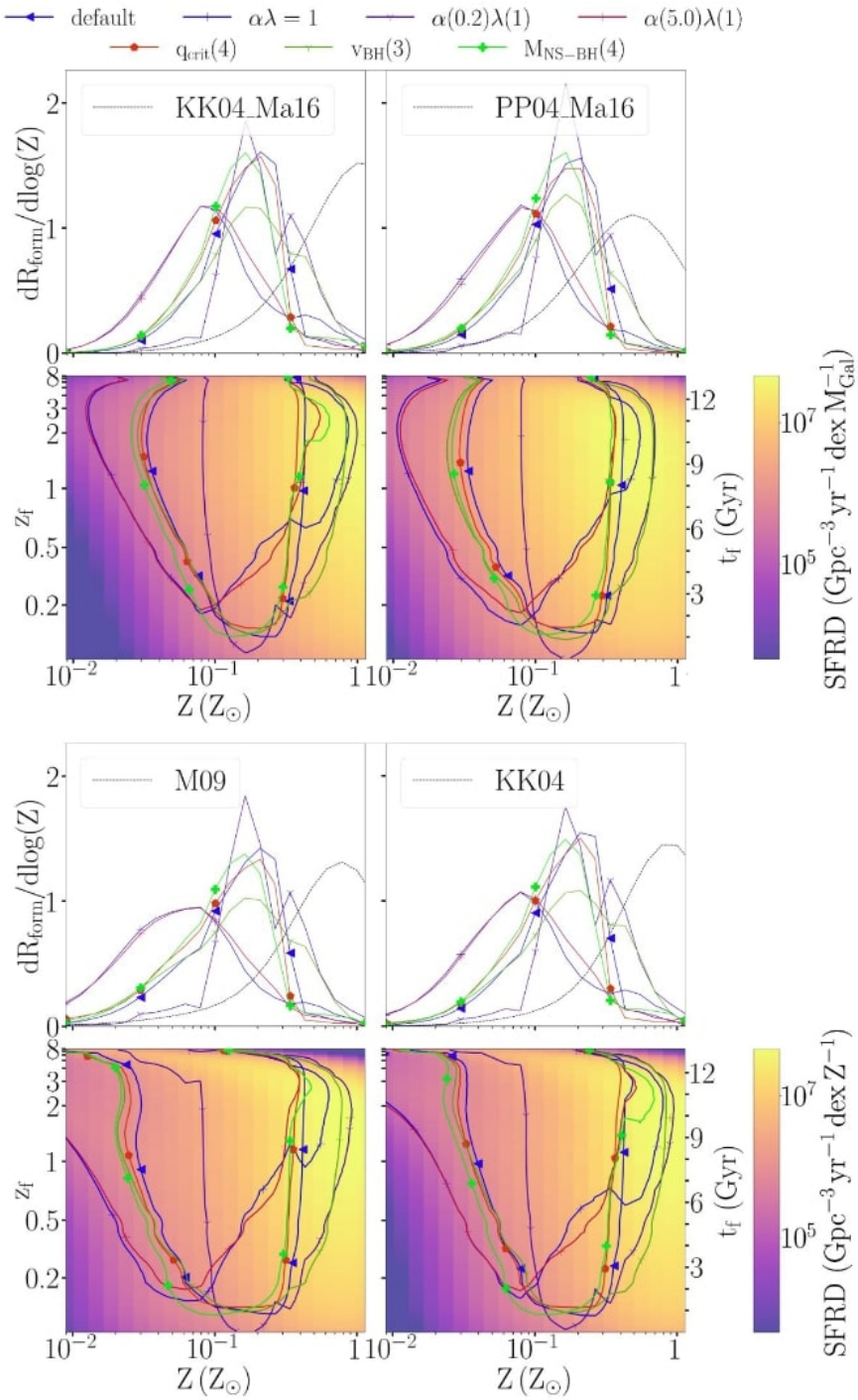

Figure 3.6: Typical formation galaxy metallicity and formation redshift (or equivalently, lookback time $t_{\rm f}$) of merging black holes. In the second and fourth row, I show the contours containing 90% of the progenitor formation rate in terms of galaxy metallicity and time of formation, for different binary population synthesis models (colored lines with symbols) and different mass-metallicity models in each 2×1 panel (mentioned in the label). The logarithmic color map depicts the global star formation rate in each model for comparison. In the first and third row, I show the same distributions, summed over all formation time, with the corresponding star formation model shown with the black dotted line.

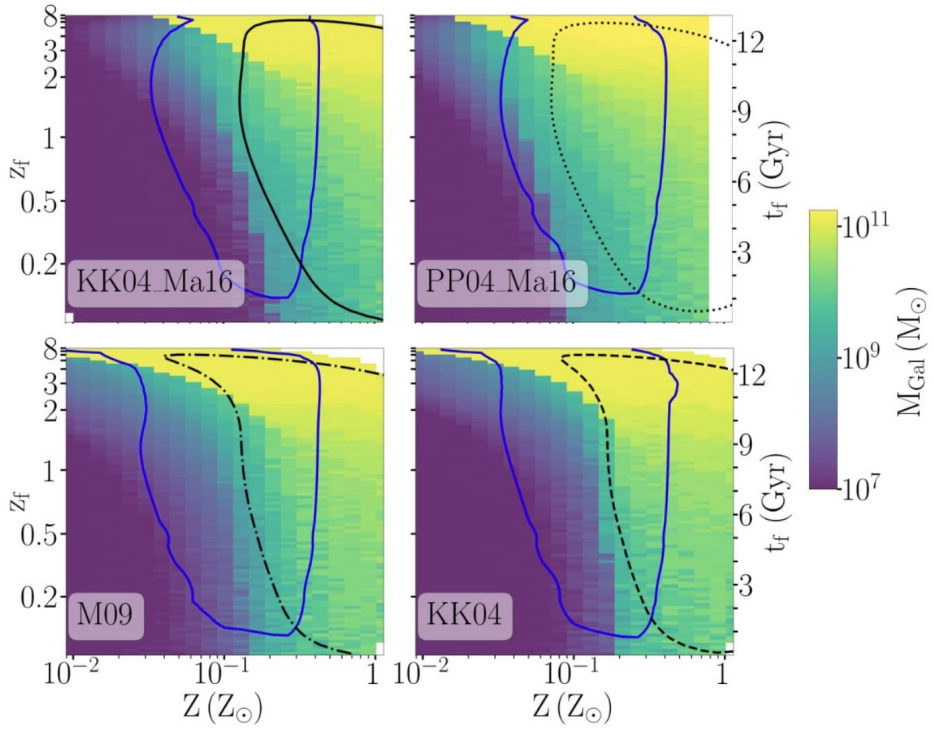

Figure 3.7: Typical formation galaxy mass of merging binary black holes. The logarithmic color map shows the $M_{\rm Gal}$ with the maximum progenitor formation rate for a given Z and $z_{\rm f}$. The blue contours contain 90% of the progenitor formation rate of my default binary population synthesis model and the black contours contain 90% of the star formation rate for different mass metallicity models. The white spaces correspond to the progenitor formation rates that fall below the resolution of my simulation.

the region of the SFR which is extrapolated based on the assumption of the high redshift evolution of the MZR. In these SFR/MZR models, most of the star formation occurs at low metallicity ($Z < 0.1\,{\rm Z}_\odot$) for $z_f > 3$ (see the yellow extension towards the upper left corner in Figure 2.6). Figure 3.2 shows that the efficiency of mBBH formation does not vary significantly in this metallicity region. Therefore, the BPS contours directly trace the SFR at high $z_{\rm f}$. With decreasing $z_{\rm f}$ the increasingly high metallicity causes the lower metallicity limit of the colored contours containing 90% of the progenitor formation rate to shift slightly towards higher metallicities. However, a deciding factor that places an upper limit on the metallicity of progenitors ($Z \lesssim 0.5\ {\rm Z}_\odot$) is the nearly constant $\eta_{\rm mBBH}$ for low metallicities ($Z < 0.1\,{\rm Z}_\odot$) and its rapid decline for higher values ($Z > 0.2\,{\rm Z}_\odot$). Thus the progenitor contours generally favor lower metallicities as compared to the SFR, while also slightly shifting towards higher metallicities at lower redshifts, hence its narrowing shape.

To help elaborate further, Figure 3.7 shows the mode of the distribution of formation

galaxy masses of mBBH progenitors for a given Z and z_f for the default BPS model. Low-metallicity progenitors tend to come from dwarf galaxies ($M_{\rm Gal}$ <10^9 $M_\odot$) while larger galaxies have higher metallicities. At large z_f, most of the progenitor formation is driven by the SFR, meaning that across Z, the progenitors are mostly present in galaxies that would now be massive. At lower z_f, stars in massive galaxies have increasingly high metallicity while low-metallicity environments can be found in dwarf galaxies.

Looking closely at the trends in individual BPS models, the $\alpha(0.2)\lambda(1)$ model stands out along the three dimensions of my star formation models (see Figures 3.5-3.6). The $\eta_{\rm mBBH}$ of this specific BPS model has a peculiar shape with low efficiency at high and low Z while peaking between 0.1 and 0.2 $Z_\odot$. As a result, the progenitor formation rate is concentrated within 0.1-0.2 $Z_\odot$. This implies that the formation rate contours are also smaller in $M_{\rm Gal}$ versus z_f and Z versus z_f. On the other hand, the contours for $\alpha\lambda(1)$ and $\alpha(5.0)\lambda(1)$ models show a large overlap as a result of their very similar $\eta_{\rm mBBH}(Z)$ seen in Figure 3.2.

Combined uncertainties on both binary/stellar evolution and star formation make the inference of the birth conditions (formation galaxy mass, metallicity, and cosmic time) non-trivial, especially for the typical formation galaxy mass. Still, I find that in all the models I explored, the most likely progenitor metallicity is around Z$\simeq$ 0.2 $Z_\odot$ and is narrowly peaked. Liotine et al. [2023] have also found similar trends in the mBBH progenitor metallicity, further highlighting its significance. This effect translates from the interplay between the mBBH formation efficiency, and the star formation rate as a function of metallicity (Figure 3.2). Based on the range of models presented here, I find that one can predict the typical progenitor metallicity for merging BBHs formed through different BPS models provided the corresponding $\eta_{\rm mBBH}$(Z) and a star formation model.

The determination of the typical formation times is also rather consistent across models, with a steady increase of progenitor formation up to a look-back time of $\simeq$ 10 Gyr. Beyond that, I find that the formation rate decreases in my models using the Ma et al. [2016] metallicity evolution at high redshift. On the other hand, models based on the Chruslinska and Nelemans [2019] extrapolation at high redshift show a sharp peak of progenitor formation more than 12 Gyr ago, owing to the low-metallicity gas. This is consistent with the findings of Graziani et al. [2020], who find a typical formation time lies between 6 < z_f< 8. Within the models I have explored, different binary evolution models show limited differences in their typical formation times. This is because the delay time distributions prefer short timescales and the combination of the wide range of metallicities tends to wash out strong features in the delay time distributions.

The largest uncertainty is for the determination of the typical formation galaxy. Figure 3.5 shows three peaks whose heights vary strongly depending on both binary and MZR models. Extracting global trends of the progenitor environment based on the mBBH formation efficiency and global star formation model seems unclear at this point. Still, my results show agreement with the analysis of Santoliquido et al. [2022] where the authors

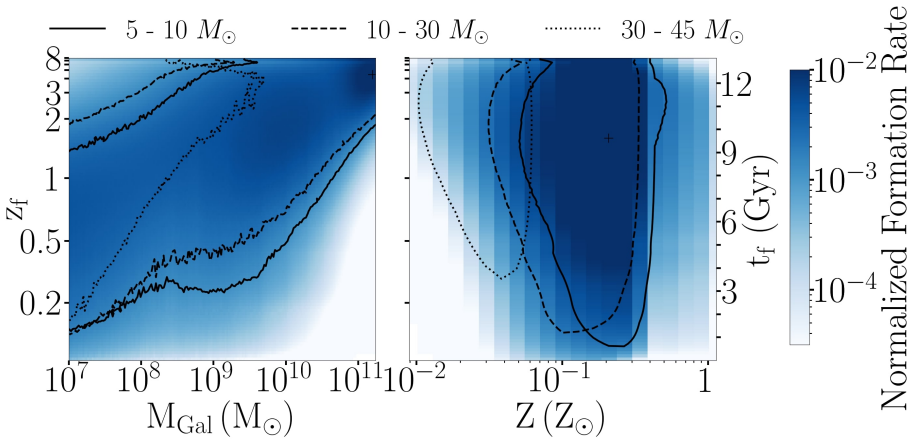

Figure 3.8: **Top**: Typical progenitor galaxy mass, metallicity, and time of formation for merging black holes with different ranges of primary black hole mass, $M_{1,\mathrm{BBH}}$. The logarithmic color map shows the normalized progenitor formation rate for all mass ranges. The contours contain 90% of the progenitor formation rate, for different $M_{1,\mathrm{BBH}}$ ranges (legend) as a function of M_{Gal} versus z_{f} (left) and Z versus z_{f} (right). I use my default model of the mass-metallicity relation (KK04_Ma16) and binary population synthesis.

simulate the merger rate, formation galaxy and merger host galaxy of compact objects using observational scaling relations. Using an MZR similar to ours [Chruslinska and Nelemans, 2019] to build their SFR, and BPS models probing different values of the CE efficiency (α), they find that mBBHs tend to form in low mass, low-metallicity galaxies, with a metallicity mode $\simeq$ 0.1 $Z_\odot$ for a range of redshifts. They additionally show that BBHs tend to merge in more massive galaxies, as dwarf galaxies merge into more massive ones.

3.2.2 Effects of the black hole mass

Taking my default SFR/MZR model and BPS model (KK04_Ma16, default respectively), I look at the typical progenitor environment for black holes of different masses. For simplicity, I consider the mass of the primary black hole, defined as the larger of the two merging black holes. In practice, almost all the BHs have an almost equal mass ratio.

Figure 3.8 shows the contours containing 90 % of the formation of BH merger progenitors for three ranges in primary black hole mass $M_{1\,\mathrm{BBH}}$: 5-10 $M_\odot$, 10-30 $M_\odot$, and 30-45 $M_\odot$. The color map shows the overall normalized progenitor formation rate. The plot on the right shows that with increasing primary black hole mass, the progenitor contours favor lower metallicities (see § 2.2). The black hole mass only indirectly depends on M_{Gal} and z_{f} which correlates with Z through the SFR. For example, massive black holes tend to be formed from low-metallicity progenitors. Figure 3.7 shows that low-metallicity progenitors

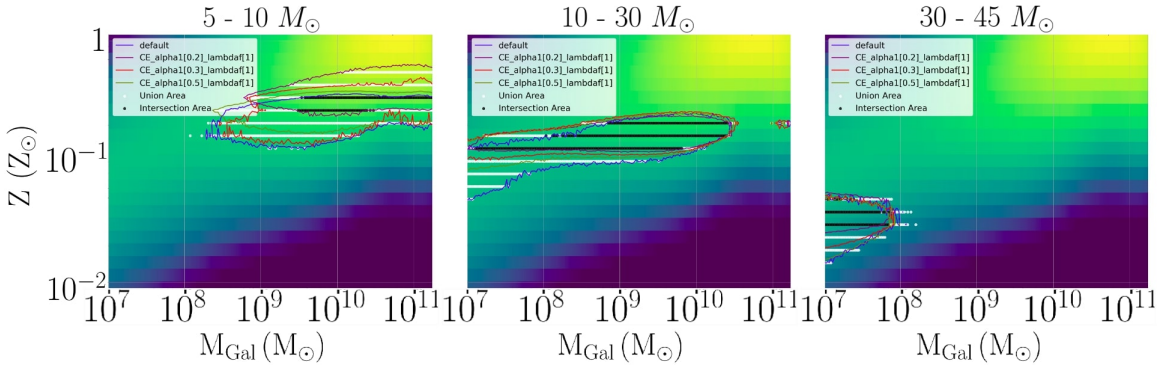

Figure 3.9: Progenitor contours containing 50% of the progenitor formation rate for 4 example BPS models (default mass-metallicity relation, KK04_Ma16) showing overlapping trends. From left to right, I show the contours for increasing primary black hole mass ranges 5-10 $M_\odot$, 10-30 $M_\odot$, and 30-45 $M_\odot$. The region of intersection is depicted with black lines and the region of union is shown with white lines. The overlap (i.e., ratio of the intersection and union areas) of the progenitor contours are 20%, 53%, 42% respectively. The colormap shows the SFRD of KK04_Ma16 for context.

are found both at low redshifts in typically low-mass galaxies and at high redshifts in a wide range of galaxy mass. Combining all BH masses (color map), I recreate the global trends in the progenitor formation rate that is shown in Figures 3.5-3.6.

Using the overlap metric, defined as the ratio of the intersection and union areas, I am able to determine that this trend is seen in most of the 240 models. As an example, Figure 3.9 shows the overlap of the *50%* contours of a few BPS models. Here, the trend in the black hole mass - galaxy mass correlation is evident and consistent across models.

3.3 Progenitors of detectable merging black holes

Using the astrophysical population of mBBH, I explore the detected population and the effect of GW detector selection effect on the inference of the progenitor formation environment. Figure 3.10 shows the progenitor $M_{\rm Gal}$ and $z_{\rm f}$ for mBBHs that are detectable (i.e., individual detector SNR > 6, network SNR > 12) by the LIGO-Virgo three-detector network in the O3 configuration. The 1-dimensional plot shows fewer variations across BPS models as compared to the astrophysical progenitors in Figure 3.5. This indicates that the detection bias largely limits the fraction of the astrophysical mBBH population current detectors can observe.

Moreover, there is a large overlap in the contours of the 2-dimensional plot in two distinct progenitor environments: high $z_{\rm f}$ (> 2), large $M_{\rm Gal}$ (>$10^{10.5}$ $M_\odot$) progenitors and

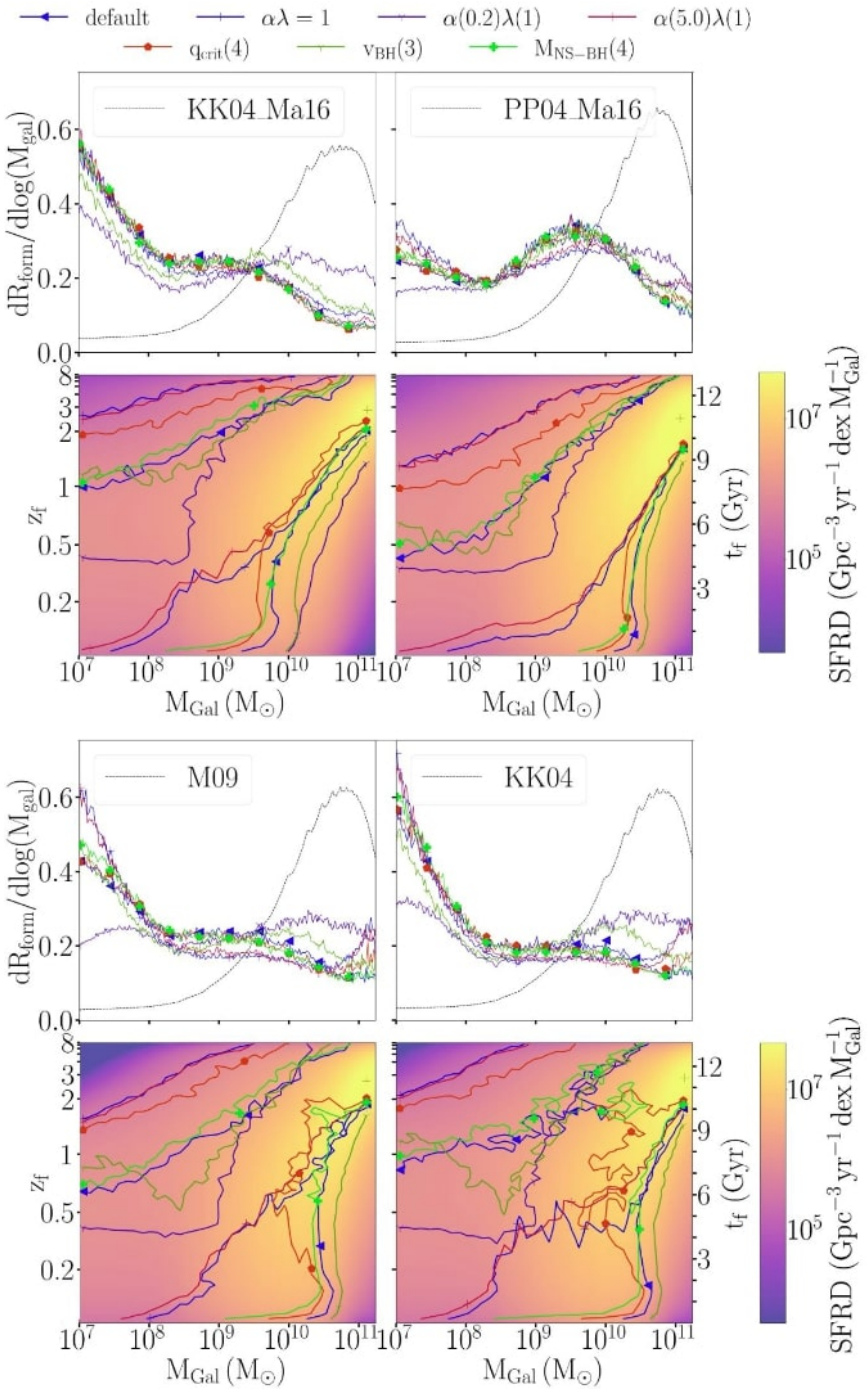

Figure 3.10: Typical formation galaxy mass and formation redshift (or equivalently, look-back time $t_{\rm f}$) of detectable merging black holes. In the second and fourth row, I show the contours containing 90% of the progenitor formation rate in terms of galaxy mass and time of formation, for different binary population synthesis models (colored lines with symbols) and different mass-metallicity models in each 2×1 panel (mentioned in the label). The logarithmic color map depicts the global star formation rate in each model for comparison. In the first and third row, I show the same distributions, summed over all formation time, with the corresponding star formation model shown with the black dotted line.

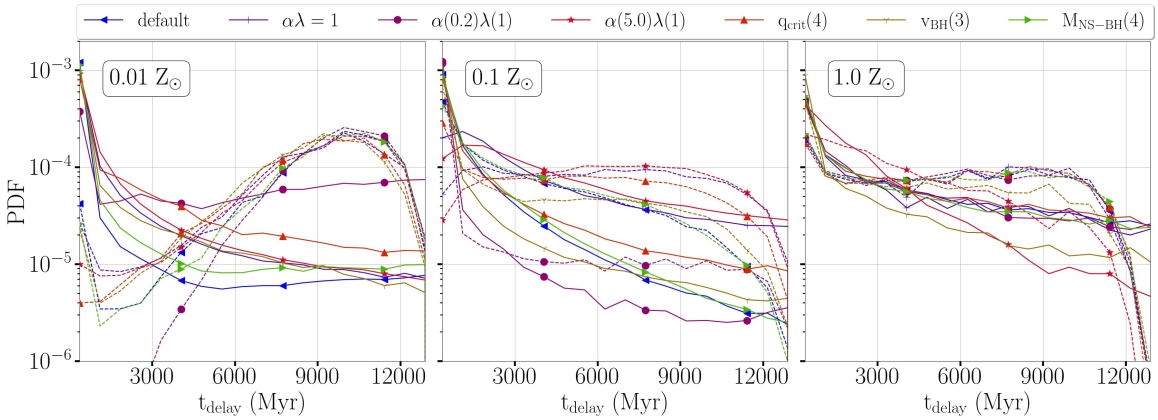

Figure 3.11: Normalized histogram of the delay time ($t_{\rm delay}$) of the mBBHs from the subset of the astrophysical population $Pop_{\rm Astro}$ that are detectable (dashed lines), and from $Pop_{\rm BPS}$ of the binary population synthesis simulation (solid lines), for different BPS models (colors and symbols), across 3 metallicity bins: 0.01 $Z_\odot$ (left), 0.1 $Z_\odot$ (center), 1 $Z_\odot$ (right). Figure 2.12 showed the $t_{\rm delay}$ histogram just from the BPS simulation, whereas here, I show its comparison with that of the detected population.

low $z_{\rm f}$, small $M_{\rm Gal}$ ($< 10^{10}$ $M_\odot$) progenitors. Comparing with the astrophysical progenitors in Figure 3.5, it is evident that the abundance of astrophysical progenitors at high $z_{\rm f}$, in large $M_{\rm Gal}$ has influenced the progenitors of detected mBBHs in the same part of the parameter space, albeit, with a very low formation rate as shown in the 1-dimensional plot (KK04_Ma16 with default BPS progenitor formation rate in massive galaxy fall by a factor of 2 in the detected population).

Across all models, the progenitor formation at low $z_{\rm f}$ in small $M_{\rm Gal}$ ($< 10^{10}$ $M_\odot$) galaxies is more prominent than in the case of the astrophysical population. The inverse relation between the signal-to-noise ratio (SNR) and luminosity distance implies that the detectors are biased towards a low redshift of the merger. To analyze the relationship between the redshift of merger and the redshift of progenitor formation, I look at the distribution of the delay time defined as the time interval between the formation of the binary stars to the merger of BBH. Figure 3.11 shows the delay time distribution of mBBHs for 3 metallicities for the subset of the astrophysical population $Pop_{\rm Astro}$ that are detectable (dashed lines) and for systems from the BPS simulation $Pop_{\rm BPS}$ (solid lines). Note that the $t_{\rm delay}$ of $Pop_{\rm BPS}$ was discussed in Figure 2.12 and is also shown here for comparison. I do not show the global $Pop_{\rm Astro}$ as they closely follow the BPS curves, but with a sharp drop in the number of systems with $t_{\rm delay} \gtrsim 10$ Gyr as these systems generally fail to merge by the present-day. The vast majority of delay times in the BPS simulation are short, implying that the merger redshift closely follows the formation redshift $z_{\rm f}$ for the astrophysical population. However, considering the detectable mBBH population, the bias towards detecting mergers at low

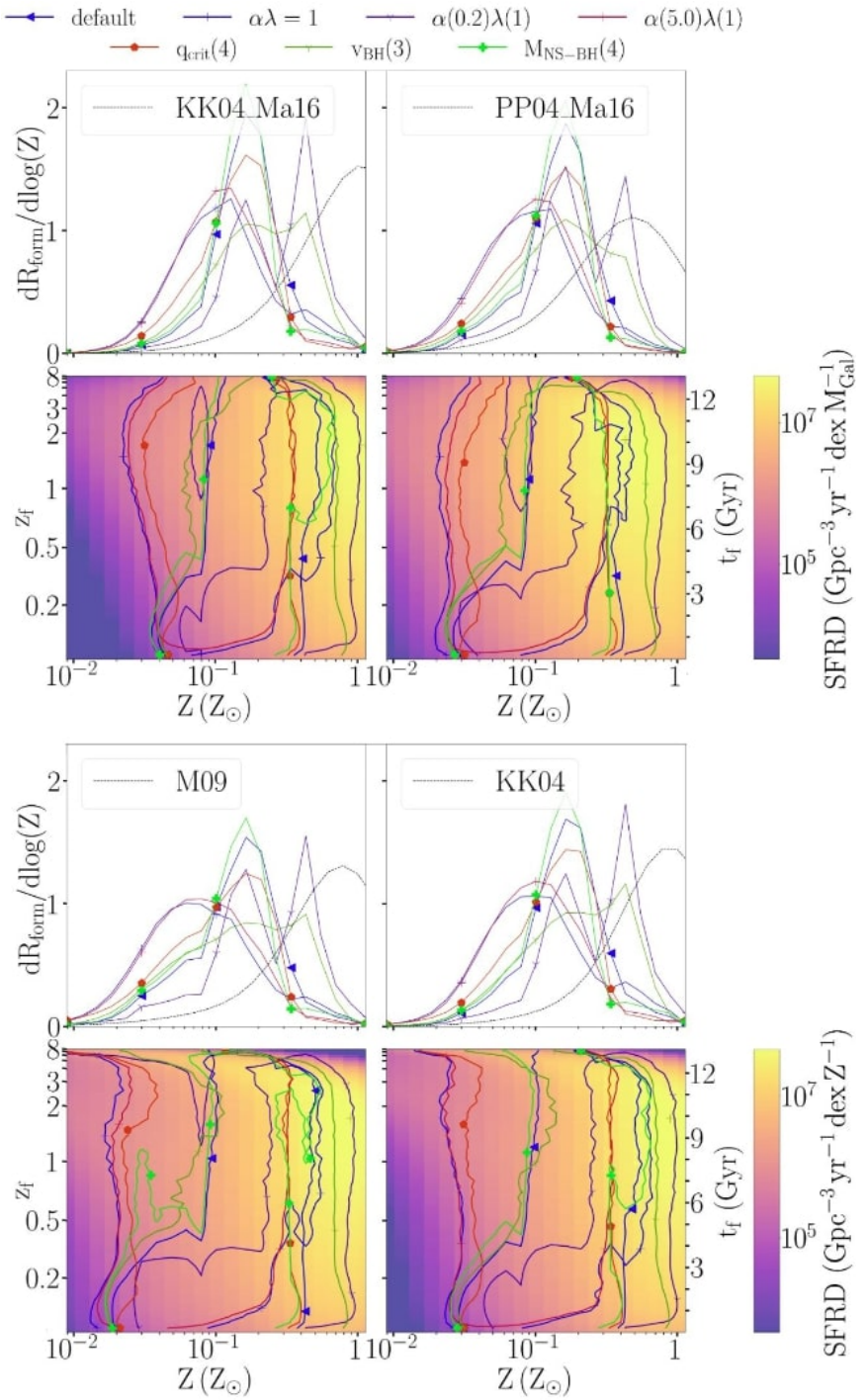

Figure 3.12: Typical formation galaxy metallicity and formation redshift (or equivalently, lookback time t_f) of detectable merging black holes. In the second and fourth row, I show the contours containing 90% of the progenitor formation rate in terms of galaxy metallicity and time of formation, for different binary population synthesis models (colored lines with symbols) and different mass-metallicity models in each 2×1 panel (mentioned in the label). The logarithmic color map shows the global star formation rate in each model for comparison. In the first and third row, I show the same distributions, summed over all formation time, with the corresponding star formation model shown with black dotted line.

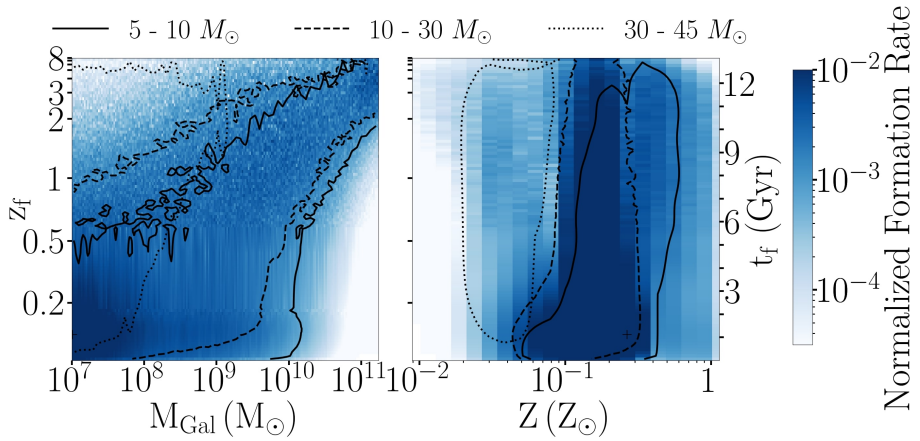

Figure 3.13: Typical progenitor galaxy mass, metallicity, and time of formation for *detected* merging black holes with different ranges of primary black hole mass, $M_{1,\mathrm{BBH}}$. The logarithmic color map shows the normalized progenitor formation rate for all mass ranges. Contours contain 90% of the progenitor formation rate, for different $M_{1,\mathrm{BBH}}$ ranges (legend) as a function of M_{Gal} versus z_{f} (left) and Z versus z_{f} (right). I use my default model of the mass-metallicity relation (KK04_Ma16) and binary population synthesis.

redshift, in combination with the influence of the SFR towards high z_{f} progenitors, it seems, results in a preference towards long delay times.

Figure 2.6 showed that the astrophysical formation rate of high metallicity ($Z > 0.1$ $Z_\odot$) stars is much higher than that of low-metallicity stars. As such, I expect high redshift progenitors of detected systems to have $Z > 0.1$ $Z_\odot$. Figure 3.12 indeed shows that the concentration of progenitors at high z_{f} corresponds to higher Z (> 0.1 $Z_\odot$). This also contributes to the slight shift towards higher metallicities in the 1-dimensional plot as compared to the astrophysical metallicity distribution (Figure 3.6). The first peak in the 1-dimensional plot between 0.1-0.3 $Z_\odot$ is due to the astrophysical bias, while the second peak around $Z \simeq 0.5$ $Z_\odot$ is due to the large delay times of mBBHs from high z_{f}. Furthermore, there exists a secondary detector bias towards larger black holes due to their larger GW signal amplitude which plays a role in selecting low-metallicity progenitors. This can be seen in the low z_{f} progenitors of the 2-dimensional plots of Figure 3.12.

Figure 3.13 shows the progenitor distribution of detected mBBHs for different primary black hole masses. The majority of detected mBBHs come from dwarf galaxies, at low z_{f}, and with metallicity of 0.1 to 0.3 $Z_\odot$. This is in good agreement with existing progenitor predictions of GW events [Lamberts et al., 2016]. Massive black holes are predominantly formed in low mass galaxies ($< 10^{10}$ $M_\odot$) and with lower metallicities (≤ 0.1 $Z_\odot$) as compared to smaller black holes, which in contrast, arise from a wide range of galaxy masses and higher metallicities (≥ 0.3 $Z_\odot$).

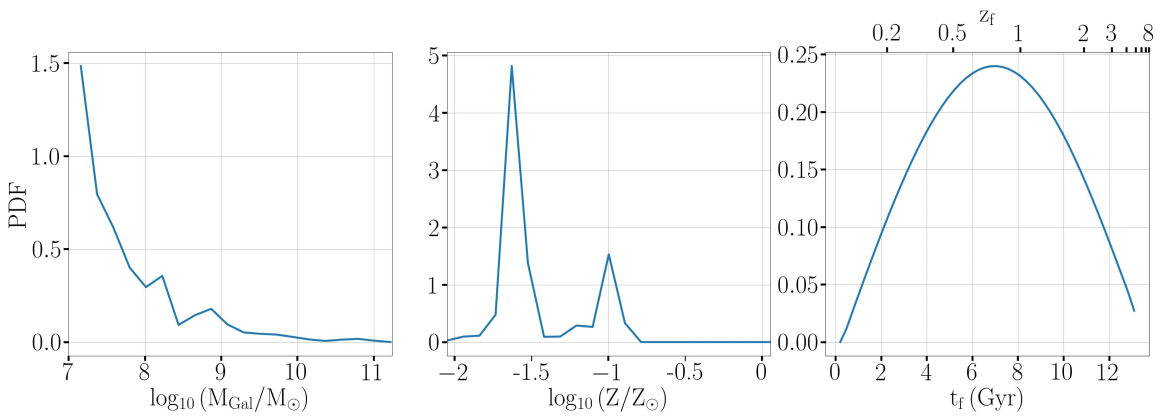

Figure 3.14: Posterior probability density function (PDF) of the progenitor galaxy mass $M_{\rm Gal}$, metallicity Z and time of formation $t_{\rm f}$ for the first detected gravitational wave event (GW150914) based on my default star formation model (KK04_Ma16) and binary evolution model (default COSMIC). This illustrates the method described in § 2.3.3 to produce progenitor posteriors given posterior samples of a detected merger.

3.4 Posterior generation pipeline

As shown by Eq. (2.6), I can produce a posterior distribution of the progenitor galaxy properties ($M_{\rm Gal}$, Z, $z_{\rm f}$) for a GW event using my model and given the posterior samples of the mBBH masses and luminosity distance. Figure 3.14 shows the progenitor environment of the first discovered mBBH event, GW150914 [Abbott et al., 2016a], for my default model (KK04_Ma16 with default BPS flags). It distinctly shows that GW150914 likely came from a dwarf galaxy ($M_{\rm Gal} \lesssim 10^9$ M$_\odot$) with very low metallicity ($Z \simeq 0.025$ Z$_\odot$), and with a broad distribution of progenitor formation look-back time which peaks at a corresponding redshift of $z_{\rm f} \simeq 1$. This is consistent with the initial study of [Abbott et al., 2016b, Lamberts et al., 2016, Marassi et al., 2019] of the GW event. The secondary peak in metallicity follows from the peak in astrophysical formation rates at around 0.1 Z$_\odot$, as discussed in detail in § 3.2.1. The primary peak in metallicity is due to GW150914's combination of a high-mass BBH merging at close proximity. We can see in Figure 1.7 that a remnant mass BH $\simeq$ 70-80 M$_\odot$, which was the mean total mass of GW150914, can be formed from progenitors with $Z \simeq 0.01$ Z$_\odot$ (consistent with Figure 3.13). This low metallicity is typically seen in dwarf galaxies, especially in low $z_{\rm f}$, as shown in Figure 3.7. The broad posterior distribution in $t_{\rm f}$ is due to the presence of dwarf galaxies with low metallicities at almost all redshifts, as can be inferred from Figure 3.7. I find that the progenitor posteriors prediction from other BPS and SFR/MZR models broadly agree that GW150914 had a low metallicity ($Z \lesssim 0.1$ Z$_\odot$) dwarf galaxy ($M_{\rm Gal} \lesssim 10^9$ $M_{\rm Gal}$) progenitor with small deviations depending on the different values of $\eta_{\rm mBBH}(Z)$ value of each BPS model.

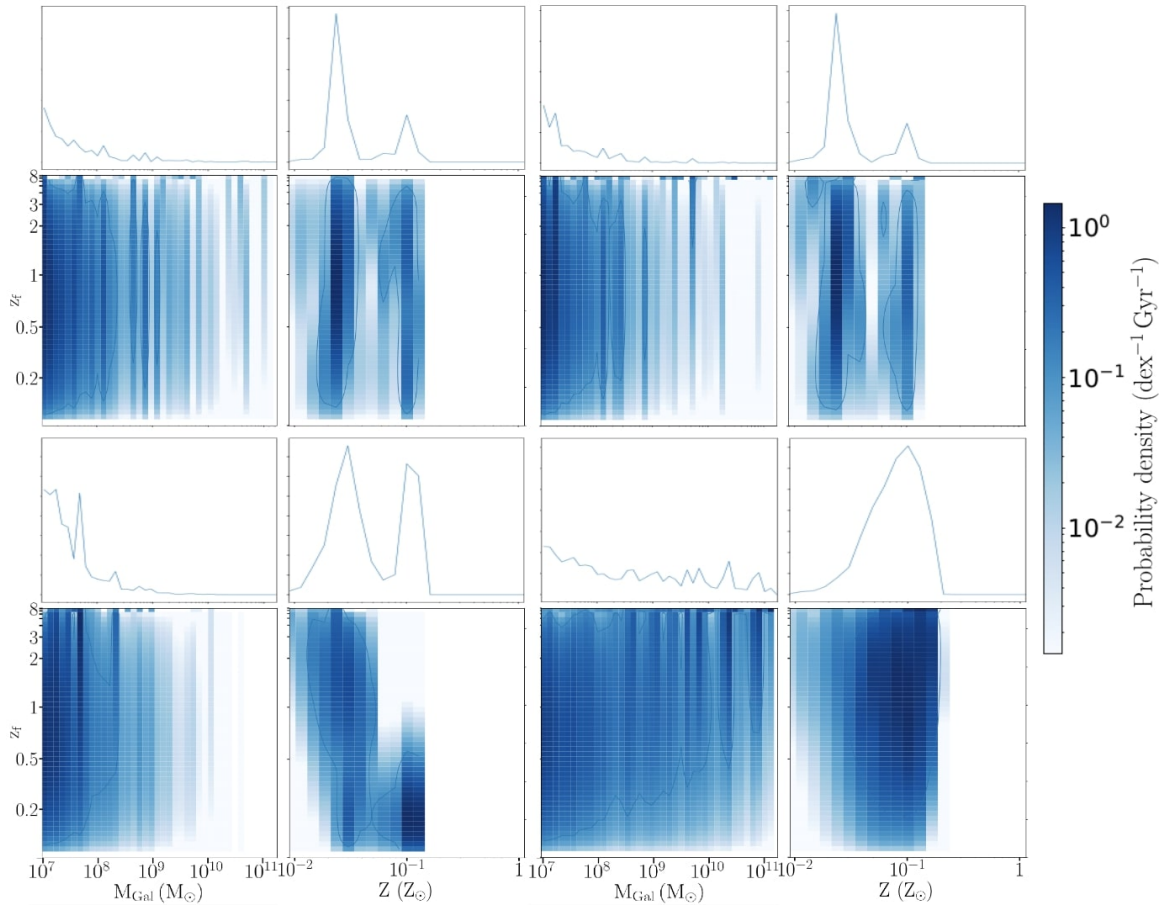

Figure 3.15: Comparison of the progenitor posterior of GW150914 for the KK04_Ma16 SFR/MZR and different BPS models: default (top-left), $M_{\mathrm{NS-BH}}(4)$ (top-right), $\alpha(0.2)\lambda(1)$ (bottom-left), and $q_{\mathrm{crit}}(4)$ (bottom-right). For each BPS model, I show the 1 and 2 dimensional posteriors in galaxy mass M_{Gal}, metallicity Z, and z_{f}.

It is important to test the robustness of the progenitor posteriors to different models. To this end, Figure 3.15 shows the progenitor posteriors for four models. Moreover, I represent the 2 dimensional posterior to show the correlation of $M_{\rm Gal}$ and Z with $z_{\rm f}$. It is interesting to see that all models are in agreement that the progenitor galaxy of GW150914 was a dwarf galaxy. In addition, although the relative probabilities of the bi-modal peak in metallicity varies between models (sometimes, collapsing into a single peak), the fact that the progenitors of GW150914 had low metallicity ($Z \lesssim 0.1$ Z$_\odot$) is invariant. These trends are also consistent with other models in my simulations.

The statistical method that I apply simply consists of re-weighting the typical galaxy properties from the simulation by the most credible black holes parameters of detected GW mBBHs. In the hypothesis that all the mBBHs detected are generated from processes described by my simulation, this method rapidly provides the most credible values for $M_{\rm Gal}$, Z, and $z_{\rm f}$ for a given event.

However, binary simulations are limited to black hole masses in the range of around 5-45 M$_\odot$, the upper mass limit is enforced by the PISN effect discussed in § 2.2.1. If a GW detection has posterior samples with black hole mass that falls outside this range, such a progenitor posterior cannot be generated from my current simulations and would require a different formation mechanism or channel (like dynamical interactions in dense environments) that can produce larger black holes. In the case that the formation channel is not known, or the detection rate and GW event are not consistent with my simulation, one should use a hierarchical inference approach (e.g. Bouffanais et al., 2021, Mastrogiovanni et al., 2022) considering other formation channels. In my analysis, I did not consider multiple formation channels but instead provided the most credible $M_{\rm Gal}$ and Z assuming that a particular GW event can be described with my simulation.

3.5 Uncertainties

3.5.1 Potential Sources

My star formation model builds on a global star formation rate based on Behroozi et al. [2013] and hence inherits the uncertainties it its estimation. My galaxy stellar mass function is based on Tomczak et al. [2014], which, as detailed in Chruslinska and Nelemans [2019], includes more low-mass galaxies than other models. As I show in Figure 3.5, these dwarf galaxies can be large contributors to the BBH merger rates. As such, the uncertainties on the number of low-mass galaxies, at all redshifts, are another important driver of uncertainties. Neijssel et al. [2019] showed that different galaxy mass functions can lead to a change in detected BBH merger rates up to a factor of five. Additional uncertainties stem from the exact initial conditions of the BPS models, such as the binary fraction and potential correlations between initial masses and orbital parameters (mentioned § 1.2.2). These

uncertainties can lead to an increase or decrease in the merger rate up to a factor of two.

BPS modeling is an ongoing field of research, with large uncertainties and oversimplification of complex mechanisms like the common envelope in unstable mass transfers and supernova kicks. We are severely limited by sparse observations due to the dynamic and transient nature of these mechanisms and defining a preferred model remains a challenge.

Dynamical environments are likely significantly contributing to the observed mergers as well [Wong et al., 2021, Bouffanais et al., 2021, Zevin et al., 2021, Mapelli, 2021b]. In dense clusters within galaxies, black holes can form successive binary mergers governed by N-body interactions that can lead to the formation of progressively larger black holes. The progenitor environments of dynamically formed mBBHs are clusters within large galaxies [Mapelli et al., 2022], unlike the typical dwarf galaxy progenitors of isolated mBBHs. A potential signature of the dynamical formation of black hole binaries is the spin orientation of the black holes. Black holes formed from isolated binary evolution will have aligned spins, whereas those formed through dynamic interactions in dense stellar environments will likely have random spins. Although, currently, more observations of mBBHs are required in order to confidently test the presence of misaligned spins among the detected mBBHs [Vitale et al., 2022]. The uncertainties on typical conditions of formation of clusters [e.g. Brodie and Strader, 2006] and the uncertainty on the associated merger rates add an additional layer of ambiguity to the inference of the typical formation conditions of mBBHs. In order to accurately predict the progenitor galaxies of mBBHs, it is necessary to incorporate this formation channel into the analysis.

3.5.2 Mitigation

Ultimately breaking the degeneracies between initial conditions (global star formation rate, metallicity evolution) and binary stellar evolution will require including additional information. First, one can limit the sample of explored models by only including those that have merger rates compatible with measurements. Then one can take this a few steps further by also including the information on the mass and possibly spin distributions. All of these will ultimately be measured as a function of redshift as detectors improve. With third-generation detectors like the Einstein Telescope [Maggiore et al., 2020] and Cosmic Explorer [Reitze et al., 2019] which are expected to detect sources up to a redshift of 15 to 20, the astrophysical and detected distributions will be very similar, removing the effects of detector biases from the analysis. Along the same lines, improved measurements of metallicity, star formation rates, and the galaxy stellar mass function, especially at high redshift will progressively decrease the allowed range for star formation models.

Still, degeneracies are likely to remain between star formation models and binary stellar evolution models. Joint modeling and observations of other types of transients associated with massive stars will be key. Neutron star mergers, and neutron star-black hole mergers to some extent, are much less dependent on stellar metallicity, and their merger rate more

directly traces the global star formation rate [Mapelli et al., 2018, Artale et al., 2020, Santoliquido et al., 2022].

As such, most of the differences arise due to the different assumptions on binary and stellar evolution. Eldridge et al. [2019] and Briel et al. [2022] showed population models of an ensemble of transients, including core-collapse supernovae, long gamma-ray bursts, and pair-instability supernovae, which are likely related to the same underlying population of massive stars. They show how transients of different delay times are sensitive to different uncertainties. Combined modeling of a range of phenomena seems to be the way forward when breaking degeneracies and ultimately determining likely progenitor environments.

Future research could extend the analysis to include massive black hole mergers as those formed for instance in active galactic nuclei and binary neutron star mergers. These sources have potential electromagnetic counterparts which can be used to test my estimation of the galaxy posterior. Such an analysis would entail BPS simulations of neutron star mergers and the simulation of dynamical black hole mergers in the dense environment of active galactic nuclei.

3.5.3 Applications of my simulations

In addition to Srinivasan et al. [2023], the astrophysical populations I simulated have also been used in Srinivasan et al [2023b] (in prep), Lehoucq et al. [2023], Mastrogiovanni et al. [2022]. In the latter two papers, as a co-author, I wrote the sections describing the BPS simulations. Lehoucq et al. [2023] studied the stochastic gravitational wave background produced by mBBHs and binary neutron stars in the frequency ranges of LIGO/Virgo/Kagra and the space-based GW detector LISA. For this purpose, Lehoucq et al. [2023] explored analytical and simulation-based population models. In order to establish a range of the background GW strain that are predicted by BPS simulations, we have used my default model and 2 other BPS models with the lowest and highest merger rates. Mastrogiovanni et al. [2022] have used a few populations of my common envelope models to demonstrate a method to implement synthetic catalogs for multi-channel hierarchical Bayesian inference and have quantified a match between the phenomenological reconstruction of merger rates with synthetic catalogs. Finally, in Srinivasan et al [2023b] (in prep), I use my default population to test and demonstrate a proof of concept of a ML-based GW detection pipeline. I elaborate on this project in Chapter 4.

Chapter 4

Towards a novel gravitational wave detection algorithm using machine learning

By the end of Chapter 3, I developed an astrophysical population of mBBHs in the Universe. A natural extension of my research is to work on the other side of the story: the detection of these sources. In this chapter, I detail my on-going project on developing a prototype algorithm to detect mBBHs using a machine learning (ML) algorithm, specifically ***sparse dictionary coding***. A distinguishing feature of this study is the use of my synthetic population of mergers ($Pop_{\rm Astro}$) that is based on observations and simulations, as opposed to a phenomenological model usually used in the development of pipelines.

Over the course of my research on understanding the progenitors of mBBHs, I identified my interest and ability to incorporate computer programming techniques into astrophysics. Building on my programming capabilities, I am interested in exploring the field of machine learning (ML) due to its growing importance in astrophysics and in general, all areas of research. The superior adaptability of ML techniques to parse complex problems without the need for complicated, problem-specific, user-defined algorithms makes ML an indispensable tool of research and engineering. However, applications of ML in astrophysics is arguably still in its early development stages, rich with scope for exploration, and therein lies its appeal to me as a researcher. To explore the use of ML in GW data processing, I initiated a project in collaboration with another doctoral student Charles Alexander Badger from King's College, London.

In this Chapter, § 4.1 provides an overview of existing detection techniques based on classical and ML algorithms. § 4.2 elaborates on the creation and evaluation of the sparse dictionary coding method. Finally, the ongoing and future developments are mentioned in § 4.3.

4.1 Introduction to ML and GW detection methods

Machine learning algorithms help statistical models to learn patterns, make predictions, and derive insights from data. These algorithms can be broadly categorized into three main types: supervised learning, unsupervised learning, and reinforcement learning. In the context of the algorithm explored in this thesis, I focus on supervised learning which involves training models on labeled data, where the algorithm learns the mapping between input features and corresponding output labels. The objective of supervised learning is to predict the output of new instances based on previously seen examples. In the context of GWs, the input feature is the detector data, and the output data can be any quantity that is to be determined, for example, the underlying GW signal.

The concepts of training and testing an algorithm is a vital phase governing the development and evaluation of a predictive statistical model. The training phase is a foundational process wherein a model reproduces patterns and relationships inherent in the provided dataset. This dataset used to train the model is aptly referred to as the training dataset. In my case of labeled data, the ML training algorithm attempts to minimize the disparity between the predicted and expected output that is encapsulated by a loss function. In this process, the model adjusts its parameters iteratively, thereby refining its ability to make predictions or classifications. Conversely, the testing phase serves as the litmus test for the model's efficacy and generalization to new, unseen data. This phase involves evaluating the model's performance on a separate dataset, distinct from the one used in training, to gauge its ability to accurately predict outcomes of data that it has not encountered before. The training and testing datasets must be disjoint to ensure the robustness of the model to real-world scenarios, avoiding overfitting to training data.

In this section, I elaborate on the typical algorithm of popular GW detection pipelines in § 4.1.1. Then, in § 4.1.2, I discuss current ML-based techniques for GW detection and in § 4.1.3 I introduce the principle behind the ML technique that we use in our algorithm.

4.1.1 The canonical GW detection algorithm

At the heart of compact binary coalescence (CBC) detection pipelines that ascertain the presence of a GW signal inside detector data is a match-filtering algorithm which I explain below. I shall focus on providing a simple explanation of the underlying principle used in Allen et al. [2012].

The CBC detection algorithm involves the calculation of the *match-filter SNR* ρ_{MF} between the detector data $s(t)$ and a collection of waveform templates $h(t)$. The template waveform is the projection of a GW onto the detector. The template banks built by the LVK are comprised of a large number of pre-generated waveforms whose parameters (masses) cover the parameter space of CBC sources. The match-filter SNR, ρ_{MF}, is defined as the

correlation between the data $s(t)$ and the template waveform $h(t)$ and is given by,

$$\rho_{\rm MF}(h) = \max_t \frac{|\langle \tilde{s}(f) \mid \tilde{h}(f) e^{i2\pi f t} \rangle_{\mathbb{C}}|}{\sqrt{\langle \tilde{h}(f) \mid \tilde{h}(f) \rangle}}, \tag{4.1}$$

where $\max_t$ is the maximization function that iterates over t and the corresponding t value that maximizes the correlation is the inferred time of coalescence. The subscript $\mathbb{C}$ extracts the complex value, and $\langle . \mid . \rangle$ is the noise-weighted inner product which "whitens" the signals and is defined as,

$$\langle h \mid g \rangle = \int_{-\infty}^{\infty} \frac{\tilde{h}(f)\tilde{g}^*(f) + \tilde{h}^*(f)\tilde{g}(f)}{S_n(f)} df, \tag{4.2}$$

where $S_n(f)$ is the one sided PSD defined in § 1.4 and $\tilde{h}^*$ is the complex conjugate of $\tilde{h}$. Iterating over the relevant templates, the pipeline identifies the one with the highest $\rho_{\rm MF}$ and designates that as the SNR of the given segment of the detector data $s(t)$. When $\rho_{\rm MF}$ exceeds a given threshold, a trigger of interest is defined in the dataset. In practice, in order to confidently identify the presence of GWs in triggers, the template search in a LVK detection pipeline defines a detection statistic based on $\rho_{\rm MF}$ that incorporates other consistency quantities to make it robust against non Gaussian features present in real GW data (see for instance, Usman et al., 2016).

In order to evaluate the chance of noise producing the observed SNR, and hence to establish confidence in a detection, one needs a model of the noise over an extended period. To this end, pipelines compute a false-alarm-rate (FAR), a useful detection metric used to asses the significance of a GW candidate.

4.1.2 Present ML-based detection algorithms

Most CBC detection pipelines use match filtering and with great success [Aubin et al., 2021, Usman et al., 2016, Messick et al., 2017]. Currently, the match filtering technique provides the best efficiency of detection among all existing methods. However, match filtering long segments of data can prove to be very computationally intensive and time-consuming. As an alternative, ML algorithms have been explored. Popular ML algorithms for GW signal processing [Cuoco et al., 2020] include the principle component analysis, deep learning, and decision trees. The deep neural network (DNN) architecture of deep learning have been shown to be useful for CBC searches among other applications (like noise subtraction and glitch detection) in GW data [George and Huerta, 2018, Schäfer et al., 2022, Schäfer et al., 2023, Schäfer, 2023], and even for detecting multi-messenger events like binary neutron star detection from both GW and EM counterparts [Baltus et al., 2022]. One of the strengths of deep networks is their ability to interpolate between waveform templates and to generalize to new classes of signals outside the template bank. Moreover, although teaching the network

can take time and computational resources, once trained, neural networks can potentially perform the detection analysis much faster than traditional algorithms.

The backbone of deep learning is the use of DNNs. In a typical deep learning based detection pipeline, the detector data undergoes a pre-processing step to extract the key features from the data that would provide the network with the optimal input to identify a GW signal, if present. For example, a pre-processing step usually adopted for unmodelled short signals is a Q-transform [Brown, 1991] which provides, as input features, the energy of the detector data as a function of frequency and time. The DNN itself is comprised of a series of convolutional neural networks and a fully connected network. The former is a neural network architecture that is best suited to extract features from image data (here, the energy-frequency-time plot) and the latter is used to classify the features (here, presence or absence of GW). Optionally, a post-processing step might involve parsing the output of the DNN into a probability or FAR of GW detection.

A supervised neural network requires data to train and to test its performance. In the context of neural network-based detection pipeline, the data is a collection of noise-only and noise + GW signal realizations. The term supervised implies that the user has access to the ground truth, i.e., the data is accurately labelled to denote the presence or absence of GW. The data is separated into two groups; one for training and the other for testing. During the training phase, the pipeline is shown examples of the data along with the ground truth in order to tune its system parameters to best predict the presence/absence of GW. The tuning of the neural network parameters is performed using the principle of gradient descent to locate the local minima of the loss function, a measure of the error between the prediction and ground truth. After training the pipeline, its performance is evaluated using a testing dataset. The pipeline is only fed the inputs of the testing dataset and its predicted output is compared with the corresponding ground truth. Depending on the specific ML algorithm one can introduce further steps such as repeated training-testing processes, performance confirmation with a validation dataset, and tuning system hyper-parameters (such as the number and size of the layers of a network).

Among ML-based detection pipelines, techniques like deep learning and decision trees have been explored. In this chapter, I investigate the potential of another ML algorithm called sparse dictionary coding.

4.1.3 Sparse dictionary coding

The sparse dictionary coding is a type of feature learning that aims to identify a sparse representation of the raw data as a linear combination of basis vectors called *atoms*. The collection of atoms comprise a *dictionary*.

Reconstructing the signal from data

I describe the adaptation of the sparse dictionary coding to GW data analysis based on the prescription of Torres-Forné et al. [2016]. This method solves the de-noising goal as a variational problem. Let $y = u + n$, where y is the detector data, u is the true signal, and n is the noise. A solution for u is given by

$$u_\lambda = \text{argmin}_\text{u} \left\{ \mathcal{R}(u) + \frac{\lambda}{2} \mathcal{F}(u) \right\}, \tag{4.3}$$

where $\mathcal{F}$ is a measure of the similarity between the predicted and expected values, $\mathcal{R}$ is a regularization term used to constrain the fitting parameters, and λ is a regularization parameter that controls the relative weight of $\mathcal{R}$.

The dictionary $\boldsymbol{D}$ is a matrix consisting of a series of column vectors called atoms. I designate the length and number of the atoms in a dictionary by w and p respectively. In theory, any GW signal can be represented by a linear combinations of the atoms of the dictionary. Therefore, there exists a sparse vector α such that $u \sim \boldsymbol{D}\alpha$. The similarity term $\mathcal{F}$ can then be defined as

$$\mathcal{F}(\alpha) = ||\boldsymbol{D}\alpha - y||^2, \tag{4.4}$$

where $||.||$ represents the L_2-norm, or Euclidean distance, of the vector defined as the square root of the sum of the squares of the vector components. Therefore, to solve Eq. (4.3), one needs to find the optimal sparse vector α that can best reconstruct the GW signal u using the dictionary. The regularization term is set as the L_1-norm, or Manhattan distance, of the sparse vector, i.e., $\mathcal{R} = |\alpha|$. Eq. (4.3) can be re-written as,

$$\alpha_\lambda = \text{argmin}_\alpha \left\{ |\alpha| + \frac{\lambda}{2} ||\boldsymbol{D}\alpha - y||^2 \right\}, \tag{4.5}$$

known as “least absolute shrinkage and selection operator" (LASSO) [Tibshirani, 1996] or basis pursuit [Chen et al., 2001]. Using the optimal sparse vector α_λ from Eq. (4.5), the reconstructed signal ("best guess") of the dictionary is $\boldsymbol{D}\alpha_\lambda$. One can solve for the basis pursuit by using the Alternating Direction Method of Multipliers (ADMM) algorithm from Boyd et al. [2011]. Taking, as input, the detector data y, the ADMM algorithm produces the first reconstruction $\boldsymbol{D}\alpha$. A residual is defined as the difference between the input, y, and the reconstruction. The residual is then fed back into the ADMM algorithm as the new input and the process repeats. At each iteration, the new residual is equal to the input subtracted by the current reconstruction. Theoretically, with subsequent iterations, more signal is subtracted from the data until the residual eventually converges to the underlying noise. This convergence is evaluated by the norm of the residual. When the norm falls below a specified tolerance, the algorithm stops. The reconstructed signal is the sum of the reconstructions from all iterations.

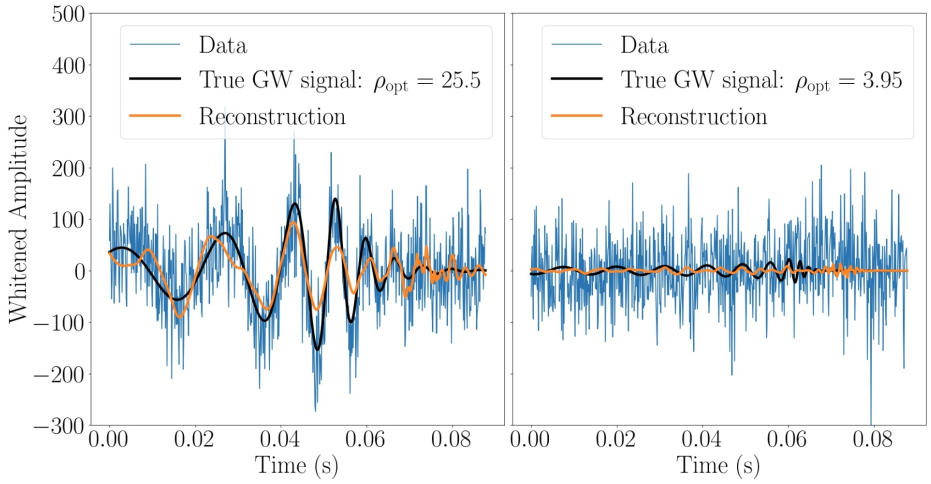

Figure 4.1: Examples of signal reconstruction (orange curve) using a trained dictionary for a given detector data (blue curve). The ground-truth GW signal (black curve) present in the detector data is shown for comparison. In the two panels, I illustrate the reconstructions for different optimal SNRs $\rho_{\rm opt}$ (shown in legend).

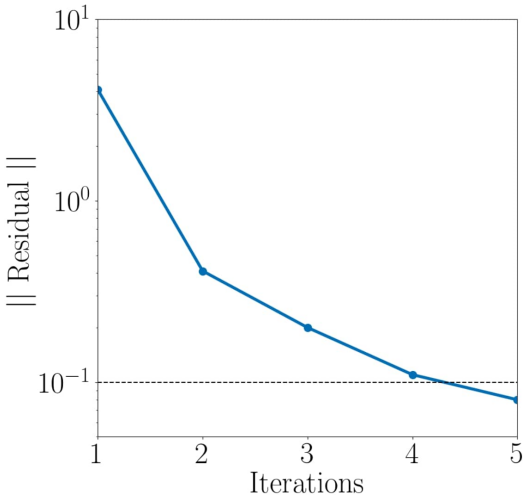

Figure 4.2: Illustrating the convergence of the reconstruction: evolution of the norm of the residual (blue curve) from successive iterations of the ADMM algorithm to evaluate Eq. (4.5). The residual is defined as the current reconstruction subtracted from the previous residual. The initial residual is set as the data itself. When the norm of the residual falls below 0.1 (dotted black line), the algorithm terminates and returns the sum of the reconstructions from all iterations.

I illustrate an example of the reconstruction of a signal in Figure 4.1. I show the reconstructions of CBC signal (70-70 $M_\odot$ system at different distances) embedded in noise using a trained dictionary for two values of the signal optimal SNR $\rho_{\rm opt}$. The GW with the higher $\rho_{\rm opt}$ is better reconstructed. Elaborating further, the low SNR signal is dominated by noise. As the noise is uncorrelated with GWs, and because the dictionary is trained to reconstruct GW signals, the fidelity term in Eq. (4.5) cannot be minimized for any value of α. Hence, only the regularization term $|\alpha|$ can be minimized. As a consequence, α tends towards the null vector and the reconstruction ($\boldsymbol{D}\alpha$) approaches a time-series of nearly zero amplitude. In terms of the ADMM algorithm, the residual soon falls below the tolerance threshold and the returned reconstruction have small amplitudes.

The reconstruction also shows erroneous non-zero values after the true merger time, especially in the case for high $\rho_{\rm opt}$. This follows from the fact that when the algorithm reconstructs the signal in the high-frequency merger regime, it is also susceptible to the high frequency noise fluctuations shortly afterwards.

Figure 4.2 illustrates the evolution of the norm of the residual which is used to check for the convergence of the ADMM algorithm to solve Eq.(4.5). The norm shows a converging trend until falling below the defined threshold (here, 0.1). Thus, after five iterations of the ADMM algorithm, the reconstruction is over.

Note that different values of $\boldsymbol{D}$ and λ can result in different reconstructions. To obtain the best reconstruction, one must optimize the hyper-parameters of the algorithm (w, p, and λ) and the values of the dictionary itself (i.e., the atoms) by comparing the reconstruction $\boldsymbol{D}\alpha_\lambda$ with the ground truth GW signal u.

Training the dictionary

Eq. (4.5) assumes that the best values of the dictionary has already been identified (for instance, as a set of wavelets) and can be used to reconstruct any GW signal. Significant improvement can be achieved by training the dictionary [Elad and Aharon, 2006] on the CBC waveform. The training dataset is comprised of a set of GW signal realizations. No noise is added. Each training signal is segmented into overlapping patches, each of length w (i.e., equal to the atom lengths). The total number of patches in the training dataset m depends on the number of training signals, patch length w, and the number of overlapping samples between consecutive patches. Following Torres-Forné et al. [2016] and Mairal et al. [2009], the dictionary is trained by recursively evaluating α and $\boldsymbol{D}$ by the equations

$$\alpha^{k+1} = \text{argmin}_\alpha \left\{ \frac{1}{w} \sum_{i=1}^{m} ||\boldsymbol{D}^k \alpha_i - u_i||^2 + \lambda |\alpha_i| \right\} \tag{4.6}$$

$$\boldsymbol{D}^{k+1} = \text{argmin}_{\boldsymbol{D}} \left\{ \frac{1}{w} \sum_{i=1}^{m} ||\boldsymbol{D}\alpha_i^{k+1} - u_i||^2 + \lambda |\alpha_i| \right\}, \tag{4.7}$$

where the superscript k identifies the training iteration and the subscript i indicates the index of the training data patch. In comparison to Eq. (4.5), the above two equations have replaced y with u because the training data is devoid of noise. Eq. (4.6) and Eq. (4.7) are repeatedly calculated until the dictionary converges, at which point training is complete. In practice, both Mairal et al. [2009] and Torres-Forné et al. [2016] have empirically found that a single iteration of this step is sufficient for convergence (see Goldstein and Osher, 2009 for detailed discussion). Note that the aim of the training is to learn and fix the values of the dictionary $\boldsymbol{D}$, and not the sparse vector α. The latter is used to produce the signal reconstruction for a given data and a given dictionary $\boldsymbol{D}$.

4.2 Methods: designing and evaluating a dictionary

We are interested in exploring the use of dictionaries to detect stellar-mass black hole binaries with a total mass between 10 and 200 $M_\odot$ from GW detectors (LIGO Hanford, LIGO Livingston, Virgo, and KAGRA) during the planned 5th observing run, O5 [Abbott et al., 2018]. To explore the detection of GWs from merging binary black holes (mBBHs) using sparse dictionary coding, we train two competing dictionaries, establish the detection statistics, evaluate their performances with simulated data, and select the best dictionary. We build upon the dictionary training procedure discussed in Torres-Forné et al. [2016, 2020] and Badger et al. [2023]. All plots in this chapter are made using dictionaries trained on the LIGO-Hanford detector data.

In this section, Charlie produced the noise and training dataset. I produced the testing dataset. Charlie trained the dictionaries with the training dataset, and produced signal reconstructions for the noise and testing datasets. I identified the detection metrics, produced the detection statistic, and evaluated the performance of the dictionaries and metrics. The following subsections describe the procedure in detail.

§ 4.2.1 details the procedure to generate the datasets to train and evaluate the dictionaries. In § 4.2.2, I establish the detection metrics I explore. Then, in § 4.2.3 I discuss our choice of dictionary hyper-parameters (size of atoms, number of atoms, regularization parameter) that we explore. Finally, in § 4.2.4, I evaluate the performance of the two dictionaries.

4.2.1 Data generation

The dictionary takes as input, whitened detector data, and returns a reconstruction of the underlying whitened GW signal, if any. We focus on analyzing the merger phase as it contains a significant portion of the GW SNR, especially for heavier black holes. The sampling frequency and duration of the data that is passed into the dictionary is determined by the trade-off between the computational load of processing large time-series and the duration of the mBBH in the detector bandwidth (with a lower frequency of 10Hz). We

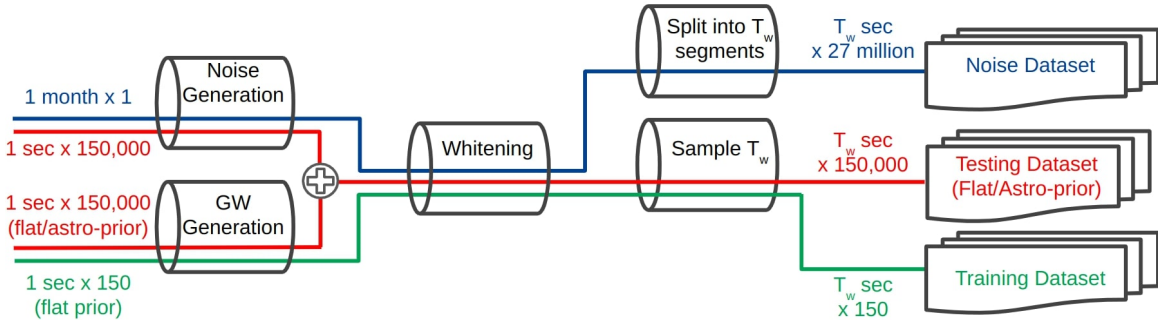

Figure 4.3: Flowchart illustrating the procedures involved in generating the noise, training, and testing datasets. The size of the data are written in text in the format *duration of each realization* × *number of such realizations*.

fix the sampling frequency f_s to 8192 Hz. This sets the Nyquist frequency, the highest frequency that the system can theoretical reproduce, to 4092 Hz which is higher than the merger frequency of all stellar-mass mBBH systems. The duration of the time-series $T_{\rm w}$ is derived by the relation $T_{\rm w} = N_s/f_s$, where N_s is the number of samples considered. Typically, the number of samples is set to powers of 2 [Torres-Forné et al., 2016]. Having a small $T_{\rm w}$ we run the risk of not capturing the pre-merger and merger phases of high mass black holes because the duration of these phases decreases with increasing mBBH mass. Whereas, increasing $T_{\rm w}$, and hence the number of samples, increases the computational complexity. The interplay between the two is such that $N_s = 512$ is too short for heavy mBBHs, whereas, $N_s = 1024$ is computationally prohibitive. As a compromise, we set $N_s = 720$. This sets $T_{\rm w}$ to 0.08789 s which is optimally short for computation and also long enough to accommodate the pre-merger and merger phase of all stellar-mass black holes.

GW detector noise contain different power at different frequencies as given by the PSD. The process of whitening normalizes the power at all frequencies so that excess power at any frequency is more obvious. Therefore, the data provided to the dictionary is always whitened. To whiten a given time-series, we take its Fourier transform, divide it by the square-root of the PSD, and take its inverse Fourier transform. To account for edge-effects from the whitening procedure, we discard the first and last 0.1 s of the whitened data.

In the paragraphs below, I detail the procedure to produce the datasets for training, testing, and noise analysis for a dictionary of a given detector. The flowchart of Figure 4.3 also illustrates these steps.

Noise dataset

The noise dataset is comprised of whitened noise realizations. It is used to produce a distribution of the detection statistic for data that is devoid of GW signal. To generate noise realizations, we use the PSDs of the LVK's future fifth observing run O5. The size of the

dataset is limited by the time taken to generate the noise. For each detector, one month-long duration of noise in half-day chunks is produced. All chunks are whitened in parallel to improve computational efficiency. Month-long noise is split in segments of duration T_w s. The steps involved in generating the noise dataset are shown by the blue lines of Figure 4.3.

Training dataset

The dictionary is trained with whitened GW signals. Badger et al. [2023] use 100 training signals to model their dictionary on GW signals in the data of the future space-based interferometer LISA. Due to differences in the population analyzed, our dictionary performs better with more training signals. However, the size of the training set is limited by the time required to train. Moreover, the dictionary shows diminishing improvement in the reconstruction when the number of training signals increases beyond 150. Hence, optimized for computational efficiency, the training dataset is comprised of 150 whitened, GW signals. These GW signals are generated from a population of mBBHs with a uniform distribution of primary black hole mass (5 to 100 $M_\odot$), mass-ratio (1 to 3), luminosity distance (10 to 10^4 Mpc), sky-position angles, and inclination of non-spinning black holes. The coalescence time and phase of the GW is also sampled from a flat distribution.

For each mBBH system in the training dataset, the GW strain data in each detector is generated using the IMRPhenomD waveform approximant [Khan et al., 2016]. One second of the waveform containing the end of the coalescence is sampled. The signal is then whitened. Finally, a segment of duration T_w containing the merger is sampled from the whitened signal. In order to ensure at least 70% of the segment is occupied by the pre-merger + merger phases, the merger is aligned at about 0.7 T_w. The collection of such segments for the above-defined set of 150 GW signals makes up the training dataset. The steps described is illustrated by the green lines in Figure 4.3. Note that we whiten 1 s of data (8192 samples) and then sample T_w s, instead of directly whitening T_w s (720 samples), because of the improved robustness of whitening with the increasing number of samples.

Testing dataset

The testing dataset is divided in two categories: the flat-prior dataset, and the astrophysical dataset. The former is used to evaluate the performance of the dictionary and to identify the detection biases it entails. It is comprised of 150,000 noise+GW data that I generate with flat-priors on the GW signal (similar to the training signals) for all parameters but the masses. To investigate the performance of the dictionary for different black hole masses and mass ratio, I set the black hole mass to have five equally probable configurations: 5-5, 10-10, 40-40, 70-70, and 80-20 $M_\odot$. Note that the training dataset only contains a maximum mass ratio of three. As remarked earlier, one of the key features of ML-based detection pipelines is its ability to generalize to a new class of waveforms beyond its trained

template bank. Therefore, I include the 80-20 $M_\odot$ system with a mass ratio of four to test the performance of the algorithm for systems outside its training population. I produce the astrophysical testing dataset by sampling from my simulation of the default astrophysical population $Pop_{\rm Astro}$ to simulate a detection period of one year. I plan to use this dataset to infer about the subset of the astrophysical population that is detectable by our dictionary. It is important to note that the training and the flat-prior testing datasets are produced with the same CBC priors (except for the 80-20 $M_\odot$, high mass-ratio system). It is therefore imperative to check whether the algorithm is over-trained using the astrophysical testing dataset.

For a given mBBH system in the testing dataset, I generate the corresponding GW signal of duration 1 s, with the merger time at 0.7 s. To this, I add 1 s of simulated coloured-noise. Thereafter, the steps are identical to those involved in producing the training dataset. For the current goal of establishing a proof-of-concept of the algorithm, we fix the merger time to 0.7 T_w. In future analysis, we must explore reconstructions with the merger at random times in the window. The procedure for generating the testing dataset is shown by the red lines of Figure 4.3.

4.2.2 Detection metrics

A detection metric is a quantity that can distinguish the presence and absence of GW signal in data. The dictionary algorithm produces a reconstructed waveform for a given detector data. Following the idea of the match filtering technique, I explore metrics involving the correlation of the detector data and the dictionary's reconstruction. Specifically, the overlap and match-SNR of the data and reconstruction. The overlap O is defined as follows,

$$O = \frac{\langle \tilde{s}(f) \mid \tilde{h_r}(f) \rangle}{\sqrt{\langle \tilde{s}(f) \mid \tilde{s}(f) \rangle \langle \tilde{h_r}(f) \mid \tilde{h_r}(f) \rangle}}, \tag{4.8}$$

where s represents the detector data, h_r is the dictionary's reconstruction, and $\langle . \mid . \rangle$ is the noise-weighted inner product defined in Eq. (4.2). Similar to the match-filter SNR of Eq. (4.1), the second metric, match SNR $\rho_{\mathcal{M}}$, is defined as

$$\rho_{\mathcal{M}} = \frac{\langle \tilde{s}(f) \mid \tilde{h_r}(f) \rangle}{\sqrt{\langle \tilde{h_r}(f) \mid \tilde{h_r}(f) \rangle}}, \tag{4.9}$$

which is related to the overlap by a factor $\sqrt{\langle \tilde{s}(f) \mid \tilde{s}(f) \rangle}$, which quantifies the energy of the time-series data. The overlap is a normalized quantity, with a range of 0 to 1. The match SNR, in contrast, increases with increasing GW signal amplitude and can have any value greater than 0.

4.2.3 Dictionary hyper-parameters explored

The sparse coding algorithm is defined by its hyper-parameters: atom length (or column size) w, number of atoms (or row size) p, and the regularization parameter λ. Note that the atom length w cannot be greater than the length of the input data (i.e., $w <= 720$).

As we are only interested in providing a proof of concept for a dictionary-based GW-detection algorithm, we do not perform an extensive search for the best set of hyper-parameters. Based on an empirical evaluation of the reconstructions, we observed no clear trends in the performance of the dictionaries for different w and p. Moreover, Torres-Forné et al. [2020] have remarked that the number of atoms does not show variation in performance as long as the dictionary is over-completed (i.e., $p > w$). Following the procedure in [Torres-Forné et al., 2020, Badger et al., 2023], we explore an atom length that is a power of two, $w = 512$. We also chose to explore the case of maximum atom length, i.e., $w = 720$. Following the convention in Badger et al. [2023], we also set $p = 1.5 \times w$.

The hyper-parameter λ controls the "step-size" of the basis pursuit algorithm described in Eq. (4.5), typically taking a value between 0.1-0.0001. As λ decreases, the time taken to train the dictionary and to produce reconstructions increases. The desired value of λ is one that produces a dictionary that demands a low computational load and produces reconstructions that are highly correlated with the underlying true GW signal. For the two dictionaries, we empirically find that $\lambda = 0.0001$ is a good trade-off between computational efficiency and high fidelity reconstructions.

In summary, we chose to explore the performance of dictionaries with hyper-parameters $w = 512$, $p = 768$, $\lambda = 0.0001$ and $w = 720$, $p = 1080$, $\lambda = 0.0001$. For ease of notation, I hereon refer to the former by $\boldsymbol{D}_{512}$ and latter by $\boldsymbol{D}_{720}$. I describe a detailed study on the efficiency of detection for both dictionaries in the following section.

4.2.4 Detection statistics and dictionary evaluation

To compare the two detection metrics ($\mathcal{O}$, $\rho_{\mathcal{M}}$) and to analyze the detection efficiency of the competing dictionaries ($\boldsymbol{D}_{720}$, $\boldsymbol{D}_{512}$), I compute the detection statistics and evaluate the performance of the two dictionaries using reconstructions of the noise and the flat-prior testing datasets.

Evaluating the detection metric

Figure 4.4 shows the probability density function of the detection metrics for $\boldsymbol{D}_{720}$ and $\boldsymbol{D}_{512}$ for the noise and testing datasets. I also show sub-sets of the testing dataset with different optimal SNR ρ_{opt}. $\boldsymbol{D}_{512}$ generally produces higher values of $\mathcal{O}$ and $\rho_{\mathcal{M}}$ in comparison to $\boldsymbol{D}_{720}$ for both datasets. Moreover, in comparison to $\boldsymbol{D}_{720}$, the detection statistic of $\boldsymbol{D}_{512}$ shows slightly greater overlap between noise and signal, especially for signals with low

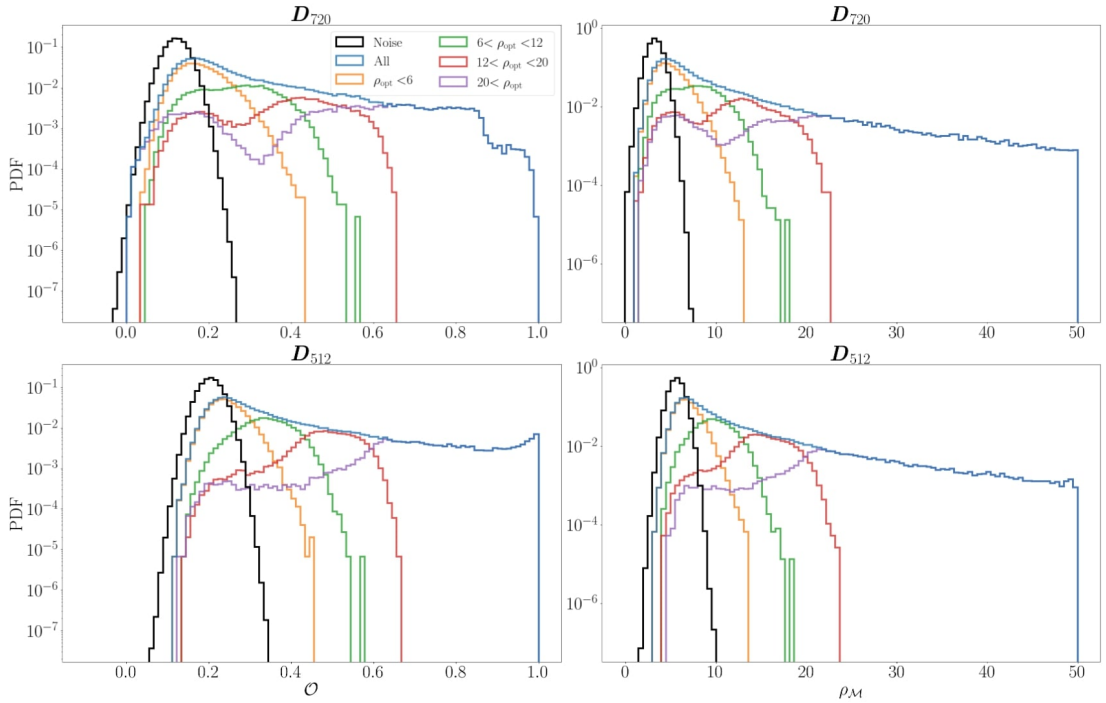

Figure 4.4: Probability density function (PDF) of the detection metrics, overlap $\mathcal{O}$ (left) and match SNR $\rho_{\mathcal{M}}$ (right), for the two dictionaries, $\boldsymbol{D}_{720}$ (top) and $\boldsymbol{D}_{512}$ (bottom). The figures show the results for 28 million noise realizations totalling to one-month of data (black curve) and 150,000 testing data comprised of GW + noise (blue curve). The PDF for the subset of testing data with different ranges of the optimal SNR $\rho_{\rm opt}$ is also shown (see legend). For clarity, I limit the maximum value of $\rho_{\mathcal{M}}$ in the figure to 50.

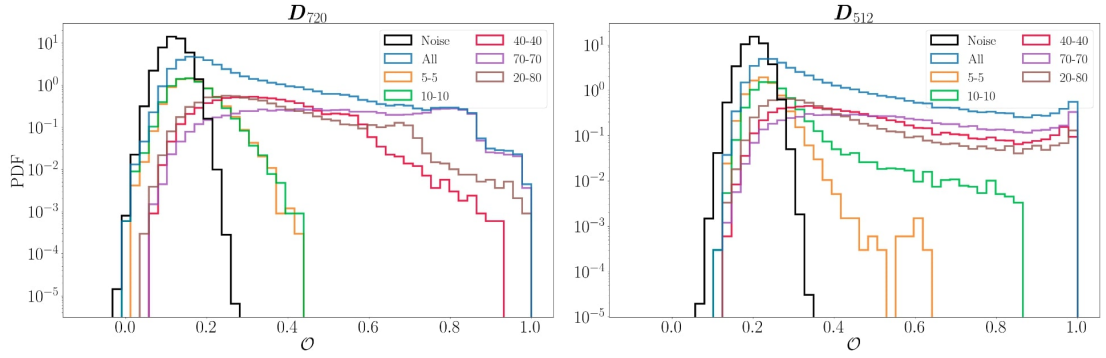

Figure 4.5: Probability density function (PDF) of the overlap $\mathcal{O}$ for the two dictionaries $\boldsymbol{D}_{720}$ (left) and $\boldsymbol{D}_{512}$ (right) for different mass systems in the testing dataset (see legend). For comparison, I show the one-month of noise-only data (black curve) and all 150,000 of the testing data (blue curve).

optimal SNR. For $\rho_{\rm opt} > 12$, both dictionaries have O and $\rho_{\mathcal{M}}$ values that are mostly larger than the noise statistic. This indicates that the chosen metrics perform well and show promise towards classifying signal and noise.

For $\boldsymbol{D}_{720}$, there is a bi-modal distribution in high SNR signals ($\rho_{\rm opt} > 12$). In the case of $\boldsymbol{D}_{512}$, instead of a bi-modal distribution, there appears to be one major peak at high metric values and a flattened distribution for lower metric values. Figure 4.5 shows that these effects are due to the different detection statistics for different mass ranges for the two dictionaries. Specifically, the 5-5 $M_\odot$ and 10-10 $M_\odot$ systems contribute to the peak in the probability density function at lower values of the metric and more massive systems contribute to the peak at higher metric values. Moreover, Figure 4.5 also shows that this effect is less pronounced for $\boldsymbol{D}_{512}$ as evident by the relatively flatter distribution for low mass systems in comparison to that for $\boldsymbol{D}_{720}$. These results indicate that in addition to the SNR, the dictionaries are sensitive to the masses of the black holes.

False-alarm-rate

To quantify the confidence of detecting a signal, I define the false-alarm-rate (FAR) of a given metric as the ratio of the number of noise realizations from the noise dataset which surpass the metric threshold, divided by the total time of noise-data analysed. I calculate the FAR distribution for the two dictionaries, and for each metric. Figure 4.6 shows the FAR as a function of the detection statistic O and $\rho_{\mathcal{M}}$ for the two dictionaries. The figure shows, for example, the number of realizations (of duration $T_{\rm w}$) in the one month of noise data which have $O \gtrsim 0.25$ is $\simeq 100$ for $\boldsymbol{D}_{720}$ and nearly 10 million for $\boldsymbol{D}_{512}$. Thus, the FAR of the dictionaries at $O = 0.25$ is about 100/yr and 10^7/yr respectively.

The minimum value of the FAR from the noise dataset is 12/yr (or 1/month). As shown in Figure 4.4, the testing dataset have a large fraction of signals with metric values greater than the noise distribution. Therefore, it is important to probe lower FARs for which I lack noise data. One solution is to simulate more noise realizations. However, this is a very time consuming task. Moreover, the FARs we would need to probe (up to one in several thousands of years for a 5σ discovery) require over four orders of magnitude of more noise data. Instead, I extrapolate the relation between the FAR and the detection metric. Specifically, I use a cubic polynomial fit of the $\log_{10}$ FAR as a function of the metric. Other extrapolation fits such as a power-law multiplied by an exponential can also be used. However, the root-mean-squared error between the fit and the data is the least for a simple polynomial fit. Future iterations of the extrapolation should include the statistical error of the data, such that the error scales inversely with the number of noise realizations surpassing the metric. In Figure 4.6, I illustrate the agreement between the fit function and the data, and also show the extrapolation to lower FAR values.

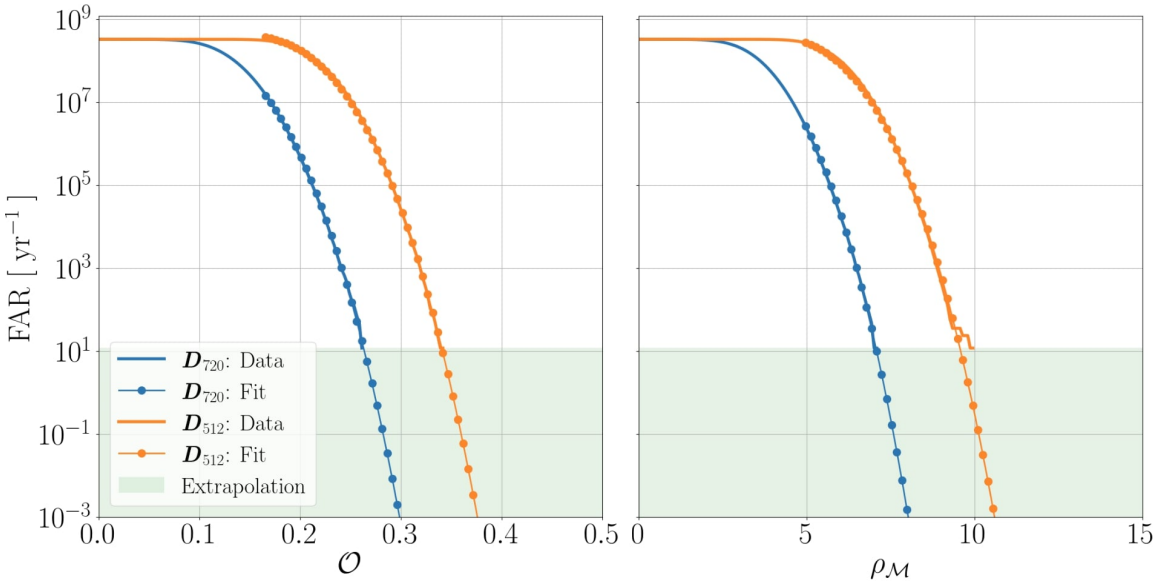

Figure 4.6: The false-alarm-rate (FAR) of the detection metrics: overlap $\mathcal{O}$ (left) and match SNR $\rho_{\mathcal{M}}$ (right), for the two dictionaries $\boldsymbol{D}_{720}$ (blue curves) and $\boldsymbol{D}_{512}$ (orange curves). As our current simulations only have one month of simulated noise data to analyze, the lowest FAR probed with data is 12/yr (or 1/month). The noise simulation of one month is shown by the lines without markers, above the green shaded region. I extrapolate the FAR to higher values of the detection metric using a cubic polynomial fit of the $\log_{10}$ FAR versus the metric. The fit is shown by the lines with circle markers and the region extrapolated is highlighted by the green shading.

Receiver operating characteristics

In order to evaluate the performance of the competing dictionaries and metrics, I analyze their receiver operating characteristic (ROC) curves. In this context, the ROC curve is a graph of the true positive rate of GW detection versus the false alarm rate for a given detection metric. The true positive rate is the fraction of all testing signals that are detected i.e., that surpass the metric threshold. When comparing ROC curves, the curve with greater true positive rate for a given FAR represents a better classifier of signal from noise and is hence more desirable.

Figure 4.7 shows that irrespective of the dictionary, $\rho_{\mathcal{M}}$ is the superior detection metric. This is understandable because although both metrics compute the correlation between the reconstruction and input data, $\rho_{\mathcal{M}}$ also takes into account the energy of the data (as remarked in the discussion of Eq. (4.9)). Hence signals with large SNRs are easier to distinguish using $\rho_{\mathcal{M}}$. It is also interesting to note that as the FAR increases, the difference between the performance of the metrics decreases. Signals with low SNRs tend to have higher FARs because they are often confused with noise. As a result, the extra information in $\rho_{\mathcal{M}}$ regarding the energy of the low SNR (high FAR) data is not as significant, causing the disparity between $\rho_{\mathcal{M}}$ and $\mathcal{O}$ to decrease.

Figure 4.7 shows that the two dictionaries have nearly identical performance as seen by the large overlap in the detection efficiency, especially considering the deviations from the FAR estimate. This is consistent with our analysis of different dictionary hyper-parameters in § 4.2.3. Due to this similarity, either dictionary can be chosen for future analysis. Although not perfect, the extrapolation does provide a rough estimate of the efficiency of detection for low FARs. The extrapolation continues the trend and shows that over 35% of the flat-prior testing dataset is detected with an FAR less than one per thousand years, indicating that the algorithm shows promise.

The ROC graph can also be used to understand the detection biases of the dictionary method. Figure 4.8 shows the ROC curves of the dictionaries for different signal SNRs ρ_{opt} (left) and black hole masses (right). The true positive rate is normalized to each sub-population specified in the legend. Looking at the left column, the performance of the dictionaries improves with greater signal SNR, i.e., for a given FAR, signals with a greater SNR have a higher rate of detection. It is encouraging to see that for $\rho_{\text{opt}} > 12$, the algorithm is able to detect 80% (for $\boldsymbol{D}_{720}$) and 90% (for $\boldsymbol{D}_{512}$) of the signals with an FAR < 1/month. Only the ROC curve for $\rho_{\text{opt}} > 6$ (orange) falls below the global ROC curve (blue) further highlighting that the dictionaries struggles to reconstruct low SNR signals. As the SNR depends primarily on the distance of the merger, this indicates a detection bias of the dictionaries towards nearby systems. Interestingly, the $\boldsymbol{D}_{512}$ outperforms $\boldsymbol{D}_{720}$ for signals with high SNR ($\rho_{\text{opt}} > 12$), whereas for lower SNRs, $\boldsymbol{D}_{720}$ has a higher efficiency.

The right column of Figure 4.8 shows the ROC curve for different dictionaries and black hole masses. In both dictionaries, low mass systems (5-5 $M_\odot$ and 10-10 $M_\odot$) have

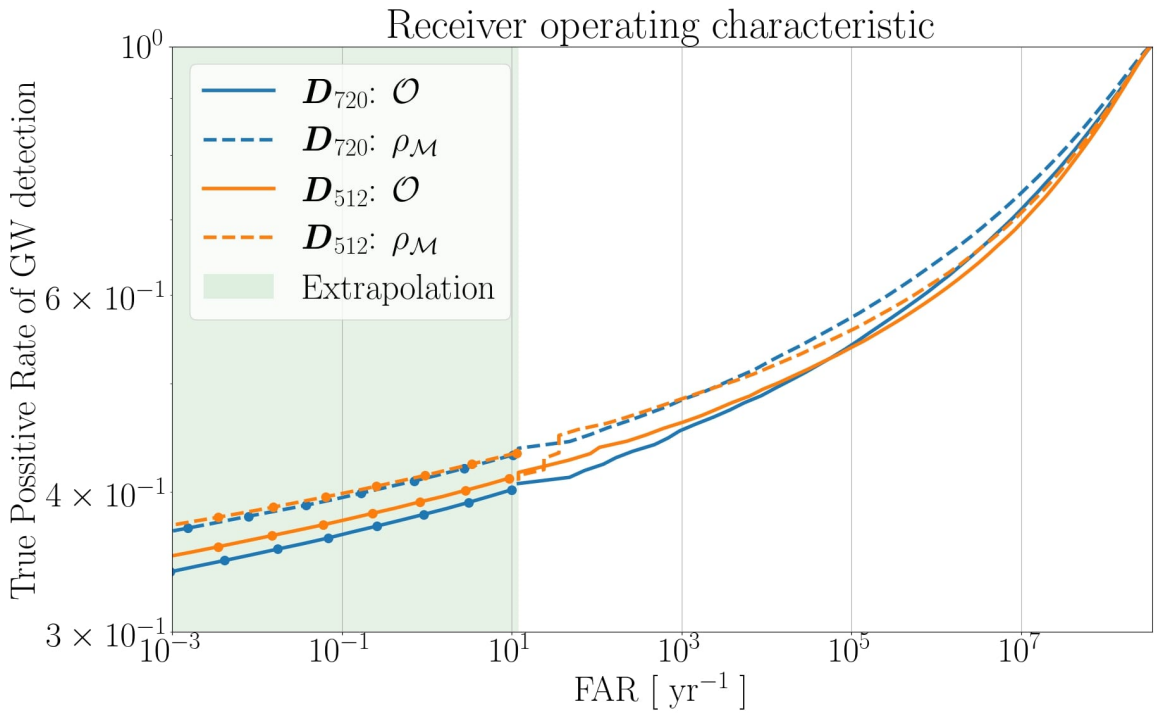

Figure 4.7: Receiver operating characteristic (ROC) curve describing the true positive rate as a function of the false-alarm-rate (FAR) of the $\boldsymbol{D}_{720}$ (orange) and $\boldsymbol{D}_{512}$ (blue) dictionaries, and for different detection metrics overlap $\mathcal{O}$ (solid curve) and match SNR $\rho_{\mathcal{M}}$ (dashed curve). These ROC curves are produced for the flat-prior testing dataset. The portion of the ROC curve produced using the extrapolated values of the FAR is shaded in green.

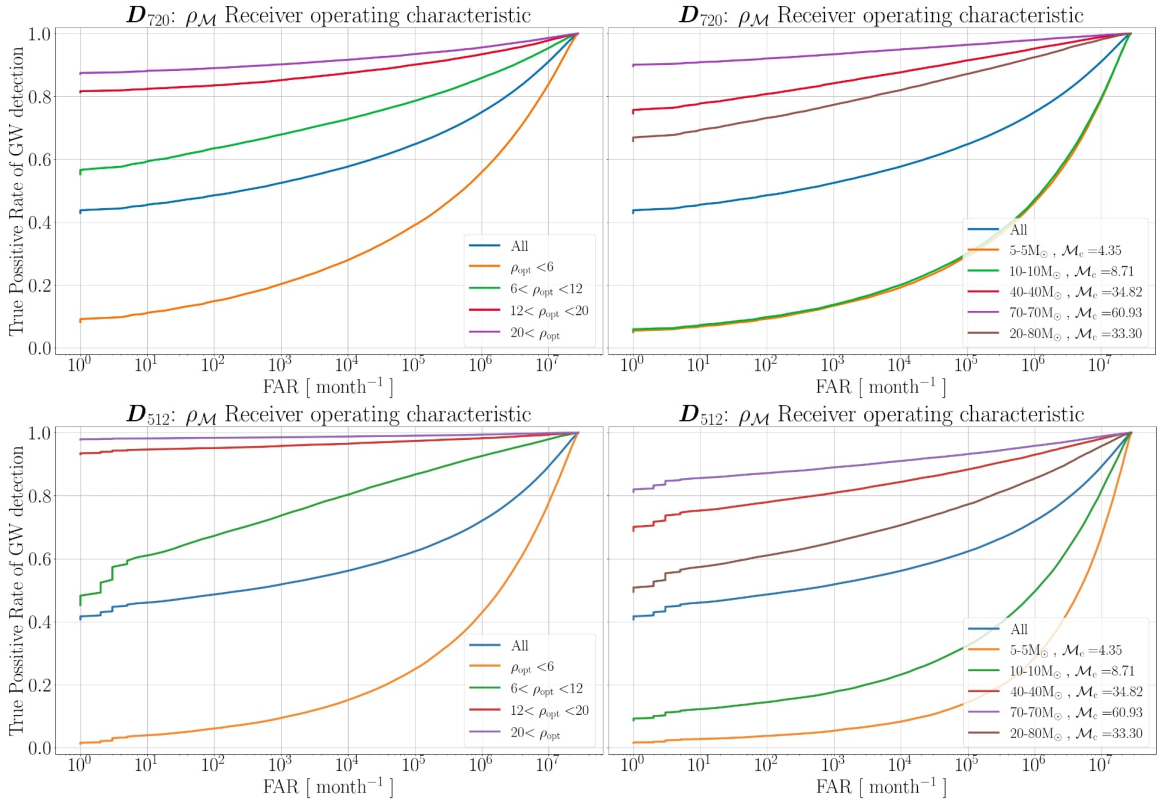

Figure 4.8: Receiver operating characteristic (ROC) curve of the $\boldsymbol{D}_{720}$ (top), $\boldsymbol{D}_{720}$ (bottom) dictionaries using the match SNR $\rho_{\mathcal{M}}$ metric for different ranges of the testing signal's optimal SNR (left, see legend) and black hole masses (right, see legend). The ROC curves for all test signals combined is shown in blue. Note that I show the results without extrapolation and show FAR in units of month^{-1}.

worse detection rates. This can be attributed to the low SNRs due to the lower chirp mass $\mathcal{M}_c$ (see legend) of these mBBHs in comparison to the other massive systems. Thus indicating a detection bias in the dictionaries towards systems with higher chirp mass (CBC signal amplitude scales with $\mathcal{M}_c^{5/3}$). This is consistent with the discussion from Figure 4.5 regarding the lower values of the detection metric for low (chirp) mass systems in comparison to high (chirp) mass systems. $\boldsymbol{D}_{720}$ outperforms $\boldsymbol{D}_{512}$ for all system masses except for the 10-10 $M_\odot$ system. Torres-Forné et al. [2020] have remarked that dictionaries with smaller atom lengths are more sensitive to higher frequencies. As the merger frequency increases with decreasing black hole masses, this could potentially explain the better performance of $\boldsymbol{D}_{512}$ over $\boldsymbol{D}_{720}$ for the low mass 10-10 $M_\odot$ systems. However, in the case of the even lower mass 5-5 $M_\odot$ systems, although the merger frequency is high, the effect of the low SNR due to the smaller chirp mass plays a bigger role. Moreover, the fraction of $\rho_{\rm opt}$ inside the $T_{\rm w}$ window is lesser for 5-5 $M_\odot$ systems in comparison to that of 10-10 $M_\odot$ systems indicating that we must lose a larger fraction of the 5-5 $M_\odot$ signal. And as remarked by the above discussion on $\rho_{\rm opt}$, $\boldsymbol{D}_{720}$ outperforms $\boldsymbol{D}_{512}$ for low SNR events.

The brown curve of the 80-20 $M_\odot$ systems shows that high mass ratio systems can be detected by both dictionaries. As mentioned before, this high mass-ratio falls outside the training population (which have mass-ratio $\lesssim 3$). Thus, it is encouraging to see that the dictionaries are able to detect systems outside their trained population. Comparing the 80-20 $M_\odot$ and 40-40 $M_\odot$ systems, the latter has a consistently higher efficiency, even though both systems have nearly identical chirp masses. This could be due to the absence of the high mass-ratio systems in the training, or can potentially indicate a bias against unequal mass ratio. To investigate further, I am currently probing the performance of the dictionary for lower mass-ratios, within the training range.

Going forward with the ongoing analysis of the astrophysical testing dataset, we are using the $\rho_{\mathcal{M}}$ metric for both dictionaries. The difference in the mass and SNR sensitivities of the two dictionaries may play a role in determining their relative detection efficiencies and potential differences in the detected mBBH population.

4.3 Prospects of development

I am currently analyzing the reconstructions of the astrophysical testing dataset to ascertain the mass, distance, and SNR of black holes that are detected. The final results, although not available as of now, will be submitted for publication by the end of my PhD. There is a bias towards large black holes due to their higher SNRs in both current GW pipelines and in our dictionaries (§ 4.2.2). With the astrophysical testing data, it will be possible to ascertain the degree of the mass bias in our method. Chapter 3 has shown that the majority of astrophysical mBBHs have low masses. Therefore, even slight difference in the mass bias between match-filtering pipelines used in the LVK and our dictionary method could

potentially lead to significantly different detected rates and population.

In addition to the simulated testing data, I will test the dictionary reconstruction on real data. Comparing the FARs between the dictionary method and the LVK pipeline using detected events in the GWTC-3 catalog [Abbott et al., 2023] can be a litmus test to rank the performance and identify shortcomings of our algorithm in comparison to the state-of-the-art match-filtering pipelines. For completeness, we also plan to analyze chunks of real data that have no triggers to test the performance of our algorithm. Meanwhile, Charlie is in the process of producing more noise realizations, extending the total time up to a year. With this, I can verify and improve the robustness of the extrapolation method.

I have thus far shown the performance of the dictionary for a single detector (Hanford). The next step is to produce the results for the other detectors and to define a network analysis. This will require steps that check if the signal is above the detection threshold in the individual and the network of detectors, in addition to checks for coincidence i.e., the time difference between the reconstructed merger should be less than or equal to the GW travel time between detectors. This will help decrease the FAR and improve our detection performance significantly.

Chapter 5

Conclusions and perspectives

In this thesis, I analyzed the merging binary black holes (mBBHs) in the Universe using a two-pronged approach. First, from an astrophysical perspective, I focused on understanding the progenitor environment of mBBHs using simulations of star formation and binary evolution. Second, from the observation side, I developed a machine learning-based algorithm with the goal of detecting gravitational wave (GWs) signals from mBBHs and understanding the detectable population.

To understand the progenitor environments of the astrophysical population of mBBHs in the Universe, I created 240 models, built using 6 mass-metallicity relations in the star formation rate (SFR) and 40 binary population synthesis (BPS) models. Crucial factors influencing the formation and mass of mBBHs are the initial binary parameters, metallicity, mass transfers, and supernova prescription. I found that the default BPS model and the variations explored in my analysis are overestimating the merger rate when compared to GW observations by about a factor of three for the mass-metallicity model with a higher abundance of high metallicity stars [Kobulnicky and Kewley, 2004], and by an order of magnitude for the model with a comparatively low abundance of high metallicity [Pettini and Pagel, 2004]. Globally, the merger rates of mBBHs do not show significant variations across BPS models, although with a few outliers with large deviations. In contrast, the choice of the SFR can influence the rate by up to a factor of four. The merger rate for my different models primarily result from the interplay between the SFR and the efficiency of the formation of mBBHs as a function of metallicity. For progenitor metallicity below 0.1 $Z_{\odot}$, the SFR is low, whereas, for metallicity greater than 0.3 $Z_{\odot}$, the efficiency of mBBH formation drops significantly. As a result, BPS models with large efficiencies at intermediate metallicities (0.1 to 0.3 $Z_{\odot}$) have large progenitor formation rates which contribute to large merger rates.

Mass-metallicity relation models that predict high formation rates of low-metallicity stars lead to high BBH merger rates. As a result, the redshift extrapolation of the Chruslinska and Nelemans [2019] model which predict a higher abundance of low-metallicity stars

has consistently higher merger rates than that of Ma et al. [2016]. Moreover, the large BBH merger rates predicted by the Pettini and Pagel [2004] mass-metallicity calibration in comparison with GW observations indicate that either all BPS models are overly optimistic or that Pettini and Pagel [2004] calibration is in tension with GW observations.

Generally, high-metallicity progenitor environments lead to the formation of smaller black holes due to the effect of metallicity on wind-driven mass loss. As a result, massive black holes (30 - 45 $M_\odot$) tend to form from low-metallicity progenitors, and small black holes (5 - 10 $M_\odot$) arise from higher metallicity progenitors. The mass spectrum of the black holes in my default simulation is in tension with the LVK observations, except in the 30 - 40 $M_\odot$ region, indicating limitations in our model of stellar binary physics. However, consistent with the trend seen from LVK observations, there is a higher abundance of low mass black holes due to the shape of the initial mass function and the abundance of high metallicity in the Universe.

The observed evolution of the merger rate as a function of redshift is limited by the GW detector sensitivity. However, with my simulations, I can evaluate the merger rate up to redshift eight. The merger rate peaked $\simeq$ 8.6 Gyr ago. This is about 1 Gyr after the peak in my SFR ($\simeq$ 9.6 Gyr ago), consistent with the delay time distribution of the binary evolution models.

When trying to infer to the typical progenitor environment of the whole astrophysical population of merging black holes, I find that most systems come from regions with $Z \simeq 0.1 - 0.3\ Z_\odot$, regardless of the model. On the other hand, I find strong variations in the typical formation galaxy mass, depending both on the metallicity and the binary evolution model.

Nevertheless, the inferred formation galaxy distribution typically presents three peaks of varying importance: present-day dwarf galaxies with low metallicity ($M_{\rm Gal} \lesssim 10^8\ M_\odot$, $Z \lesssim 0.05\ Z_\odot$), larger galaxies with intermediate metallicity ($M_{\rm Gal} \simeq 10^9 - 10^{10}\ M_\odot$, $Z \simeq 0.1 - 0.3\ Z_\odot$), and massive galaxies with high metallicity ($M_{\rm Gal} \gtrsim 10^{11}\ M_\odot$, $Z \gtrsim 0.5\ Z_\odot$). The three peaks are respectively due to the high mBBH formation efficiency for low metallicities, the interplay between the SFR and the mBBH formation efficiency for intermediate metallicities, and the high SFR of massive galaxies. Given the current uncertainties on the global star formation history of the Universe and stellar/binary evolution, inferring the typical formation-galaxies of merging black holes should be done with caution.

When considering the progenitor formation rates of currently *detectable* mBBHs, I find that I can predict the progenitor environment with more confidence. The majority of detected mBBHs are from dwarf galaxies with intermediate metallicities. Across models, I showed a distinct contribution from progenitors formed at high $z_{\rm f}$ (> 2), in large galaxies ($M_{\rm Gal} \gtrsim 10^{10.5}\ M_\odot$) as well as a contribution from progenitors formed recently ($z_{\rm f} < 0.5$) in intermediate-mass galaxies ($M_{\rm Gal} \lesssim 10^{10}\ M_\odot$). The latter arise from binaries with small delay times (< 700 Myr) while the former comes from systems with much longer delay time scales. My progenitor posterior generation pipeline shows that GW150914 likely came

from small, dwarf galaxies ($M_{\rm Gal} \lesssim 10^9$ M$_\odot$) with very low metallicity ($Z \simeq 0.025$ Z$_\odot$).

In this thesis, I construct the SFR assuming one model of the galaxy stellar mass function based on Tomczak et al. [2014]. Other models have lower number of low-mass galaxies which, as I've shown, are likely progenitor galaxies of mBBHs. Differences in the assumed galaxy distribution can vary the merger rate by up to half an order of magnitude [Neijssel et al., 2019]. Therefore, an important follow-up study to my analysis, is to probe the effect of different galaxy stellar mass function models (e.g. Furlong et al., 2015, Panter et al., 2004) on the progenitor environment.

The novel procedure proposed in this manuscript to produce galaxy posteriors of mBBH progenitors has two drawbacks. First, it does not take into account other mBBH formation channels, primarily dynamical interactions in dense stellar clusters. Black holes interacting in dense clusters can undergo successive BBH mergers. Importantly, the component masses of these systems can be greater than the upper mass limit of black holes in isolated binary evolution (i.e., $\gtrsim 45$ M$_\odot$). There are multiple LVK observations in this mass range highlighting the importance of including this formation channel. Therefore, an important next step is to include dynamical formation of mBBHs into my existing model (containing only isolated binary evolution) to provide a better informed progenitor posterior. I can model the relation between the black hole mergers in galactic clusters and the properties of the formation galaxy based on semi-analytical prescription to model mBBH populations in star clusters [Kritos et al., 2022]. An exciting future avenue of research is to analyze the progenitor environment posteriors of all LVK mBBH detections and to present a population study of the progenitors based on real observations.

The second drawback of the progenitor posterior generation method is that I cannot compare the galaxy posteriors with real observations as it is limited to mBBHs which are unlikely to produce an electromagnetic (EM) counterpart. A logical extension of the method is to include binary neutron star (BNS) mergers whose EM counterparts can provide information about the galactic environment [Abbott et al., 2017]. However, this is not trivial. Similar to the procedure for my current mBBH analysis, it is important to first explore different binary evolution and SFR models, and understand its effect on the BNS progenitor environment. Moreover, it would entail a a fair amount of rerunning of the simulation to produce a population of BNS. Eq. (2.6) will still hold true for BNSs after swapping the black hole mass terms to that of the neutron stars.

The second part of my thesis focused on the detection of GWs from mBBHs in collaboration with another doctoral student. We have developed a novel adaptation of the machine learning technique, sparse dictionary coding, to detect GWs from mBBHs. I developed two detection metrics, the overlap O, or correlation, between the detector data and dictionary reconstruction, and the match SNR $\rho_{\mathcal{M}}$, i.e., the overlap weighted by the energy of the data, to help classify the presence and absence of a GW signal. I computed the noise statistic and evaluated the false alarm rate (FAR) of the method for two competing dictionaries. I then generated and analyzed the receiver operating characteristics (ROC) for the two dic-

tionaries and two metrics to identify the optimal detection metric $\rho_{\mathcal{M}}$. I also find that the two dictionaries have similar detection efficiencies indicating a robustness of performance to dictionary hyper-parameters. However, the two dictionaries show differences in their sensitivity towards different signal SNR and mBBH masses. I use both dictionaries with the $\rho_{\mathcal{M}}$ metric for the ongoing analysis with my default astrophysical mBBHs population. The dictionary method shows a detection bias towards mBBHs that are nearby and with higher chirp mass.

The short-term goals of this GW detection algorithm are to analyze my astrophysical population of mergers and to ascertain the types of systems that are detectable in comparison to that of the LVK pipelines. A novelty in our approach is the use of the synthetic astrophysical mBBH population from my simulations in the development of our algorithm, in lieu of phenomenological models used in the development of most detection pipelines. Besides, it is important to gauge the performance of the algorithm with real data in comparison to LVK pipelines. To this end, by analyzing real GW triggers, I will compare the FARs of our method and that from state-of-the-art match filtering pipelines. With regards to long-term goals for the project, we aim to incorporate a four detector network detection statistic. I also wish to investigate the use of the dictionary reconstructions as a pre-processing step in existing detection pipelines, similar to the function of a de-noising filter. Similarly, the reconstructions of the dictionary of a GW trigger can potentially help guide rapid parameter estimation pipelines towards a faster, and computationally efficient, initial guess of the best-fitting template waveform.

Bibliography

B. P. Abbott et al. Observation of gravitational waves from a binary black hole merger. *Physical Review Letters*, 116:061102, Feb 2016a. doi: 10.1103/PhysRevLett.116.061102. URL https://link.aps.org/doi/10.1103/PhysRevLett.116.061102.

B. P. Abbott et al. Astrophysical Implications of the Binary Black-hole Merger GW150914. *The Astrophysical Journal Letters*, 818(2):L22, Feb. 2016b. doi: 10.3847/2041-8205/818/2/L22.

R. Abbott et al. GW170817: Observation of Gravitational Waves from a Binary Neutron Star Inspiral. *Physical Review Letters*, 119(16):161101, Oct. 2017. doi: 10.1103/PhysRevLett.119.161101.

R. Abbott et al. Prospects for observing and localizing gravitational-wave transients with Advanced LIGO, Advanced Virgo and KAGRA. *Living Reviews in Relativity*, 21(1):3, Apr. 2018. doi: 10.1007/s41114-018-0012-9.

R. Abbott et al. Population Properties of Compact Objects from the Second LIGO-Virgo Gravitational-Wave Transient Catalog. *The Astrophysical Journal Letters*, 913(1):L7, May 2021. doi: 10.3847/2041-8213/abe949.

R. Abbott et al. Population of Merging Compact Binaries Inferred Using Gravitational Waves through GWTC-3. *Physical Review X*, 13(1):011048, Jan. 2023. doi: 10.1103/PhysRevX.13.011048.

B. Allen, W. G. Anderson, P. R. Brady, D. A. Brown, and J. D. E. Creighton. Findchirp: An algorithm for detection of gravitational waves from inspiraling compact binaries. *Physical Review D*, 85:122006, Jun 2012. doi: 10.1103/PhysRevD.85.122006. URL https://link.aps.org/doi/10.1103/PhysRevD.85.122006.

M. C. Artale, M. Mapelli, Y. Bouffanais, N. Giacobbo, M. Pasquato, and M. Spera. Mass and star formation rate of the host galaxies of compact binary mergers across cosmic time. *Monthly Notices of the Royal Astronomical Society*, 491(3):3419–3434, Jan. 2020. doi: 10.1093/mnras/stz3190.

A. Askar, M. Szkudlarek, D. Gondek-Rosińska, M. Giersz, and T. Bulik. MOCCA-SURVEY Database - I. Coalescing binary black holes originating from globular clusters. *Monthly Notices of the Royal Astronomical Society*, 464(1):L36–L40, Jan. 2017. doi: 10.1093/mnrasl/slw177.

M. Asplund, N. Grevesse, A. J. Sauval, and P. Scott. The Chemical Composition of the Sun. *Annual Review of Astronomy and Astrophysics*, 47(1):481–522, Sept. 2009. doi: 10.1146/annurev.astro.46.060407.145222.

F. Aubin, F. Brighenti, R. Chierici, D. Estevez, G. Greco, G. M. Guidi, V. Juste, F. Marion, B. Mours, E. Nitoglia, O. Sauter, and V. Sordini. The MBTA pipeline for detecting compact binary coalescences in the third LIGO-Virgo observing run. *Classical and Quantum Gravity*, 38(9):095004, May 2021. doi: 10.1088/1361-6382/abe913.

C. Badger, K. Martinovic, A. Torres-Forné, M. Sakellariadou, and J. A. Font. Dictionary Learning: A Novel Approach to Detecting Binary Black Holes in the Presence of Galactic Noise with LISA. *Physical Review Letters*, 130(9):091401, Mar. 2023. doi: 10.1103/PhysRevLett.130.091401.

V. Baibhav, E. Berti, D. Gerosa, M. Mapelli, N. Giacobbo, Y. Bouffanais, and U. N. Di Carlo. Gravitational-wave detection rates for compact binaries formed in isolation: Ligo/virgo o3 and beyond. *Physical Review D*, 100:064060, Sep 2019. doi: 10.1103/PhysRevD.100.064060. URL `https://link.aps.org/doi/10.1103/PhysRevD.100.064060`.

G. Baltus, J. Janquart, M. Lopez, H. Narola, and J.-R. Cudell. Convolutional neural network for gravitational-wave early alert: Going down in frequency. *Physical Review D*, 106(4):042002, Aug. 2022. doi: 10.1103/PhysRevD.106.042002.

I. Baraffe and M. F. El Eid. Evolution of massive stars with variable initial compositions. *Astronomy and Astrophysics*, 245(2):548–560, May 1991.

R. Barkana and A. Loeb. In the beginning: the first sources of light and the reionization of the universe. *Physics Reports*, 349(2):125–238, July 2001. doi: 10.1016/S0370-1573(01)00019-9.

S. S. Bavera, T. Fragos, M. Zevin, C. P. L. Berry, P. Marchant, J. J. Andrews, S. Coughlin, A. Dotter, K. Kovlakas, D. Misra, J. G. Serra-Perez, Y. Qin, K. A. Rocha, J. Román-Garza, N. H. Tran, and E. Zapartas. The impact of mass-transfer physics on the observable properties of field binary black hole populations. *Astronomy and Astrophysics*, 647:A153, Mar. 2021. doi: 10.1051/0004-6361/202039804.

S. S. Bavera, T. Fragos, E. Zapartas, J. J. Andrews, V. Kalogera, C. P. L. Berry, M. Kruckow, A. Dotter, K. Kovlakas, D. Misra, K. A. Rocha, P. M. Srivastava, M. Sun, and Z. Xing.

The formation of merging black holes with masses beyond 30 $M_\odot$ at solar metallicity. *Nature Astronomy*, June 2023. doi: 10.1038/s41550-023-02018-5.

P. S. Behroozi, C. Conroy, and R. H. Wechsler. A comprehensive analysis of the stellar mass-halo mass relation for 0<z<4. *The Astrophysical Journal*, 717(1):379–403, jun 2010. doi: 10.1088/0004-637x/717/1/379. URL https://doi.org/10.1088/0004-637x/717/1/379.

P. S. Behroozi, R. H. Wechsler, and C. Conroy. The average star formation histories of galaxies in dark matter halos from z = 0-8. *The Astrophysical Journal*, 770(1):57, may 2013. doi: 10.1088/0004-637x/770/1/57. URL https://doi.org/10.1088/0004-637x/770/1/57.

K. Belczynski, V. Kalogera, and T. Bulik. A Comprehensive Study of Binary Compact Objects as Gravitational Wave Sources: Evolutionary Channels, Rates, and Physical Properties. *Astrophysical Journal*, 572(1):407–431, June 2002. doi: 10.1086/340304.

K. Belczynski, V. Kalogera, F. A. Rasio, R. E. Taam, A. Zezas, T. Bulik, T. J. Maccarone, and N. Ivanova. Compact Object Modeling with the StarTrack Population Synthesis Code. *Astrophysical Journal Supplement*, 174(1):223–260, Jan. 2008. doi: 10.1086/521026.

K. Belczynski, D. E. Holz, T. Bulik, and R. O'Shaughnessy. The first gravitational-wave source from the isolated evolution of two stars in the 40-100 solar mass range. *Nature*, 534(7608):512–515, June 2016. doi: 10.1038/nature18322.

D. Berg, E. Skillman, D. Garnett, K. Croxall, A. Marble, J. Smith, K. Gordon, and R. Jr. New radial abundance gradients for ngc 628 and ngc 2403. *The Astrophysical Journal*, 775, 09 2013. doi: 10.1088/0004-637X/775/2/128.

M. Bergemann et al. The Gaia-ESO Survey: radial metallicity gradients and age-metallicity relation of stars in the Milky Way disk. *Astronomy and Astrophysics*, 565:A89, May 2014. doi: 10.1051/0004-6361/201423456.

H. A. Bethe and G. E. Brown. Evolution of Binary Compact Objects That Merge. *Astrophysical Journal*, 506(2):780–789, Oct. 1998. doi: 10.1086/306265.

A. Blaauw. On the origin of the O- and B-type stars with high velocities (the "run-away" stars), and some related problems. *Bulletin Astronomical Institute of the Netherlands*, 15: 265, May 1961.

L. Boco, A. Lapi, S. Goswami, F. Perrotta, C. Baccigalupi, and L. Danese. Merging Rates of Compact Binaries in Galaxies: Perspectives for Gravitational Wave Detections. *Astrophysical Journal*, 881(2):157, Aug. 2019. doi: 10.3847/1538-4357/ab328e.

Y. Bouffanais, M. Mapelli, F. Santoliquido, N. Giacobbo, U. N. Di Carlo, S. Rastello, M. C. Artale, and G. Iorio. New insights on binary black hole formation channels after GWTC-2: young star clusters versus isolated binaries. *Monthly Notices of the Royal Astronomical Society*, 507(4):5224–5235, Nov. 2021. doi: 10.1093/mnras/stab2438.

S. Boyd, N. Parikh, E. Chu, B. Peleato, and J. Eckstein. Distributed optimization and statistical learning via the alternating direction method of multipliers. *Foundations and Trends in Machine Learning*, 3:1–122, 01 2011. doi: 10.1561/2200000016.

M. Boyle et al. The SXS collaboration catalog of binary black hole simulations. *Classical and Quantum Gravity*, 36(19):195006, Oct. 2019. doi: 10.1088/1361-6382/ab34e2.

J. C. Bray and J. J. Eldridge. Neutron star kicks and their relationship to supernovae ejecta mass. *Monthly Notices of the Royal Astronomical Society*, 461(4):3747–3759, Oct. 2016. doi: 10.1093/mnras/stw1275.

K. Breivik et al. COSMIC Variance in Binary Population Synthesis. *Astrophys. J.*, 898(1): 71, 2020.

M. M. Briel, J. J. Eldridge, E. R. Stanway, H. F. Stevance, and A. A. Chrimes. Estimating transient rates from cosmological simulations and BPASS. *Monthly Notices of the Royal Astronomical Society*, 514(1):1315–1334, July 2022. doi: 10.1093/mnras/stac1100.

J. P. Brodie and J. Strader. Extragalactic Globular Clusters and Galaxy Formation. *Annual Review of Astronomy and Astrophysics*, 44(1):193–267, Sept. 2006. doi: 10.1146/annurev.astro.44.051905.092441.

F. S. Broekgaarden, E. Berger, S. Stevenson, S. Justham, I. Mandel, M. Chruślińska, L. A. C. van Son, T. Wagg, A. Vigna-Gómez, S. E. de Mink, D. Chattopadhyay, and C. J. Neijssel. Impact of massive binary star and cosmic evolution on gravitational wave observations - II. Double compact object rates and properties. *Monthly Notices of the Royal Astronomical Society*, 516(4):5737–5761, Nov. 2022. doi: 10.1093/mnras/stac1677.

J. Brown. Calculation of a constant q spectral transform. *Journal of the Acoustical Society of America*, 89:425–, 01 1991. doi: 10.1121/1.400476.

W. M. Brunish and J. W. Truran. The evolution of massive stars. II. The influence of initial composition and mass loss. *Astrophysical Journal Supplement*, 49:447–468, July 1982. doi: 10.1086/190806.

A. Burrows and J. Hayes. Pulsar Recoil and Gravitational Radiation Due to Asymmetrical Stellar Collapse and Explosion. *Physical Review Letters*, 76(3):352–355, Jan. 1996. doi: 10.1103/PhysRevLett.76.352.

J. Centrella, J. G. Baker, B. J. Kelly, and J. R. van Meter. Black-hole binaries, gravitational waves, and numerical relativity. *Rev. Mod. Phys.*, 82:3069, 2010. doi: 10.1103/RevModPhys.82.3069.

S. Chakrabarti, P. Chang, R. O'Shaughnessy, A. M. Brooks, S. Shen, J. Bellovary, W. Gladysz, and C. Belczynski. The contribution of outer h i disks to the merging binary black hole population. *The Astrophysical Journal Letters*, 850(1):L4, nov 2017. doi: 10.3847/2041-8213/aa9655. URL https://dx.doi.org/10.3847/2041-8213/aa9655.

S. S. Chen, D. L. Donoho, and M. A. Saunders. Atomic decomposition by basis pursuit. *SIAM Review*, 43(1):129–159, 2001. doi: 10.1137/S003614450037906X. URL https://doi.org/10.1137/S003614450037906X.

M. Chruślińska. Chemical evolution of the Universe and its consequences for gravitational-wave astrophysics. *arXiv e-prints*, art. arXiv:2206.10622, June 2022.

M. Chruslinska and G. Nelemans. Metallicity of stars formed throughout the cosmic history based on the observational properties of star-forming galaxies. *Monthly Notices of the Royal Astronomical Society*, 488(4):5300–5326, Oct. 2019. doi: 10.1093/mnras/stz2057.

A. Cimatti, F. Fraternali, and C. Nipoti. Introduction to Galaxy Formation and Evolution. From Primordial Gas to Present-Day Galaxies. *arXiv e-prints*, art. arXiv:1912.06216, Dec. 2019. doi: 10.48550/arXiv.1912.06216.

J. S. W. Claeys, O. R. Pols, R. G. Izzard, J. Vink, and F. W. M. Verbunt. Theoretical uncertainties of the Type Ia supernova rate. *Astronomy and Astrophysics*, 563:A83, Mar. 2014. doi: 10.1051/0004-6361/201322714.

S. Cole, J. Helly, C. S. Frenk, and H. Parkinson. The statistical properties of cold dark matter halo formation. *Monthly Notices of the Royal Astronomical Society*, 383(2): 546–556, 12 2007. ISSN 0035-8711. doi: 10.1111/j.1365-2966.2007.12516.x. URL https://doi.org/10.1111/j.1365-2966.2007.12516.x.

J. M. Corral-Santana, J. Casares, T. Muñoz-Darias, F. E. Bauer, I. G. Martínez-Pais, and D. M. Russell. BlackCAT: A catalogue of stellar-mass black holes in X-ray transients. *Astronomy and Astrophysics*, 587:A61, Mar. 2016. doi: 10.1051/0004-6361/201527130.

F. Cullen et al. The NIRVANDELS Survey: a robust detection of α-enhancement in star-forming galaxies at z 3.4. *Monthly Notices of the Royal Astronomical Society*, 505(1): 903–920, July 2021. doi: 10.1093/mnras/stab1340.

E. Cuoco et al. Enhancing Gravitational-Wave Science with Machine Learning. *arXiv e-prints*, art. arXiv:2005.03745, May 2020. doi: 10.48550/arXiv.2005.03745.

M. de Kool. Common Envelope Evolution and Double Cores of Planetary Nebulae. *Astrophysical Journal*, 358:189, July 1990. doi: 10.1086/168974.

U. N. Di Carlo, N. Giacobbo, M. Mapelli, M. Pasquato, M. Spera, L. Wang, and F. Haardt. Merging black holes in young star clusters. *Monthly Notices of the Royal Astronomical Society*, 487(2):2947–2960, Aug. 2019. doi: 10.1093/mnras/stz1453.

M. Dominik, K. Belczynski, C. Fryer, D. E. Holz, E. Berti, T. Bulik, I. Mandel, and R. O'Shaughnessy. Double Compact Objects. I. The Significance of the Common Envelope on Merger Rates. *Astrophysical Journal*, 759(1):52, Nov. 2012. doi: 10.1088/0004-637X/759/1/52.

M. Dominik, K. Belczynski, C. Fryer, D. E. Holz, E. Berti, T. Bulik, I. Mandel, and R. O'Shaughnessy. Double Compact Objects. II. Cosmological Merger Rates. *Astrophysical Journal*, 779(1):72, Dec. 2013. doi: 10.1088/0004-637X/779/1/72.

A. Dorozsmai and S. Toonen. Importance of stable mass transfer and stellar winds for the formation of gravitational wave sources. *arXiv e-prints*, art. arXiv:2207.08837, July 2022. doi: 10.48550/arXiv.2207.08837.

P. P. Eggleton. The evolution of low mass stars. *Monthly Notices of the Royal Astronomical Society*, 151:351, Jan. 1971. doi: 10.1093/mnras/151.3.351.

M. Elad and M. Aharon. Image denoising via sparse and redundant representations over learned dictionaries. *IEEE Transactions on Image Processing*, 15(12):3736–3745, 2006. doi: 10.1109/TIP.2006.881969.

J. J. Eldridge and E. R. Stanway. BPASS predictions for binary black hole mergers. *Monthly Notices of the Royal Astronomical Society*, 462(3):3302–3313, Nov. 2016. doi: 10.1093/mnras/stw1772.

J. J. Eldridge, E. R. Stanway, and P. N. Tang. A consistent estimate for gravitational wave and electromagnetic transient rates. *Monthly Notices of the Royal Astronomical Society*, 482(1):870–880, Jan. 2019. doi: 10.1093/mnras/sty2714.

M. Fishbach and V. Kalogera. Apples and oranges: Comparing black holes in x-ray binaries and gravitational-wave sources. *The Astrophysical Journal Letters*, 929(2):L26, apr 2022. doi: 10.3847/2041-8213/ac64a5. URL https://dx.doi.org/10.3847/2041-8213/ac64a5.

F. Fortin, F. García, A. Simaz Bunzel, and S. Chaty. A catalogue of high-mass X-ray binaries in the Galaxy: from the INTEGRAL to the Gaia era. *Astronomy and Astrophysics*, 671: A149, Mar. 2023. doi: 10.1051/0004-6361/202245236.

C. L. Fryer, S. E. Woosley, and A. Heger. Pair-Instability Supernovae, Gravity Waves, and Gamma-Ray Transients. *Astrophysical Journal*, 550(1):372–382, Mar. 2001. doi: 10.1086/319719.

C. L. Fryer, K. Belczynski, G. Wiktorowicz, M. Dominik, V. Kalogera, and D. E. Holz. Compact Remnant Mass Function: Dependence on the Explosion Mechanism and Metallicity. *Astrophysical Journal*, 749(1):91, Apr. 2012. doi: 10.1088/0004-637X/749/1/91.

M. Furlong, R. G. Bower, T. Theuns, J. Schaye, R. A. Crain, M. Schaller, C. Dalla Vecchia, C. S. Frenk, I. G. McCarthy, J. Helly, A. Jenkins, and Y. M. Rosas-Guevara. Evolution of galaxy stellar masses and star formation rates in the EAGLE simulations. *Monthly Notices of the Royal Astronomical Society*, 450(4):4486–4504, July 2015. doi: 10.1093/mnras/stv852.

F. García, A. Simaz Bunzel, S. Chaty, E. Porter, and E. Chassande-Mottin. Progenitors of low-mass binary black-hole mergers in the isolated binary evolution scenario. , 649: A114, May 2021. doi: 10.1051/0004-6361/202038357.

S. Garrison-Kimmel, M. Rocha, M. Boylan-Kolchin, J. S. Bullock, and J. Lally. Can feedback solve the too-big-to-fail problem? *Monthly Notices of the Royal Astronomical Society*, 433(4):3539–3546, 06 2013. ISSN 0035-8711. doi: 10.1093/mnras/stt984. URL `https://doi.org/10.1093/mnras/stt984`.

D. George and E. A. Huerta. Deep neural networks to enable real-time multimessenger astrophysics. *Physical Review D*, 97:044039, Feb 2018. doi: 10.1103/PhysRevD.97.044039. URL `https://link.aps.org/doi/10.1103/PhysRevD.97.044039`.

N. Giacobbo and M. Mapelli. The progenitors of compact-object binaries: impact of metallicity, common envelope and natal kicks. *Monthly Notices of the Royal Astronomical Society*, 480(2):2011–2030, Oct. 2018. doi: 10.1093/mnras/sty1999.

N. Giacobbo and M. Mapelli. Revising Natal Kick Prescriptions in Population Synthesis Simulations. *Astrophysical Journal*, 891(2):141, Mar. 2020. doi: 10.3847/1538-4357/ab7335.

N. Giacobbo, M. Mapelli, and M. Spera. Merging black hole binaries: the effects of progenitor's metallicity, mass-loss rate and Eddington factor. *Monthly Notices of the Royal Astronomical Society*, 474(3):2959–2974, Mar. 2018. doi: 10.1093/mnras/stx2933.

T. Goldstein and S. Osher. The split bregman method for l1-regularized problems. *SIAM Journal on Imaging Sciences*, 2(2):323–343, 2009. doi: 10.1137/080725891. URL https://doi.org/10.1137/080725891.

G. Gräfener and W. R. Hamann. Mass loss from late-type WN stars and its Z-dependence. Very massive stars approaching the Eddington limit. *Astronomy and Astrophysics*, 482 (3):945–960, May 2008. doi: 10.1051/0004-6361:20066176.

L. Graziani, R. Schneider, S. Marassi, W. Del Pozzo, M. Mapelli, and N. Giacobbo. Cosmic archaeology with massive stellar black hole binaries. *Monthly Notices of the Royal Astronomical Society*, 495(1):L81–L85, June 2020. doi: 10.1093/mnrasl/slaa063.

M. Hannam, P. Schmidt, A. Bohé, L. Haegel, S. Husa, F. Ohme, G. Pratten, and M. Pürrer. Simple Model of Complete Precessing Black-Hole-Binary Gravitational Waveforms. *Physical Review Letters*, 113(15):151101, Oct. 2014. doi: 10.1103/PhysRevLett.113.151101.

R. Henry, K. Kwitter, A. Jaskot, B. Balick, M. Morrison, and J. Milingo. Abundances of galactic anticenter planetary nebulae and the oxygen abundance gradient in the galactic disk. *Astrophysical Journal*, 724, 09 2010. doi: 10.1088/0004-637X/724/1/748.

M. S. Hjellming and R. F. Webbink. Thresholds for Rapid Mass Transfer in Binary System. I. Polytropic Models. *Astrophysical Journal*, 318:794, July 1987. doi: 10.1086/165412.

P. F. Hopkins, D. Kereš, J. Oñorbe, C.-A. Faucher-Giguère, E. Quataert, N. Murray, and J. S. Bullock. Galaxies on FIRE (Feedback In Realistic Environments): stellar feedback explains cosmologically inefficient star formation. *Monthly Notices of the Royal Astronomical Society*, 445(1):581–603, 09 2014. ISSN 0035-8711. doi: 10.1093/mnras/stu1738. URL https://doi.org/10.1093/mnras/stu1738.

J. R. Hurley, C. A. Tout, and O. R. Pols. Evolution of binary stars and the effect of tides on binary populations. *Monthly Notices of the Royal Astronomical Society*, 329(4):897–928, Feb. 2002.

N. Ivanova, S. Justham, X. Chen, O. De Marco, C. Fryer, E. Gaburov, H. Ge, E. Glebbeek, Z. Han, X.-D. Li, et al. Common envelope evolution: where we stand and how we can move forward. *The Astronomy and Astrophysics Review*, 21:1–73, 2013.

H. T. Janka and E. Mueller. Neutron star recoils from anisotropic supernovae. *Astronomy and Astrophysics*, 290:496–502, Oct. 1994.

R. D. Jeffries. Measuring the Initial Mass Function of Low Mass Stars and Brown Dwarfs. In C. Reylé, C. Charbonnel, and M. Schultheis, editors, *EAS Publications Series*, volume 57 of *EAS Publications Series*, pages 45–89, Nov. 2012. doi: 10.1051/eas/1257002.

V. Kalogera, K. Belczynski, C. Kim, R. O'Shaughnessy, and B. Willems. Formation of double compact objects. *Physics Reports*, 442(1-6):75–108, Apr. 2007. doi: 10.1016/j.physrep.2007.02.008.

S. Khan, S. Husa, M. Hannam, F. Ohme, M. Pürrer, X. Jiménez Forteza, and A. Bohé. Frequency-domain gravitational waves from nonprecessing black-hole binaries. II. A phenomenological model for the advanced detector era. *Physical Review D*, 93(4):044007, 2016. doi: 10.1103/PhysRevD.93.044007.

J. Klencki, M. Moe, W. Gladysz, M. Chruslinska, D. E. Holz, and K. Belczynski. Impact of inter-correlated initial binary parameters on double black hole and neutron star mergers. *Astronomy and Astrophysics*, 619:A77, Nov. 2018. doi: 10.1051/0004-6361/201833025.

A. A. Klypin and S. F. Shandarin. Three-dimensional numerical model of the formation of large-scale structure in the Universe. *Monthly Notices of the Royal Astronomical Society*, 204:891–907, Sept. 1983. doi: 10.1093/mnras/204.3.891.

H. A. Kobulnicky and L. J. Kewley. Metallicities of 0.3<z<1.0 Galaxies in the GOODS-North Field. *Astrophysical Journal*, 617(1):240–261, Dec. 2004. doi: 10.1086/425299.

K. Kritos, V. Strokov, V. Baibhav, and E. Berti. Rapster: a fast code for dynamical formation of black-hole binaries in dense star clusters. *arXiv e-prints*, art. arXiv:2210.10055, Oct. 2022. doi: 10.48550/arXiv.2210.10055.

P. Kroupa. On the variation of the initial mass function. *Monthly Notices of the Royal Astronomical Society*, 322(2):231–246, 04 2001. ISSN 0035-8711. doi: 10.1046/j.1365-8711.2001.04022.x. URL `https://doi.org/10.1046/j.1365-8711.2001.04022.x`.

P. Kroupa, C. Weidner, J. Pflamm-Altenburg, I. Thies, J. Dabringhausen, M. Marks, and T. Maschberger. The Stellar and Sub-Stellar Initial Mass Function of Simple and Composite Populations. In T. D. Oswalt and G. Gilmore, editors, *Planets, Stars and Stellar Systems. Volume 5: Galactic Structure and Stellar Populations*, volume 5, page 115. 2013. doi: 10.1007/978-94-007-5612-0_4.

M. U. Kruckow, T. M. Tauris, N. Langer, M. Kramer, and R. G. Izzard. Progenitors of gravitational wave mergers: binary evolution with the stellar grid-based code COMBINE. *Monthly Notices of the Royal Astronomical Society*, 481(2):1908–1949, Dec. 2018. doi: 10.1093/mnras/sty2190.

R. P. Kudritzki, A. Pauldrach, and J. Puls. Radiation driven winds of hot luminous stars. II. Wind models for O-stars in the Magellanic clouds. *Astronomy and Astrophysics*, 173:293–298, Feb. 1987.

C. Lacey and S. Cole. Merger rates in hierarchical models of galaxy formation. *Monthly Notices of the Royal Astronomical Society*, 262(3):627–649, June 1993. doi: 10.1093/mnras/262.3.627.

A. Lamberts, S. Garrison-Kimmel, D. R. Clausen, and P. F. Hopkins. When and where did GW150914 form? *Monthly Notices of the Royal Astronomical Society*, 463(1):L31–L35, Nov. 2016. doi: 10.1093/mnrasl/slw152.

N. Langer and C. A. Norman. On the collapsar model of long gamma-ray bursts:constraints from cosmic metallicity evolution. *The Astrophysical Journal*, 638(2):L63, jan 2006. doi: 10.1086/500363. URL https://dx.doi.org/10.1086/500363.

L. Lehoucq, I. Dvorkin, R. Srinivasan, C. Pellouin, and A. Lamberts. Astrophysical Uncertainties in the Gravitational-Wave Background from Stellar-Mass Compact Binary Mergers. *arXiv e-prints*, art. arXiv:2306.09861, June 2023. doi: 10.48550/arXiv.2306.09861.

LIGO Scientific Collaboration. LALSuite: LIGO Scientific Collaboration Algorithm Library Suite. Astrophysics Source Code Library, record ascl:2012.021, Dec. 2020.

C. Liotine, M. Zevin, C. P. L. Berry, Z. Doctor, and V. Kalogera. The Missing Link between Black Holes in High-mass X-Ray Binaries and Gravitational-wave Sources: Observational Selection Effects. *Astrophysical Journal*, 946(1):4, mar 2023. doi: 10.3847/1538-4357/acb8b2. URL https://dx.doi.org/10.3847/1538-4357/acb8b2.

K. L. Luhman. The Formation and Early Evolution of Low-Mass Stars and Brown Dwarfs. *Annual Review of Astronomy and Astrophysics*, 50:65–106, Sept. 2012. doi: 10.1146/annurev-astro-081811-125528.

X. Ma, P. F. Hopkins, C.-A. Faucher-Giguère, N. Zolman, A. L. Muratov, D. Kereš, and E. Quataert. The origin and evolution of the galaxy mass-metallicity relation. *Monthly Notices of the Royal Astronomical Society*, 456(2):2140–2156, Feb. 2016. doi: 10.1093/mnras/stv2659.

P. Madau and M. Dickinson. Cosmic star-formation history. *Annual Review of Astronomy and Astrophysics*, 52(1):415–486, 2014. doi: 10.1146/annurev-astro-081811-125615. URL https://doi.org/10.1146/annurev-astro-081811-125615.

A. Maeder and G. Meynet. The Evolution of Rotating Stars. *Annual Review of Astronomy and Astrophysics*, 38:143–190, Jan. 2000. doi: 10.1146/annurev.astro.38.1.143.

M. Maggiore. *Gravitational Waves. Vol. 1: Theory and Experiments*. Oxford University Press, 2007. ISBN 978-0-19-171766-6, 978-0-19-852074-0. doi: 10.1093/acprof:oso/9780198570745.001.0001.

M. Maggiore, C. Van Den Broeck, N. Bartolo, E. Belgacem, D. Bertacca, M. A. Bizouard, M. Branchesi, S. Clesse, S. Foffa, J. García-Bellido, S. Grimm, J. Harms, T. Hinderer, S. Matarrese, C. Palomba, M. Peloso, A. Ricciardone, and M. Sakellariadou. Science case for the Einstein telescope. *Journal of Cosmology and Astroparticle Physics*, 2020 (3):050, Mar. 2020. doi: 10.1088/1475-7516/2020/03/050.

R. Maiolino, T. Nagao, A. Grazian, F. Cocchia, A. Marconi, F. Mannucci, A. Cimatti, A. Pipino, S. Ballero, F. Calura, C. Chiappini, A. Fontana, G. L. Granato, F. Matteucci, G. Pastorini, L. Pentericci, G. Risaliti, M. Salvati, and L. Silva. AMAZE. I. The evolution of the mass-metallicity relation at z > 3. *Astronomy and Astrophysics*, 488(2):463–479, Sept. 2008. doi: 10.1051/0004-6361:200809678.

J. Mairal, F. Bach, J. Ponce, and G. Sapiro. Online dictionary learning for sparse coding. volume 382, page 87, 06 2009. doi: 10.1145/1553374.1553463.

I. Mandel and F. S. Broekgaarden. Rates of compact object coalescences. *Living Reviews in Relativity*, 25(1):1, Dec. 2022. doi: 10.1007/s41114-021-00034-3.

F. Mannucci, G. Cresci, R. Maiolino, A. Marconi, G. Pastorini, L. Pozzetti, A. Gnerucci, G. Risaliti, R. Schneider, M. Lehnert, and M. Salvati. LSD: Lyman-break galaxies Stellar populations and Dynamics - I. Mass, metallicity and gas at z ∼3.1. *Monthly Notices of the Royal Astronomical Society*, 398(4):1915–1931, Oct. 2009. doi: 10.1111/j.1365-2966.2009.15185.x.

M. Mapelli. Massive black hole binaries from runaway collisions: the impact of metallicity. *Monthly Notices of the Royal Astronomical Society*, 459(4):3432–3446, July 2016. doi: 10.1093/mnras/stw869.

M. Mapelli. Astrophysics of stellar black holes. *Proceedings of the International School of Physics E. Fermi*, 200:87–121, 2020. doi: 10.3254/ENFI200005.

M. Mapelli. In *Handbook of Gravitational Wave Astronomy*, page 16. Springer Singapore, 2021a. doi: 10.1007/978-981-15-4702-7_16-1.

M. Mapelli. Formation Channels of Single and Binary Stellar-Mass Black Holes. In *Handbook of Gravitational Wave Astronomy*, page 16. 2021b. doi: 10.1007/978-981-15-4702-7_16-1.

M. Mapelli. Formation Channels of Single and Binary Stellar-Mass Black Holes. In *Handbook of Gravitational Wave Astronomy*, page 16. 2021c. doi: 10.1007/978-981-15-4702-7_16-1.

M. Mapelli and N. Giacobbo. The cosmic merger rate of neutron stars and black holes. *Monthly Notices of the Royal Astronomical Society*, 479(4):4391–4398, Oct. 2018. doi: 10.1093/mnras/sty1613.

M. Mapelli, N. Giacobbo, E. Ripamonti, and M. Spera. The cosmic merger rate of stellar black hole binaries from the Illustris simulation. *Monthly Notices of the Royal Astronomical Society*, 472(2):2422–2435, Dec. 2017. doi: 10.1093/mnras/stx2123.

M. Mapelli, N. Giacobbo, M. Toffano, E. Ripamonti, A. Bressan, M. Spera, and M. Branchesi. The host galaxies of double compact objects merging in the local Universe. *Monthly Notices of the Royal Astronomical Society*, 481(4):5324–5330, 10 2018. ISSN 0035-8711. doi: 10.1093/mnras/sty2663. URL https://doi.org/10.1093/mnras/sty2663.

M. Mapelli, N. Giacobbo, F. Santoliquido, and M. C. Artale. The properties of merging black holes and neutron stars across cosmic time. *Monthly Notices of the Royal Astronomical Society*, 487(1):2–13, July 2019. doi: 10.1093/mnras/stz1150.

M. Mapelli, Y. Bouffanais, F. Santoliquido, M. Arca Sedda, and M. C. Artale. The cosmic evolution of binary black holes in young, globular, and nuclear star clusters: rates, masses, spins, and mixing fractions. *Monthly Notices of the Royal Astronomical Society*, 511(4):5797–5816, 02 2022. ISSN 0035-8711. doi: 10.1093/mnras/stac422. URL https://doi.org/10.1093/mnras/stac422.

S. Marassi, L. Graziani, M. Ginolfi, R. Schneider, M. Mapelli, M. Spera, and M. Alparone. Evolution of dwarf galaxies hosting GW150914-like events. *Monthly Notices of the Royal Astronomical Society*, 484(3):3219–3232, Apr. 2019. doi: 10.1093/mnras/stz170.

P. Marchant, M. Renzo, R. Farmer, K. M. W. Pappas, R. E. Taam, S. E. de Mink, and V. Kalogera. Pulsational Pair-instability Supernovae in Very Close Binaries. *Astrophysical Journal*, 882(1):36, Sept. 2019. doi: 10.3847/1538-4357/ab3426.

P. Marchant, K. M. W. Pappas, M. Gallegos-Garcia, C. P. L. Berry, R. E. Taam, V. Kalogera, and P. Podsiadlowski. The role of mass transfer and common envelope evolution in the formation of merging binary black holes. *Astronomy and Astrophysics*, 650:A107, June 2021. doi: 10.1051/0004-6361/202039992.

S. Mastrogiovanni, A. Lamberts, R. Srinivasan, T. Bruel, and N. Christensen. Inferring binary black holes stellar progenitors with gravitational wave sources. *Monthly Notices of the Royal Astronomical Society*, 517(3):3432–3444, Dec. 2022. doi: 10.1093/mnras/stac2850.

T. Mazeh, D. Goldberg, A. Duquennoy, and M. Mayor. On the Mass-Ratio Distribution of Spectroscopic Binaries with Solar-Type Primaries. *Astrophysical Journal*, 401:265, Dec. 1992. doi: 10.1086/172058.

B. McKernan, K. E. S. Ford, J. Bellovary, N. W. C. Leigh, Z. Haiman, B. Kocsis, W. Lyra, M. M. Mac Low, B. Metzger, M. O'Dowd, S. Endlich, and D. J. Rosen. Constraining Stellar-mass Black Hole Mergers in AGN Disks Detectable with LIGO. *Astrophysical Journal*, 866(1):66, Oct. 2018. doi: 10.3847/1538-4357/aadae5.

C. Messick et al. Analysis framework for the prompt discovery of compact binary mergers in gravitational-wave data. *Physical Review D*, 95(4):042001, Feb. 2017. doi: 10.1103/PhysRevD.95.042001.

H. Mo, F. Van den Bosch, and S. White. *Galaxy formation and evolution*. Cambridge University Press, 2010.

M. Moe and R. Di Stefano. Mind Your Ps and Qs: The Interrelation between Period (P) and Mass-ratio (Q) Distributions of Binary Stars. *Astrophysical Journal Supplement*, 230(2):15, June 2017. doi: 10.3847/1538-4365/aa6fb6.

M. R. Mokiem, A. de Koter, J. S. Vink, J. Puls, C. J. Evans, S. J. Smartt, P. A. Crowther, A. Herrero, N. Langer, D. J. Lennon, F. Najarro, and M. R. Villamariz. The empirical metallicity dependence of the mass-loss rate of O- and early B-type stars. *Astronomy and Astrophysics*, 473(2):603–614, Oct. 2007. doi: 10.1051/0004-6361:20077545.

C. J. Neijssel, A. Vigna-Gómez, S. Stevenson, J. W. Barrett, S. M. Gaebel, F. S. Broekgaarden, S. E. de Mink, D. Szécsi, S. Vinciguerra, and I. Mandel. The effect of the metallicity-specific star formation history on double compact object mergers. *Monthly Notices of the Royal Astronomical Society*, 490(3):3740–3759, Dec. 2019. doi: 10.1093/mnras/stz2840.

K. Nomoto, C. Kobayashi, and N. Tominaga. Nucleosynthesis in Stars and the Chemical Enrichment of Galaxies. *Annual Review of Astronomy and Astrophysics*, 51(1):457–509, Aug. 2013. doi: 10.1146/annurev-astro-082812-140956.

S. S. R. Offner, P. C. Clark, P. Hennebelle, N. Bastian, M. R. Bate, P. F. Hopkins, E. Moraux, and A. P. Whitworth. The Origin and Universality of the Stellar Initial Mass Function. In H. Beuther, R. S. Klessen, C. P. Dullemond, and T. Henning, editors, *Protostars and Planets VI*, pages 53–75, Jan. 2014. doi: 10.2458/azu_uapress_9780816531240-ch003.

R. O'Shaughnessy, J. M. Bellovary, A. Brooks, S. Shen, F. Governato, and C. R. Christensen. The effects of host galaxy properties on merging compact binaries detectable by LIGO. *Monthly Notices of the Royal Astronomical Society*, 464(3):2831–2839, Jan. 2017. doi: 10.1093/mnras/stw2550.

B. Paczynski. Common Envelope Binaries. In P. Eggleton, S. Mitton, and J. Whelan, editors, *Structure and Evolution of Close Binary Systems*, volume 73, page 75, Jan. 1976.

B. Panter, A. F. Heavens, and R. Jimenez. The mass function of the stellar component of galaxies in the Sloan Digital Sky Survey. *Monthly Notices of the Royal Astronomical Society*, 355(3):764–768, 12 2004. ISSN 0035-8711. doi: 10.1111/j.1365-2966.2004.08355.x. URL https://doi.org/10.1111/j.1365-2966.2004.08355.x.

A. Pauldrach, J. Puls, and R. P. Kudritzki. Radiation-driven winds of hot luminous stars. Improvements of the theory and first results. *Astronomy and Astrophysics*, 164:86–100, Aug. 1986.

B. Paxton, L. Bildsten, A. Dotter, F. Herwig, P. Lesaffre, and F. Timmes. Modules for Experiments in Stellar Astrophysics (MESA). *Astrophysical Journal Supplement*, 192 (1):3, Jan. 2011. doi: 10.1088/0067-0049/192/1/3.

P. C. Peters and J. Mathews. Gravitational radiation from point masses in a keplerian orbit. *Physical Review*, 131:435–440, Jul 1963. doi: 10.1103/PhysRev.131.435. URL https://link.aps.org/doi/10.1103/PhysRev.131.435.

M. Pettini and B. E. J. Pagel. [OIII]/[NII] as an abundance indicator at high redshift. *Monthly Notices of the Royal Astronomical Society*, 348(3):L59–L63, Mar. 2004. doi: 10.1111/j.1365-2966.2004.07591.x.

Planck Collaboration et al. Planck 2015 results. XIII. Cosmological parameters. *Astronomy and Astrophysics*, 594:A13, Sept. 2016. doi: 10.1051/0004-6361/201525830.

S. Planelles, D. R. G. Schleicher, and A. M. Bykov. Large-Scale Structure Formation: From the First Non-linear Objects to Massive Galaxy Clusters. *Space Science Reviews*, 188(1-4):93–139, May 2015. doi: 10.1007/s11214-014-0045-7.

O. R. Pols, C. A. Tout, P. P. Eggleton, and Z. Han. Approximate input physics for stellar modelling. *Monthly Notices of the Royal Astronomical Society*, 274(3):964–974, June 1995. doi: 10.1093/mnras/274.3.964.

S. F. Portegies Zwart and S. L. W. McMillan. Black Hole Mergers in the Universe. *The Astrophysical Journal Letters*, 528(1):L17–L20, Jan. 2000. doi: 10.1086/312422.

W. H. Press and P. Schechter. Formation of Galaxies and Clusters of Galaxies by Self-Similar Gravitational Condensation. *Astrophysical Journal*, 187:425–438, Feb. 1974. doi: 10.1086/152650.

J. Puls, J. S. Vink, and F. Najarro. Mass loss from hot massive stars. *Astronomy and Astrophysics Reviews*, 16(3-4):209–325, Dec. 2008. doi: 10.1007/s00159-008-0015-8.

M. Rafelski, A. M. Wolfe, J. X. Prochaska, M. Neeleman, and A. J. Mendez. Metallicity Evolution of Damped Lyα Systems Out to z $\sim$5. *Astrophysical Journal*, 755(2):89, Aug. 2012. doi: 10.1088/0004-637X/755/2/89.

G. Rakavy and G. Shaviv. Instabilities in Highly Evolved Stellar Models. *Astrophysical Journal*, 148:803, June 1967. doi: 10.1086/149204.

D. Reitze et al. Cosmic Explorer: The U.S. Contribution to Gravitational-Wave Astronomy beyond LIGO. In *Bulletin of the American Astronomical Society*, volume 51, page 35, Sept. 2019. doi: 10.48550/arXiv.1907.04833.

M. Rieke, S. Arribas, A. Bunker, S. Charlot, S. Finkelstein, R. Maiolino, B. Robertson, C. Willott, R. Windhorst, D. Eisenstein, E. Nelson, S. Tacchella, E. Egami, R. Endsley, B. Frye, K. Hainline, R. Hviding, G. Rieke, C. Williams, C. Willmer, and C. Woodrum. JWST GTO/ERS Deep Surveys. *Bulletin of the AAS*, 51(3):45, May 2019.

C. L. Rodriguez, M. Morscher, B. Pattabiraman, S. Chatterjee, C.-J. Haster, and F. A. Rasio. Binary Black Hole Mergers from Globular Clusters: Implications for Advanced LIGO. *Physical Review Letters*, 115(5):051101, July 2015. doi: 10.1103/PhysRevLett.115.051101.

C. L. Rodriguez, S. Chatterjee, and F. A. Rasio. Binary black hole mergers from globular clusters: Masses, merger rates, and the impact of stellar evolution. *Physical Review D*, 93(8):084029, Apr. 2016. doi: 10.1103/PhysRevD.93.084029.

A. D. Sakharov. Violation of CP Invariance, C asymmetry, and baryon asymmetry of the universe. *Pisma Zh. Eksp. Teor. Fiz.*, 5:32–35, 1967. doi: 10.1070/PU1991v034n05ABEH002497.

E. E. Salpeter. The Luminosity Function and Stellar Evolution. *Astrophysical Journal*, 121:161, Jan. 1955. doi: 10.1086/145971.

J. Samsing. Eccentric black hole mergers forming in globular clusters. *Physical Review D*, 97(10):103014, May 2018. doi: 10.1103/PhysRevD.97.103014.

H. Sana, S. E. de Mink, A. de Koter, N. Langer, C. J. Evans, M. Gieles, E. Gosset, R. G. Izzard, J.-B. Le Bouquin, and F. R. N. Schneider. Binary interaction dominates the evolution of massive stars. *Science*, 337(6093):444–446, 2012. ISSN 0036-8075. doi: 10.1126/science.1223344. URL `https://science.sciencemag.org/content/337/6093/444`.

F. Santoliquido, M. Mapelli, N. Giacobbo, Y. Bouffanais, and M. C. Artale. The cosmic merger rate density of compact objects: impact of star formation, metallicity, initial mass

function, and binary evolution. *Monthly Notices of the Royal Astronomical Society*, 502 (4):4877–4889, Apr. 2021. doi: 10.1093/mnras/stab280.

F. Santoliquido, M. Mapelli, M. C. Artale, and L. Boco. Modelling the host galaxies of binary compact object mergers with observational scaling relations. *Monthly Notices of the Royal Astronomical Society*, 516(3):3297–3317, Nov. 2022. doi: 10.1093/mnras/stac2384.

M. B. Schäfer. *Machine learning applications in search algorithms for gravitational waves from compact binary mergers*. PhD thesis, Leibniz U., Hannover, 2023.

M. B. Schäfer, O. c. v. Zelenka, A. H. Nitz, F. Ohme, and B. Brügmann. Training strategies for deep learning gravitational-wave searches. *Physical Review D*, 105:043002, Feb 2022. doi: 10.1103/PhysRevD.105.043002. URL https://link.aps.org/doi/10.1103/PhysRevD.105.043002.

M. B. Schäfer et al. First machine learning gravitational-wave search mock data challenge. *Physical Review D*, 107(2):023021, Jan. 2023. doi: 10.1103/PhysRevD.107.023021.

R. Schneider, L. Graziani, S. Marassi, M. Spera, M. Mapelli, M. Alparone, and M. d. Bennassuti. The formation and coalescence sites of the first gravitational wave events. *Monthly Notices of the Royal Astronomical Society: Letters*, 471(1):L105–L109, 07 2017. ISSN 1745-3925. doi: 10.1093/mnrasl/slx118. URL https://doi.org/10.1093/mnrasl/slx118.

S. L. Schrøder, M. MacLeod, E. Ramirez-Ruiz, I. Mandel, T. Fragos, A. Loeb, and R. W. Everson. The Evolution of Binaries under the Influence of Radiation-Driven Winds from a Stellar Companion. *arXiv e-prints*, art. arXiv:2107.09675, July 2021. doi: 10.48550/arXiv.2107.09675.

S. Sigurdsson and L. Hernquist. Primordial black holes in globular clusters. *Nature*, 364 (6436):423–425, July 1993. doi: 10.1038/364423a0.

M. Spera and M. Mapelli. Very massive stars, pair-instability supernovae and intermediate-mass black holes with the sevn code. *Monthly Notices of the Royal Astronomical Society*, 470(4):4739–4749, Oct. 2017. doi: 10.1093/mnras/stx1576.

M. Spera, M. Mapelli, N. Giacobbo, A. A. Trani, A. Bressan, and G. Costa. Merging black hole binaries with the SEVN code. *Monthly Notices of the Royal Astronomical Society*, 485(1):889–907, May 2019. doi: 10.1093/mnras/stz359.

R. Srinivasan, A. Lamberts, M. A. Bizouard, T. Bruel, and S. Mastrogiovanni. Understanding the progenitor formation galaxies of merging binary black holes. *Monthly Notices*

of the Royal Astronomical Society, 06 2023. ISSN 0035-8711. doi: 10.1093/mnras/stad1825. URL https://doi.org/10.1093/mnras/stad1825. stad1825.

S. W. Stahler and F. Palla. *The Formation of Stars*. 2004.

C. C. Steidel, A. L. Strom, M. Pettini, G. C. Rudie, N. A. Reddy, and R. F. Trainor. Reconciling the Stellar and Nebular Spectra of High-redshift Galaxies. *Astrophysical Journal*, 826(2):159, Aug. 2016. doi: 10.3847/0004-637X/826/2/159.

S. Stevenson, A. Vigna-Gómez, I. Mandel, J. W. Barrett, C. J. Neijssel, D. Perkins, and S. E. de Mink. Formation of the first three gravitational-wave observations through isolated binary evolution. *Nature Communications*, 8:14906, Apr. 2017. doi: 10.1038/ncomms14906.

A. L. Strom, G. C. Rudie, C. C. Steidel, and R. F. Trainor. Chemical abundance scaling relations for multiple elements in z 2–3 star-forming galaxies. *The Astrophysical Journal*, 925(2):116, jan 2022. doi: 10.3847/1538-4357/ac38a3. URL https://dx.doi.org/10.3847/1538-4357/ac38a3.

P. N. Tang, J. J. Eldridge, E. R. Stanway, and J. C. Bray. Dependence of gravitational wave transient rates on cosmic star formation and metallicity evolution history. *Monthly Notices of the Royal Astronomical Society*, 493(1):L6–L10, Mar. 2020. doi: 10.1093/mnrasl/slz183.

M. Tegmark, J. Silk, M. J. Rees, A. Blanchard, T. Abel, and F. Palla. How Small Were the First Cosmological Objects? *Astrophysical Journal*, 474:1, Jan. 1997. doi: 10.1086/303434.

I. Thies and P. Kroupa. A discontinuity in the low-mass initial mass function. *The Astrophysical Journal*, 671(1):767, dec 2007. doi: 10.1086/522512. URL https://dx.doi.org/10.1086/522512.

I. Thies and P. Kroupa. A discontinuity in the low-mass IMF - the case of high multiplicity. *Monthly Notices of the Royal Astronomical Society*, 390(3):1200–1206, Nov. 2008. doi: 10.1111/j.1365-2966.2008.13827.x.

R. Tibshirani. Regression shrinkage and selection via the lasso. *Journal of the Royal Statistical Society. Series B (Methodological)*, 58(1):267–288, 1996. ISSN 00359246. URL http://www.jstor.org/stable/2346178.

B. M. Tinsley. Stellar lifetimes and abundance ratios in chemical evolution. *Astrophysical Journal*, 229:1046–1056, May 1979. doi: 10.1086/157039.

A. R. Tomczak et al. Galaxy stellar mass function from zfourge/candels: An excess of low-mass galaxies since z=2 and the rapid buildup of quiescent galaxies. *The Astrophysical Journal*, 783(2):85, feb 2014. doi: 10.1088/0004-637x/783/2/85. URL https://doi.org/10.1088/0004-637x/783/2/85.

A. Torres-Forné, A. Marquina, J. A. Font, and J. M. Ibáñez. Denoising of gravitational wave signals via dictionary learning algorithms. , 94(12):124040, Dec. 2016. doi: 10.1103/PhysRevD.94.124040.

A. Torres-Forné, E. Cuoco, J. A. Font, and A. Marquina. Application of dictionary learning to denoise LIGO's blip noise transients. *Physical Review D*, 102(2):023011, July 2020. doi: 10.1103/PhysRevD.102.023011.

C. A. Tremonti, T. M. Heckman, G. Kauffmann, J. Brinchmann, S. Charlot, S. D. M. White, M. Seibert, E. W. Peng, D. J. Schlegel, A. Uomoto, M. Fukugita, and J. Brinkmann. The origin of the mass-metallicity relation: Insights from 53,000 star-forming galaxies in the sloan digital sky survey. *The Astrophysical Journal*, 613(2):898–913, oct 2004. doi: 10.1086/423264. URL https://doi.org/10.1086/423264.

S. A. Usman et al. The PyCBC search for gravitational waves from compact binary coalescence. *Classical and Quantum Gravity*, 33(21):215004, Nov. 2016. doi: 10.1088/0264-9381/33/21/215004.

L. A. C. van Son, S. E. de Mink, T. Callister, S. Justham, M. Renzo, T. Wagg, F. S. Broekgaarden, F. Kummer, R. Pakmor, and I. Mandel. The Redshift Evolution of the Binary Black Hole Merger Rate: A Weighty Matter. *Astrophysical Journal*, 931(1):17, May 2022. doi: 10.3847/1538-4357/ac64a3.

P. Veres, T. Dal Canton, E. Burns, A. Goldstein, T. B. Littenberg, N. Christensen, and R. D. Preece. Fermi-GBM Follow-up of LIGO-Virgo Binary Black Hole Mergers: Detection Prospects. *Astrophysical Journal*, 882(1):53, Sept. 2019. doi: 10.3847/1538-4357/ab31aa.

J. S. Vink and A. de Koter. On the metallicity dependence of Wolf-Rayet winds. *Astronomy and Astrophysics*, 442(2):587–596, Nov. 2005. doi: 10.1051/0004-6361:20052862.

J. S. Vink and A. A. C. Sander. Metallicity-dependent wind parameter predictions for OB stars. *Monthly Notices of the Royal Astronomical Society*, 504(2):2051–2061, June 2021. doi: 10.1093/mnras/stab902.

J. S. Vink, A. de Koter, and H. J. G. L. M. Lamers. Mass-loss predictions for O and B stars as a function of metallicity. *Astronomy and Astrophysics*, 369:574–588, Apr. 2001. doi: 10.1051/0004-6361:20010127.

S. Vitale, S. Biscoveanu, and C. Talbot. Spin it as you like: The (lack of a) measurement of the spin tilt distribution with LIGO-Virgo-KAGRA binary black holes. , 668:L2, Dec. 2022. doi: 10.1051/0004-6361/202245084.

R. F. Webbink. Double white dwarfs as progenitors of R Coronae Borealis stars and type I supernovae. , 277:355–360, Feb. 1984a. doi: 10.1086/161701.

R. F. Webbink. Double white dwarfs as progenitors of R Coronae Borealis stars and type I supernovae. *Astrophysical Journal*, 277:355–360, Feb. 1984b. doi: 10.1086/161701.

K. W. K. Wong, K. Breivik, K. Kremer, and T. Callister. Joint constraints on the field-cluster mixing fraction, common envelope efficiency, and globular cluster radii from a population of binary hole mergers via deep learning. *Physical Review D*, 103(8):083021, Apr. 2021. doi: 10.1103/PhysRevD.103.083021.

S. E. Woosley. The Evolution of Massive Helium Stars, Including Mass Loss. *Astrophysical Journal*, 878(1):49, June 2019. doi: 10.3847/1538-4357/ab1b41.

M. Zevin and S. S. Bavera. Suspicious Siblings: The Distribution of Mass and Spin across Component Black Holes in Isolated Binary Evolution. *Astrophysical Journal*, 933(1):86, July 2022. doi: 10.3847/1538-4357/ac6f5d.

M. Zevin, J. Samsing, C. Rodriguez, C.-J. Haster, and E. Ramirez-Ruiz. Eccentric Black Hole Mergers in Dense Star Clusters: The Role of Binary-Binary Encounters. *Astrophysical Journal*, 871(1):91, Jan. 2019. doi: 10.3847/1538-4357/aaf6ec.

M. Zevin, S. S. Bavera, C. P. L. Berry, V. Kalogera, T. Fragos, P. Marchant, C. L. Rodriguez, F. Antonini, D. E. Holz, and C. Pankow. One Channel to Rule Them All? Constraining the Origins of Binary Black Holes Using Multiple Formation Pathways. *Astrophysical Journal*, 910(2):152, Apr. 2021. doi: 10.3847/1538-4357/abe40e.

Appendix A

Binary population synthesis flags

BPS Flag	Description	Values
$Z_{\odot}$ (zsun)	Value of solar metallicity from Asplund et al. [2009].	**0.014**
β (beta)	Wind velocity factor β_w. -1: Belczynski et al. [2008]; positive value: supplied to Equation 12, Hurley et al. [2002] .	**-1**, 0.125, 7
$\dot{M}L_{\rm edd}$ (eddlimflag)	Wind mass loss dependence on metallicity near the Eddington limit. 0: No dependence; 1: Giacobbo et al. [2018].	**0**, 1
α (alpha)	CE efficiency parameter from Equation 71, Hurley et al. [2002].	0.2, 0.5, **1**, 5, 10
λ (lambdaf)	CE binding energy factor from Equation 69, Hurley et al. [2002]. 0: Claeys et al. [2014] prescription without extra ionization energy contribution; -1: λ chosen to satisfy $\alpha\lambda$ = 1; 1: Claeys et al. [2014] prescription with full contribution of extra ionization energy.	-1, **0**, 1
$CE_{\rm Merger}$ (ce_merge-flag)	Determining whether stars beginning CE while lacking core-envelope boundary automatically lead to a stellar merger [Belczynski et al., 2008]. 0: No stellar merger; 1: stellar merger.	0, **1**.
$E_{\rm orb,\,i}$ (ceflag)	CE initial orbital energy calculation. 0: Using core mass as in Equation 70, Hurley et al. [2002]; 1: Using total binary mass as in de Kool [1990].	0, **1**

$q_{\rm crit}$ (qcflag)	CE onset based on critical mass ratio models. 0: Section 2.6 of Hurley et al. [2002]; 1: Hjellming and Webbink [1987] for GB/AGB stars, otherwise same as 0; 2: Table 2 of Claeys et al. [2014], 3: Hjellming and Webbink [1987] for GB/AGB stars otherwise same as 2; 4: Section 5.1 of Belczynski et al. [2008].	0, 1, **2**, 3, 4
$v_{\rm Kick}$ (kickflag)	Natal kicks of Fe core-collapse supernova based on Maxwellian dispersion parameter σ (for $v_{\rm Kick}$ = 0, -1, -2). 0: Standard COSMIC prescription with additional options from $v_{\rm BH}$; -1: Kick based on Eq. (1) of Giacobbo and Mapelli [2020]; -2: kicks based on Eq. (2) of Giacobbo and Mapelli [2020]; -3: Kicks based on Eq. (1) of Bray and Eldridge [2016].	**0**, -1, -2, -3
σ (sigma)	Maxwellian dispersion parameter for SN kick (km/s).	90, **256**, 530
v_{BH} (bh-flag)	Scalling BH kicks. 1: fallback-modulated [Fryer et al., 2012]; 2: Linear momentum conservation which scales down kick by BH to neutron star mass; 3: Kicks not scaled.	**1**, 2, 3
$PISN$ (pisn)	Sets pair-instability supernova (PISN) and pulsational pair-instability supernova (PPISN) model. 0: No PISN or PPISN; -1: Spera and Mapelli [2017]; -2: Table 1 in Marchant et al. [2019]; -3: Table 5 in Woosley [2019].	-3,**-2**, -1, 0
$M_{\rm NS-BH}$ (remnant-flag)	Remnant mass prescription specifically for BHs. 0: Section 6 of Hurley et al. [2002]; 1: Belczynski et al. [2002]; 2: Belczynski et al. [2008]; 3: rapid prescritopn from Fryer et al. [2012]; 4: delayed prescription from Fryer et al. [2012].	0, 1, 2, **3**, 4
$Tide_{\rm ST}$ (ST_tide)	Tide prescription. 0: Hurley et al. [2002]; 1: Belczynski et al. [2008].	0, **1**

Table A.1: The description and values of the flags I explore with the COSMIC binary population synthesis (BPS) code. The three columns depict the symbol of the flag, its description, and the values I explore in my 40 simulations. Values in bold are the default values. For each BPS simulation, besides the default, I assign a given flag its value described in the table and set all other flags to their default (bold) value.